RICE UNIVERSITY

WW production cross section measurement and limits on anomalous trilinear gauge couplings at $\sqrt{s} = 1.96$ TeV

by

Michael P. Cooke

A Thesis Submitted
in Partial Fulfillment of the
Requirements for the Degree

Doctor of Philosophy

Approved, Thesis Committee:

Marjorie D. Corcoran, Chair
Professor of Physics and Astronomy

B. Paul Padley
Associate Professor of Physics and Astronomy

David W. Scott
Noah Harding Professor of Statistics

Houston, Texas

April, 2008

WW production cross section measurement and limits on anomalous trilinear gauge couplings at $\sqrt{s} = 1.96$ TeV

Michael P. Cooke

Abstract

The cross section for WW production is measured and limits on anomalous $WW\gamma$ and WWZ trilinear gauge couplings are set using $WW \to ee/e\mu/\mu\mu$ events collected by the Run II DØ detector at the Fermilab Tevatron Collider corresponding to 1 fb^{-1} of integrated luminosity at $\sqrt{s} = 1.96$ TeV. Across the three final states, 108 candidate events are observed with 40.8±3.8 total background expected, consistent with $\sigma(p\bar{p} \to WW) = 11.6 \pm 1.8$ (stat) ± 0.7 (syst) ± 0.7 (lumi) pb. Using a set of $SU(2)_L \otimes U(1)_Y$ conserving constraints, the one-dimensional 95% C.L. limits on trilinear gauge couplings are $-0.63 < \Delta\kappa_\gamma < 0.99$, $-0.15 < \lambda_\gamma < 0.19$, and $-0.14 < \Delta g_1^Z < 0.34$.

Acknowledgments

I would like to thank my family, who lovingly supported me throughout my career as a graduate student. I would also like to thank the many members of Diboson group at DØ who have influenced this analysis, especially Andrew, Jim, Tom, Rob, Chad, Yurii and Greg.

I'd like to give special thanks to my advisor, Marj Corcoran. Her excitement about the field of High Energy Physics helped encourage me to pursue it's study.

Finally, I'd like to thank my father, who always cultivated my curiosity and encouraged critical thinking. He opened my mind up to the world and helped provide this opportunity to explore the nature of the universe. He will be missed.

Contents

Illustrations

Tables

Chapter 1

Introduction

1.1 Standard Model

1.1.1 Quarks and Leptons

The vacuum is awash with particles, or particle and antiparticle pairs to be precise. Modern physical theory demands it and modern experiments support it. What was once thought to be cold and devoid of activity is now found to be bubbling with a life of it's own, just as atoms that were once thought indivisible are now known to be composed of more fundamental objects, quarks and leptons. The Standard Model of particle physics, a framework of quantized field theories, details the interactions between quarks and leptons through the force carriers, or gauge bosons.

Quarks and leptons are fermions, particles with intrinsic angular momentum equal to a half integral unit of $\hbar$. Bosons, on the other hand, are particles with integer multiples of $\hbar$ spin. In fact, all quarks possess spin equal to $\frac{1}{2}$, in units of $\hbar$, while all gauge bosons are spin 1. There are six known quarks and six known leptons, all grouped into three generations as shown by the columns in Table 1.1. Each generation of particles repeats the charge properties of the last, but with increasing mass. These particles, along with their antiparticle partners, compose all of the known material in

the universe.

Quarks:

Up (u) 1 MeV $< m_u <$ 5 MeV	Charm (c) 1.15 GeV $< m_c <$ 1.35 GeV	Top (t) $m_t = 174.3 \pm 5.1$ GeV
Down (d) 3 MeV $< m_d <$ 9 MeV	Strange (s) 75 MeV $< m_s <$ 170 MeV	Bottom (b) 4.0 GeV $< m_b <$ 4.4 GeV

Leptons:

Electron (e) $m_e = 0.51$ MeV	Muon (μ) $m_\mu = 106$ MeV	Tau (τ) $m_\tau = 1.77$ GeV
Electron type Neutrino (ν_e)	Muon type Neutrino (ν_μ)	Tau type Neutrino (ν_τ)

Table 1.1 : Quarks and Leptons are divided into three generations, here indicated by the three separate columns. Each quark in the top row has electrical charge equal to $\frac{2}{3}e$, where $-e$ is an electron charge, while each lower row quark's charge is $-\frac{1}{3}e$. Each upper row lepton shares the electron's charge while each type of neutrino is neutral. Note that ν_e, ν_μ and ν_τ are not mass eigenstates.

All quarks and leptons interact through the unified electroweak force, which describes the interactions of electrically charged particles and neutrinos through the exchange of photons and $W^{\pm}$ and Z^0 bosons. However, only quarks are subject to the strong force, in which particles with color charge interact with force carrying gluons, because only quarks (and the gluons they interact with) carry color. In this manner, quarks can combine into two different types of hadrons, or composite particles made of quarks, called baryons and mesons.

A baryon is composed of three quarks, qqq, or three antiquarks, $\overline{qqq}$, while a meson is a quark-antiquark pair, $q\overline{q}$. Baryons and mesons have integer electric charge, if any, but are overall color neutral. A particle can carry a color charge of Red (R), Green (G), or Blue (B) or an "anticolor" charge of Cyan ($\overline{R}$), Magenta ($\overline{G}$), or Yellow ($\overline{B}$).

Colorless states consist of either a color and it's anticolor, such as $R\overline{R}$, or a three color state of either RGB or $\overline{RGB}$. No particles have been detected that have an overall color state due to quark confinement, an effect brought about because gluons, also carriers of color charge, interact with themselves. The energy used in attempting to separate confined quarks instead creates new quark-antiquark pairs, so quarks are only found within, or are confined to, composite particles. This process leads to jets, or tightly packed sprays of mostly hadronic particles, a phenomena seen often in particle detectors at large particle accelerator facilities.

There are a total of twelve gauge bosons, as described in Table 1.2, ranging from the massless and neutral to the massive and charged. The photon (γ) mediates electromagnetic interactions and, due to it's lack of mass, gives the electromagnetic force an infinite range. The $W^{\pm}$ and Z bosons mediate the weak interaction, which is "weak" because of the large mass of the force carriers. A total of eight gluons are required as carriers of the strong force, due to the gauge symmetry group of the strong interaction, as discussed in Section 1.1.2. Gluons are never seen outside of the composite particles they help create.

Gauge Boson	**Charge**	**Mass**
γ (photon)	0	0
$W^{\pm}$ (weak bosons)	± 1	80.4 GeV
Z (weak boson)	0	91.2 GeV
g_i (gluon, $i = 1, ..., 8$)	0	0

Table 1.2 : Charge is given in units where an electron has charge -1. All gauge bosons have spin $\hbar$. Gluons also carry color charge and are self-interacting.

1.1.2 Quantum Field Theories

Some of the most powerful theories of modern physics stem from the idea that symmetry principles can be used to describe physical interactions. This is clearly evidenced in the Standard Model of particle physics, in which particle interactions are described by local gauge symmetries. When choosing a Lorentz scalar Lagrangian in quantum field theory, the overall phase of the wavefunction for a single particle may be arbitrarily defined without affecting any measurable quantities. This choice of a global gauge is simply a freedom of the system, related to the conservation of charge.[1] Just as Noether's theorem describes the relationship between translational invariance and conservation of momentum, the global phase invariance in quantum field theory is connected to charge conservation.

But a global gauge invariance is not the most general form available, instead a local gauge symmetry could be established in which the phase of a wavefunction could depend on space and time coordinates in a completely arbitrary way. However, the generic Lagrangian of a Lorentz scalar is not invariant under local gauge transformations. For a particle field, $\psi(x)$, a local gauge transformation takes the form of

$$\psi \rightarrow e^{i\alpha(x)}\psi, \tag{1.1}$$

where $\alpha(x)$ is an arbitrary function of space and time. A Lagrangian term involving a derivative of the form $\partial_\mu\psi$ will lead to an extra term in the Lagrangian involving

$\partial_\mu \alpha$, which breaks the invariance:

$$\partial_\mu \psi \rightarrow e^{i\alpha(x)} \partial_\mu \psi + i e^{i\alpha(x)} \psi \partial_\mu \alpha \tag{1.2}$$

By constructing a covariant derivative, D_μ, which transforms like a vector under the gauge transformation, the offending $\partial_\mu \alpha$ term can be removed. This can be accomplished through the definition

$$D_\mu \equiv \partial_\mu - ieA_\mu, \tag{1.3}$$

where the vector field A_μ transforms as

$$A_\mu \rightarrow A_\mu + \frac{1}{e} \partial_\mu \alpha. \tag{1.4}$$

In quantum electrodynamics (QED), the A_μ vector field, or the gauge field, represents the photon field that interacts with the charged particle fields. In order for the gauge invariance to hold, the photon must be massless. Thus, by applying the idea of local gauge invariance, the theory of electron-photon interactions, QED, is formed.

The family of phase transformations, $U(\alpha) = e^{i\alpha(x)}$, used to create the photon field forms the unitary Abelian group $U(1)$. The term Abelian simply denotes that multiplication within this group is commutative. Quantum chromodynamics (QCD) is an extension of QED in that it is formed by forcing local gauge invariance of a group of phase transformations upon a Lagrangian. This time, the $SU(3)$ group, which has eight generators, is used to describe the transformations of the quark color fields. Eight gauge fields must be introduced in order to allow the phase of the three

color fields to vary arbitrarily and produce complete invariance under local phase transformations, with each gauge field representing a type of gluon. Once again, the force carrying particles must be massless in order for the invariance to hold. In addition, achieving complete invariance introduces self-interacting gluon terms into the Lagrangian, due to the non-Abelian nature of the $SU(3)$ group.

Whereas QCD is a natural evolution of the gauge invariant quantum field theory, the weak interactions must account for the behavior seen in nature, namely that the weak coupling inherently violates parity conservation and that the weak gauge bosons are massive. The helicity of a particle is the projection of its spin onto its momentum vector. When a particle's spin aligns with it's momentum it is considered "right-handed," while antialignment is called "left-handed." In nature, only left-handed neutrinos, ν_L, and right-handed antineutrinos, $\overline{\nu}_R$, are involved in weak interactions. Individually, both parity (P) invariance and charge conjugation (C) invariance are violated by this preference of nature, though when both transformations (CP) are applied the system is invariant.

In order to accommodate for empirical left-handedness of the weak force, a special symmetry group is constructed of gauge fields that only couple to left-handed particles (or right-handed antiparticles), $SU(2)_L$. This "weak isospin" triplet of currents cannot completely describe the weak force as observed, since neutral current weak interactions are observed to include a right-handed component for particles other than neutrinos. This requires the introduction of a current that contains a right-

handed component but is unchanged under $SU(2)_L$ transformations. The "weak hypercharge" current, based on the electromagnetic current of QED, is selected, where the hypercharge, Y, of a particle is related to its charge, Q, and weak isospin, T_3, by $Q = T_3 + Y/2$. The hypercharge operator generates a symmetry group $U(1)_Y$, expanding the electroweak symmetry group to $SU(2)_L \otimes U(1)_Y$. The photon and the Z boson are described by a mixture of the neutral weak isospin current and the weak hypercharge current:

$$A_\mu = B_\mu \cos\theta_W + W^3_\mu \sin\theta_W \tag{1.5}$$

$$Z_\mu = -B_\mu \sin\theta_W + W^3_\mu \cos\theta_W \tag{1.6}$$

where A_μ is the photon field, Z_μ is the Z boson field, B_μ is the weak hypercharge field, W^3_μ is the neutral weak isospin field, and θ_W is the weak mixing angle. While an $SU(2)_L \otimes U(1)_Y$ symmetry has the mathematical capability to produce the complete set of weak and electromagnetic currents, the weak bosons still lack mass within this theoretical framework (see Table 1.2).

The Higgs mechanism is used to add masses to the weak bosons. A set of four real scalar fields are added to the electroweak Lagrangian. In order to keep the Lagrangian gauge invariant, these scalar fields must belong to $SU(2)_L \otimes U(1)_Y$ multiplets. In the Weinberg-Salam model, the four scalar fields are arranged into an isospin doublet with weak hypercharge $Y = 1$. The potential energy of the scalar fields is arranged to contain equivalent minima for an entire circle of points, creating a potential energy curve that looks much like a "Mexican hat." When a single point along this circle

is chosen in order to set the system's parameters, the continuous symmetry of the system is broken. The extra degrees of freedom introduced into the system can be reparameterized into terms that act like a mass in the Lagrangian. When chosen properly, the scalar fields introduced into the weak force can allow for the massless photon and massive weak bosons. While the Higgs mechanism produces the proper mass terms, particle masses arise from Yukawa couplings to the Higgs field, which are arbitrary, so the Higgs mechanism does not actually predict particle masses.

An after effect of the Higgs mechanism is that an excitation of the Higgs scalar field, the Higgs boson, is also predicted. The Higgs boson would couple to particles in direct proportion to their mass and would produce higher order corrections to the cross sections of certain processes. So far, no search for the Higgs boson has confirmed its existence, though its discovery is eagerly anticipated.

While the weak interactions link quark and lepton pairs within each generation, $e \leftrightarrow \nu_e$, $\mu \leftrightarrow \nu_\mu$, $u \leftrightarrow d$ and so on, quark states are also mixed via decays such as $K^+ \rightarrow \mu^+\nu_\mu$, implying that somehow $u \leftrightarrow s$ interactions are possible. This introduces the Cabibbo angle, θ_C, used to rotate the quark doublets from the mass eigenstates (d, s) to the the weak eigenstates (d', s') that weak gauge bosons interact with: [2]

$$\begin{pmatrix} d' \\ s' \end{pmatrix} = \begin{pmatrix} \cos\theta_C & \sin\theta_C \\ -\sin\theta_C & \cos\theta_C \end{pmatrix} \begin{pmatrix} d \\ s \end{pmatrix} \tag{1.7}$$

After the c quark was discovered, Kobayashi and Maskawa generalized Cabibbo's idea, creating a parametrization for the u, d, s, and c quarks [3]. They further proposed that it could be extended to a 3×3 matrix, now known as the "CKM matrix,"

to represent mixing between three generations of quarks, in which case the parameterization includes three angles and a complex phase. This complex phase allows CP-violating transitions because under a CP transformation, CKM matrix elements become their complex conjugates. A certain amount of CP violation is believed to be necessary in nature in order to explain the matter-antimatter asymmetry in the universe today.[4] While certain weak decays in the K and B meson sectors show small amounts of CP violation, the observed CP violations are not large enough to account for the matter-antimatter asymmetry.

1.2 Experimental High Energy Physics

The frontier of physical research tests the precision and accuracy of our current theoretical predictions while searching for signs of physics beyond the Standard Model. Experiments are designed to test detailed predictions for their accuracy, search for the predicted particles and effects of new theoretical models, and explore the energy frontier for signs of new physics.

QED is a precisely tested model of electron-photon interactions. The anomalous magnetic moment of the electron has been carefully predicted to ten significant figures and experimentally measured to as many with a mere 1.7σ difference between them [5, 6]. This is a phenomenally accurate precision measurement, considering that it is akin to measuring the distance from the tip of the Empire State Building to the top of the U.S. Capitol's dome ($\sim$ 370 km) to within the width of a human hair ($\sim$ 25 μm),

then realizing your prediction was less than two hair widths off!

While recently it seems that theory has driven the advancements in the field of High Energy Physics, predicting the existence of the massive $W^{\pm}$ and Z bosons and the t quark, the future of the field now relies on experiment. At facilities like Fermi National Accelerator Laboratory, experiments are performed with general purpose detectors that can simultaneously collect data useful for performing precision measurements, such as the measurement of an interaction's cross section or branching ratio, while also performing searches for new particles, such as the Higgs boson. New theories can also be tested or constrained, since some models would effect interaction cross sections or predict specific mass ranges for particles like the Higgs.

Already, many signs point to physics beyond the Standard Model and inherent problems in Quantum Field Theory, including recent developments in the field of Cosmology. The Standard Model lacks a mechanism to add masses to particles without the Higgs boson, which has yet to be discovered. Cosmological evidence points to dark matter and dark energy as being the predominant components of the universe, yet there is no evidence of what dark matter or dark energy could actually be, and neither seem to behave like quarks or leptons! Many competing models of physics beyond the Standard Model exist, including supersymmetry, technicolor, and string theory. Experiment once again drives High Energy Physics and the efforts at experiments like CDF and DØ at Fermilab, and later ATLAS and CMS at the Large Hadron Collider in Europe, will reveal the fundamental nature of our universe.

1.2.1 WW Production

The detailed study of WW production provides an opportunity to test the Standard Model at a fundamental level, by probing the triple gauge-boson coupling vertices, $WW\gamma$ and WWZ. In addition, a greater understanding of this process is desired because WW production is a major background to the search for a Higgs boson and certain theoretical new phenomena.

The principle of gauge-invariance is the foundation of the Standard Model. In the electroweak sector of the Standard Model, interactions are described by a non-Abelian gauge-group structure, which leads to very specific couplings between the electroweak gauge-bosons. Accurate measurements of the gauge-boson couplings provide for a fundamental test of the Standard Model.

The triple gauge-boson couplings (TGCs) occur in the Standard Model, at the three gauge-boson vertices $WW\gamma$ and WWZ. Both of these TGCs appear in the leading order Feynman diagrams for WW production, as shown in Figure 1.1. Each individual diagram contributes a divergent term to the WW production cross section, but destructive interference between the diagrams yields a finite cross section prediction, which leads to a strong dependence of the cross section on the specific values of the TGCs. In the most general Lorentz-invariant form, the effective Lagrangian that describes the TGCs has fourteen independent complex coupling parameters, seven

for each vertex [7]:

$$\begin{aligned}\mathcal{L}_{WWV}/g_{WWV} = {} & ig_1^V(W^\dagger_{\mu\nu}W^\mu V^\nu - W^\dagger_\mu V_\nu W^{\mu\nu}) + i\kappa_V W^\dagger_\mu W_\nu V^{\mu\nu} \\ & + \frac{i\lambda_V}{M_W^2}W^\dagger_{\lambda\mu}W^\mu{}_\nu V^{\nu\lambda} - g_4^V W^\dagger_\mu W_\nu(\partial^\mu V^\nu + \partial^\nu V^\mu) \\ & + g_5^V\epsilon^{\mu\nu\rho\sigma}(W^\dagger_\mu(\partial_\rho W_\nu) - (\partial_\rho W^\dagger_\mu)W_\nu)V_\sigma \\ & + \frac{1}{2}i\tilde{\kappa}_V\epsilon^{\mu\nu\rho\sigma}W^\dagger_\mu W_\nu V_{\rho\sigma} + \frac{i\tilde{\lambda}_V}{2M_W^2}\epsilon^{\nu\lambda\rho\sigma}W^\dagger_{\lambda\mu}W^\mu{}_\nu V_{\rho\sigma}\end{aligned} \tag{1.8}$$

where $V = \gamma$ or Z, W^μ is the W^- field, $W_{\mu\nu} = \partial_\mu W_\nu - \partial_\nu W_\mu$, $V_{\mu\nu} = \partial_\mu V_\nu - \partial_\nu V_\mu$, and the overall couplings are $g_{WW\gamma} = -e$ and $g_{WWZ} = -e\cot\theta_W$. In the Standard Model, $g_1^V = \kappa_V = 1$, and all other couplings are zero.

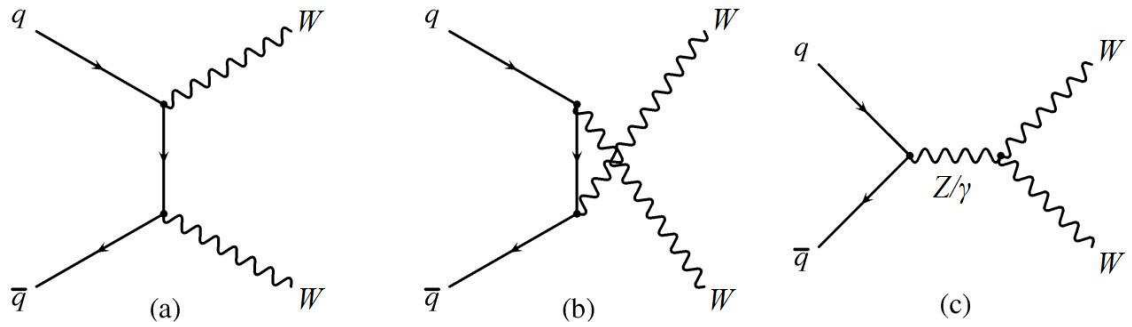

Figure 1.1 : Leading order Feynman diagrams for WW production.

All of the TGC parameters have fixed values in the Standard Model, and any deviation from the Standard Model values will lead to a change in the behavior of $q\bar{q} \to Z/\gamma^* \to W^+W^-$ production. In particular, anomalous values of the κ_V terms will cause the WW production cross section to rise proportionally to the center of mass energy at the parton level, $\sqrt{\hat{s}}$, while anomalous λ_V and g_1^V terms will grow as $\hat{s}$ [8]. If introduced alone, a constant finite anomalous value of a coupling will lead

to an unphysically large cross section, violating unitarity. Anomalous couplings are bounded by a unitarity limit because they can only contribute to WW production through the annihilation Feynman diagram in Figure 1.1(c), which can only contribute to the $J = 1$ partial wave expansion amplitude. Unitarity requires that any partial wave amplitude is bounded by a constant, therefore an anomalous coupling must be introduced as a form factor such that the coupling vanishes as the interaction energy increases [9]. The form factor used for a coupling A_0 is:

$$A(\hat{s}) = \frac{A_0}{(1 + \hat{s}/\Lambda^2)^2} \tag{1.9}$$

where the form factor scale, Λ, is a regularization scale related to, though not necessarily identical to, the energy scale at which new physics becomes important in the electroweak sector. The unitarity limits imposed upon a given coupling get tighter as Λ increases, which imposes a constraint upon the maximum value of Λ that is sensible to use, dependent on the sensitivity of the experimental measurement. Apart from this constraint, the most sensible value of Λ to use is that set by the energy scale of the experiment, which is ~ 2 TeV in the case of the Fermilab Tevatron Collider.

The specific values of the TGCs affect the kinematics of WW events. Figure 1.2 shows the area normalized expected distribution of $\sqrt{\hat{s}}$ for the Standard Model and an anomalous coupling scenario. The scenarios plotted in Figure 1.2 are generated by a leading order Monte Carlo by Hagiwara, Woodside and Zeppenfeld, which is capable of generating WW events with arbitrary TGC values [7]. Most important to this analysis is that when anomalous couplings are introduced, the distribution of

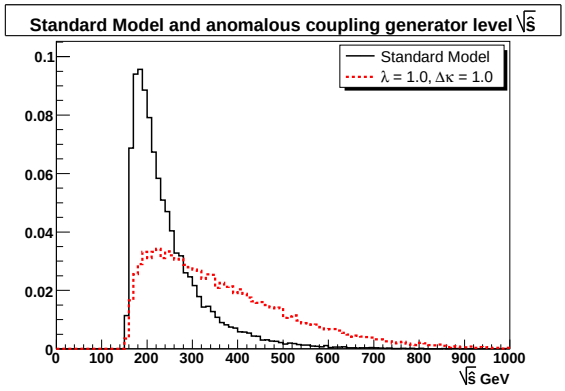

Figure 1.2 : Area normalized generator level MC [7] distribution of $\sqrt{\hat{s}}$ for the Standard Model (solid line) vs. an anomalous coupling scenario with $\lambda = 1.0$, $\Delta\kappa = 1.0$, and $\Lambda = 2$ TeV (dashed line).

the lepton transverse momentum, $p_T = \sqrt{p_x^2 + p_y^2}$ where z is the beam axis, has a much larger tail out to higher values than the expected Standard Model distribution. Comparing the leading and trailing lepton p_T distributions between various anomalous coupling models allows for enhanced discrimination beyond simply comparing against the expected number of events for each model. Various area normalized kinematic distribution differences are shown in Figure 1.3. Note that all kinematic differences in Figure 1.3 are determined by subtracting the low p_T lepton from the high p_T lepton.

The fourteen complex terms of the Lagrangian in Equation 1.8 are too numerous to be studied effectively, and are typically reduced based on maintaining consistency with current experimental observations. Specifically, CP violation is usually neglected when studying triple gauge-boson interactions, electromagnetic gauge invariance is expected to be preserved, and the $SU(2)_L \otimes U(1)_Y$ symmetry of electroweak interactions is expected to be preserved. Enforcing C and P conservation in the Lagrangian

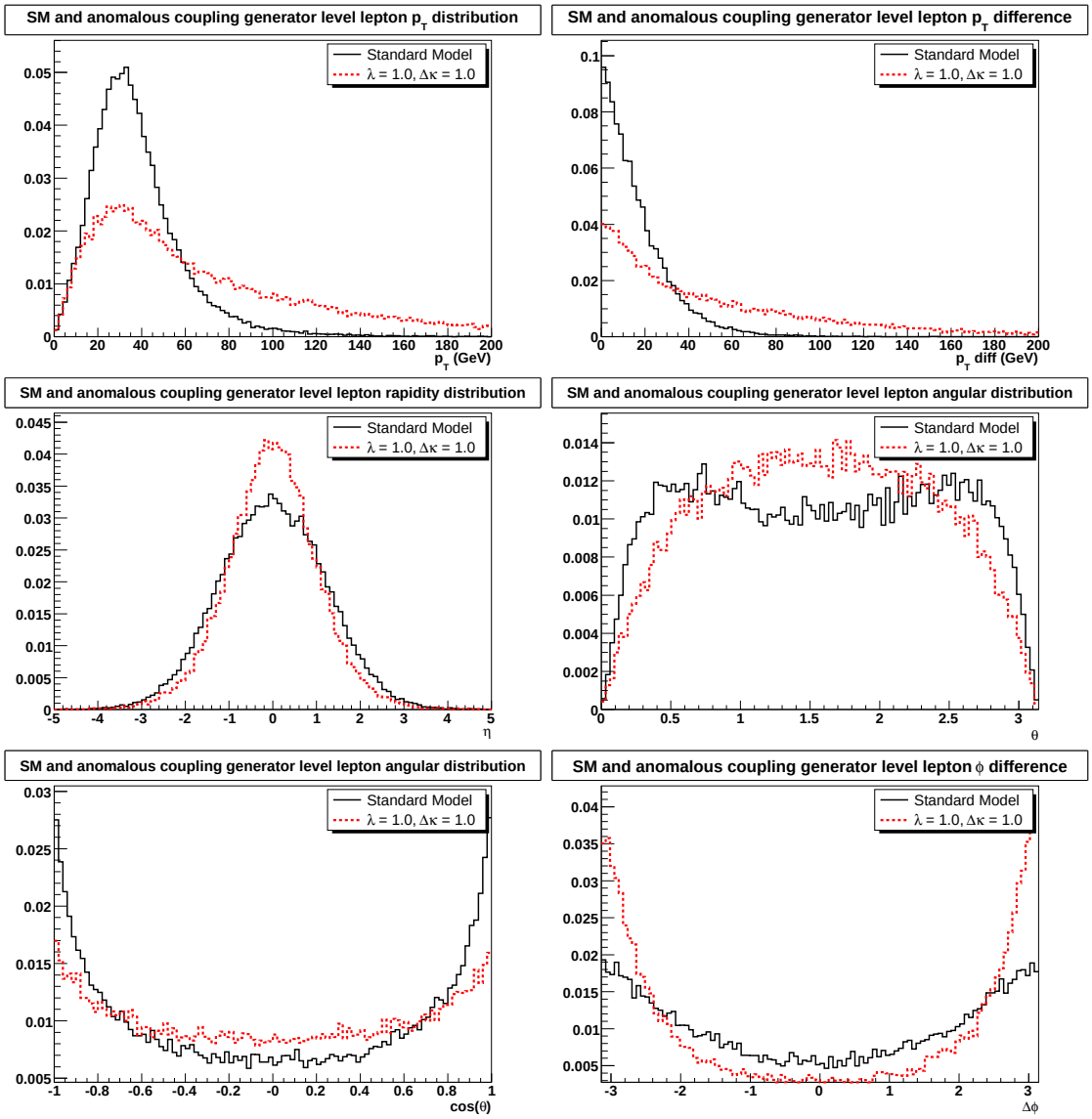

Figure 1.3 : Area normalized generator level MC [7] distributions for the Standard Model (solid) vs. an anomalous coupling scenario with $\lambda = 1.0$, $\Delta\kappa = 1.0$, and $\Lambda = 2$ TeV (dashed). All kinematic distribution differences are the result of subtracting the low p_T lepton from the high p_T lepton. The lepton production angle as measured from the beam axis is θ, $\eta = -\ln\tan(\theta/2)$, and ϕ is the azimuthal angle.

removes eight of the fourteen terms, because g_4^V violates CP and C, g_5^V violates C and P but is CP even, and $\tilde{\kappa}_V$ and $\tilde{\lambda}_V$ violate P and CP. Electromagnetic gauge invariance fixes $g_1^\gamma = 1$ (and $g_4^\gamma = g_5^\gamma = 0$). Requiring the Lagrangian to be $SU(2)_L \otimes U(1)_Y$ symmetric imposes the pair of constraints [10]:

$$\kappa_Z = g_1^Z - (\kappa_\gamma - 1)\tan^2\theta_W \tag{1.10}$$

$$\lambda_Z = \lambda_\gamma \tag{1.11}$$

Imposing all of these constraints reduces the number of free parameters in the TGC Lagrangian from 14 to three: κ_γ, λ_γ and g_1^Z.

This analysis seeks to measure the $p\bar{p} \to W^+W^-$ cross section and set limits on the trilinear gauge-boson couplings associated with $WW\gamma$ and WWZ vertices.

Chapter 2

The Tevatron and the DØ Collider Detector

2.1 The Tevatron

Fermilab National Accelerator Laboratory is currently host to the highest energy accelerator in the world. The Tevatron accelerates protons and antiprotons to 0.98 TeV, producing 1.96 TeV center of mass collisions inside of two collider detectors. While the Tevatron performs the final acceleration and directs the particles around the ring, an intricate network of accelerators are required to feed particles into the Tevatron. [11]

Fermilab's complex set of accelerators starts with a Cockroft-Walton device, where hydrogen gas from a bottle is negatively ionized. A positive voltage is applied and the ionic hydrogen is accelerated across a voltage gap to an energy of 750 keV. From here, the ions enter the Linear Accelerator, see Figure 2.1, where they are boosted to an energy of 400 MeV. Next, the hydrogen ions make their way to the Booster. As they enter the Booster, the ions hit a sheet of foil which strips their electrons and the remaining protons are accelerated to an energy of 8 GeV. From here, bunches of protons make their way to the Main Injector, where they are accelerated further and may be used to make antiprotons or injected directly into the Tevatron.

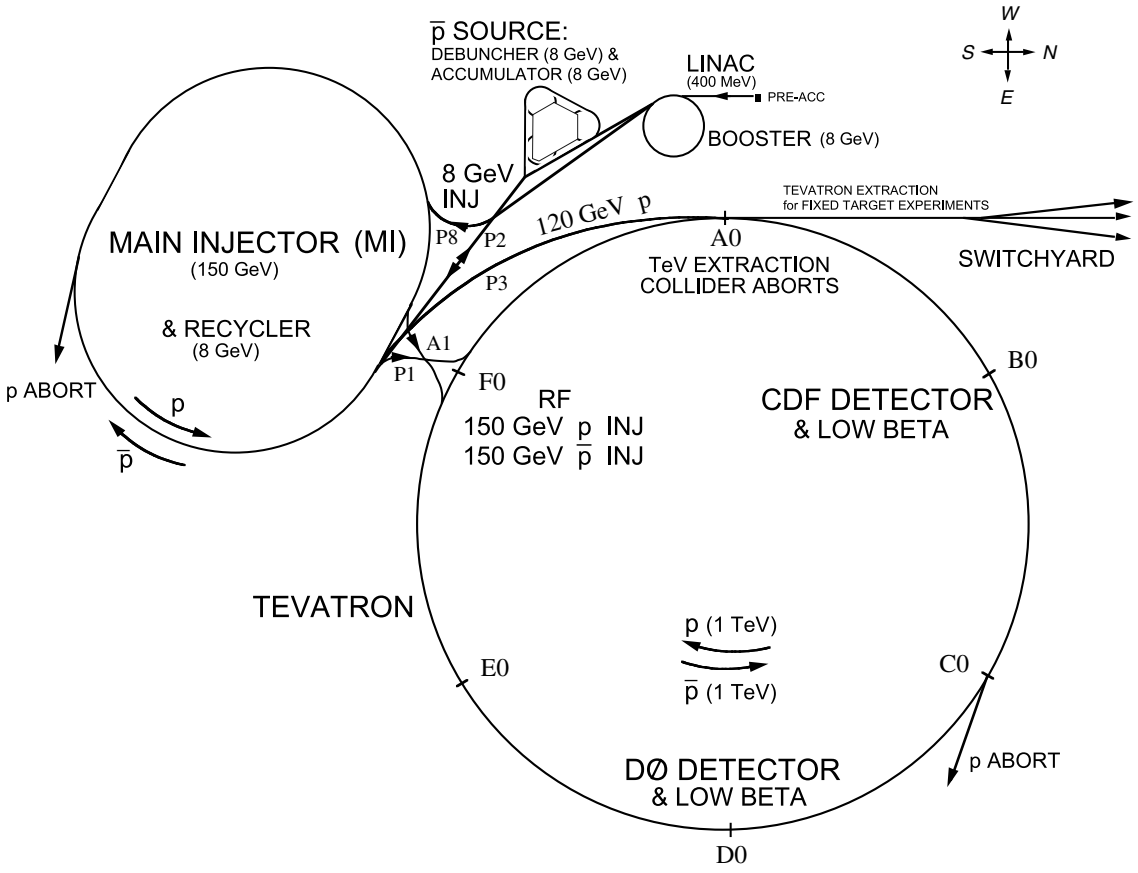

Figure 2.1 : Overview of the Tevatron and it's supporting accelerators. The Tevatron ring has a radius of 1 km, while the rest of the accelerators are drawn to the same scale.

To make antiprotons, the protons in the Main Injector are accelerated to an energy of 120 GeV and sent to the Antiproton Source. At the Antiproton Source, the incoming beam of protons hits a nickel target, causing a spray of secondary particles. The cone of secondary particles is rendered parallel by a lithium collection lens, a cylindrical lithium conductor that creates a solenoidal magnetic field which focuses negative particles. Next, the focused secondary particles reach a pulsed magnet where the applied magnetic field selects negative particles with about 8 GeV of energy. These selected particles continue into the Debuncher while the rest of the particles are absorbed in a beam dump. The Debuncher, one of two triangular rings at the Antiproton Source in Figure 2.1, is used to lower the momentum spread of the surviving antiprotons. Just before the next beam pulse from the nickel target is sent into the Debuncher, the antiprotons in the Debuncher are sent to the inner triangular ring, the Accumulator. The Accumulator stores many batches of antiprotons, continually cooling them to create dense regions of antiprotons. When enough antiprotons have been gathered, the densest regions of beam in the Accumulator can be extracted out to the Main Injector, where they may be accelerated for injection into the Tevatron.

While preparing the Main Injector to insert particles into the Tevatron for colliding beam physics, separate bunches of protons are coalesced into larger, denser superbunches of particles as they are inserted into the Main Injector. (The antiprotons do not need to undergo such a process, since they are taken from the densest

regions of the Accumulator's beam.) Then the protons and antiprotons are accelerated to an energy of 150 GeV. A total of 36 coalesced bunches each of protons and antiprotons are injected into the Tevatron. Three trains of 12 bunches each, with a spacing of 396 ns between bunches, are inserted. There is a 2.617 μs abort gap between each of the trains. Once inside the Tevatron, the particles are accelerated further to a peak energy of 0.98 TeV. The center of mass energy of proton-antiproton collisions at a collider detector, such as DØ or CDF, is 1.96 TeV.

2.2 Overview of the DØ Collider Detector

DØ is a general purpose collider detector that is designed to study a wide range of physics. It is as hermetic as possible in order to detect and measure as many of the final state particles as possible. Tracking subdetectors provide a measure of the momentum of charged particles near the center of the detector while large calorimeters force particles to shower and measure their energy. Outer layers flag and locally measure muon candidates that escape the rest of the detector.

The DØ collider detector is composed of four major layers, each visible in Figure 2.2. The innermost two tracking layers lie within a superconducting solenoidal magnet capable of producing a 2 Tesla magnetic field. The third layer, the calorimeter, measures the energy of most types of particles by bringing them to a stop. The final layer is designed to identify and further measure muons, the only charged particle that will escape the calorimeter. The only particles that cannot be directly measured

at DØ are neutrinos, though measurements of "missing transverse energy," or $\not\!\!E_T$, from the calorimeter may indicate the presence of neutrinos in interactions.

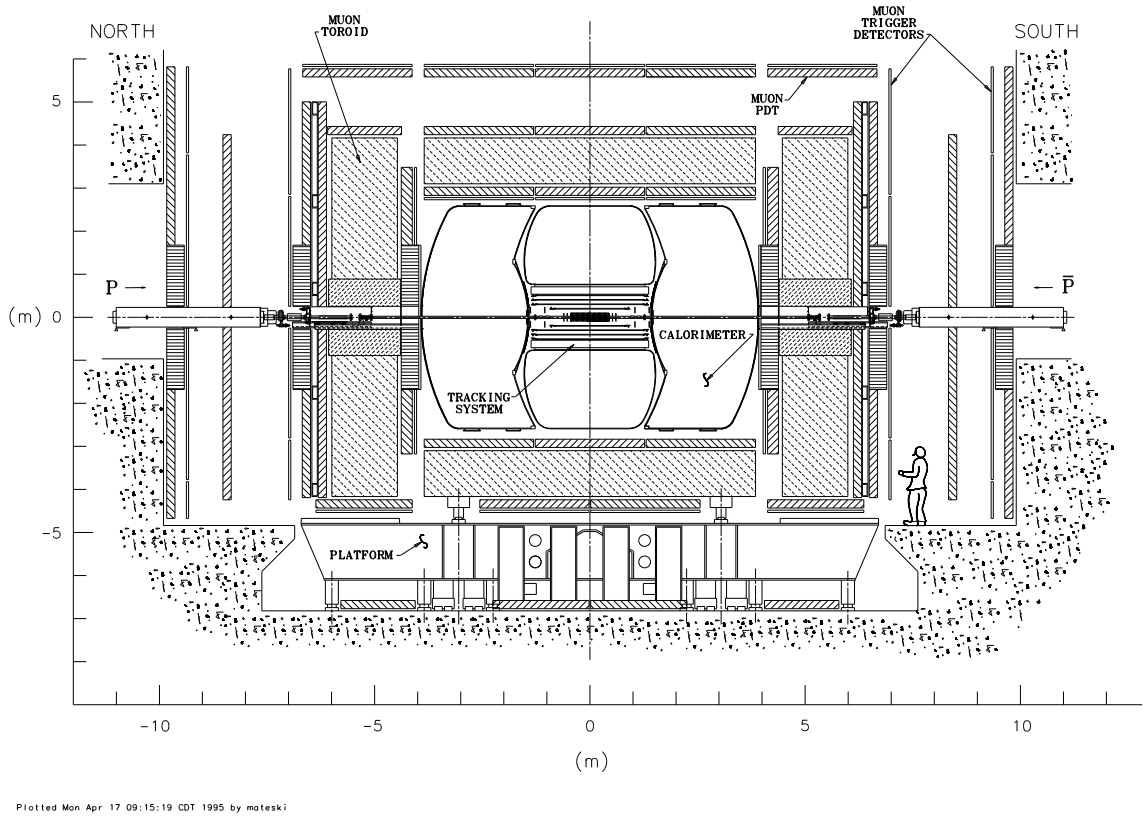

Figure 2.2 : Side view of the DØ collider detector. The four major subsystems of the detector, from innermost to outermost, are the Silicon Microstrip Tracker (SMT), the Central Fiber Tracker (CFT), the Calorimeter, and the Muon system. The two inner tracking layers lie within a 2 T solenoid.

The DØ detector is designed to operate with delivered instantaneous luminosities of 2×10^{32} cm^{-2}s^{-1}. The Tevatron timing structure produces a 1.7 MHz rate of bunch crossings within the detector, with the detector capturing data during each bunch crossing window. At typical DØ luminosities, about 10^{32} cm^{-2}s^{-1} where the total proton-antiproton interaction cross section is about 70 mb [12], about two proton-

antiproton interactions are expected during each beam crossing. The DØ detector is capable of writing full event data out to tape at a peak rate of about 50 Hz. The process of determining which events to write to tape is called "triggering," and this system is vital to the success of the DØ collaboration.

2.2.1 Units, Coordinate Systems and Special Variables at DØ

In the field of high energy physics a set of "natural units" is often used, based on the two fundamental constants in relativistic quantum mechanics, Plank's constant, $h = 2\pi\hbar$, and the velocity of light, c. Since $\hbar$ is a measure of action (ML^2/T) and c is a measure of velocity (L/T), the unit system can be completely defined through the choice of GeV as the definition of energy ($ML2/T^2$). By choosing the units such that $\hbar = c = 1$, it becomes unnecessary to explicitly write factors of $\hbar$ and c into formula, as such factors can always be determined unambiguously through dimensional analysis. In this unit system, energy, momentum and mass all share the same units, GeV, and factors of c are omitted when quoting their units. Such measurements can be easily converted back to standard units by inserting powers of c such that momentum has units of GeV/c and mass has units of GeV/c^2. In this thesis, energy, momentum and mass will all share the units of GeV, using the described standard. However, the second and the meter will be the basis of measuring time and length, even though they translate into units of GeV^{-1} in this scheme.

The DØ collider detector is cylindrically symmetric. The coordinates z, r, and ϕ,

are commonly used, as per the usual cylindrical coordinate system, though another quantity, psuedorapidity, η, is also often used to discuss the trajectory of particles within the detector. The z coordinate is measured as a distance along the axis of the beampipe, and r as a perpendicular distance away from the center of the beampipe. The angle ϕ, ranging between 0 and 2π, is measured counterclockwise from a horizontal plane bisecting the detector. Defining the antiproton bunch velocity within the DØ detector to be "north," zero, in ϕ, points west.

Rapidity, y, is defined by

$$y = \frac{1}{2} \ln \frac{E + p_{\|}}{E - p_{\|}} = \tanh^{-1} \beta_{\|} \tag{2.1}$$

where $p_{\|}$ is the component of the momentum parallel to the chosen axis, $\beta_{\|}$ is a similar component of the particle's velocity, and $\beta = v/c$, as normally defined in special relativity. Rapidity is a dimensionless quantity defined with respect to an axis (usually the beam axis for a particle physics experiment) and rapidity differences are invariant under Lorentz boosts along that axis. Also, in some processes, final state particles are produced uniformly in rapidity.

In the relativistic limit, or when the mass of the particle is ignored, rapidity becomes dependent only upon the production angle of a particle with respect to the beam axis. This approximation is called psuedorapidity, η, and is defined by

$$\eta = -\ln \tan \frac{\theta}{2} \tag{2.2}$$

where θ is the production angle. A value of $\theta = 90^{\circ}$ would be perpendicular to the beam axis and correlates to $\eta = 0$.

Since both ϕ and η differences between particles are Lorentz invariant, a useful Lorentz invariant separation, ΔR, can be defined be defined between two particles such that

$$\Delta R = \sqrt{(\Delta\phi)^2 + (\Delta\eta)^2} \tag{2.3}$$

where $\Delta\phi$ and $\Delta\eta$ are the ϕ and η differences between the two particles, respectively. Often, ΔR is used to define a Lorentz invariant cone around a single particle or detector position, in order to study nearby detector activity.

Certain other quantities are useful to define for studying $p\bar{p}$ interactions. The transverse momentum, p_T, of a particle is defined as the component of the momentum vector that is perpendicular to the beam axis. The transverse energy, E_T, of a particle is defined as

$$E_T = E \sin\theta \tag{2.4}$$

where θ represents the angle between the beam axis and the particle's energy deposit in the calorimeter. If the particle has a track associated with it, θ can be measured using the track. Otherwise, the primary vertex position is used to determine θ, where the primary vertex is the place where the largest number of high p_T tracks in an event originate. Since it is possible for more than one $p\bar{p}$ interaction to occur during a bunch crossing, multiple vertices can occur in the same event. This definition of the primary vertex attempts to choose the $p\bar{p}$ interaction involving the highest energy parton collision.

The transverse mass, m_T of a particle is defined as

$$m_T^2 = m^2 + p_T^2 \tag{2.5}$$

where m is the particle's rest mass. This quantity is useful to consider when studying W bosons in a leptonic decay channel because p_z of the neutrino produced by the W decay cannot be determined at DØ.

2.3 Silicon Microstrip Tracker

The Silicon Microstrip Tracker (SMT) is the first layer of the detector that a particle will reach after an interaction in the beampipe, spanning the radii 2.7 cm $< r <$ 10.5 cm from the center of the beampipe. It is constructed of many silicon wafers, both rectangular and wedge shaped, formed into cylinders ("barrels") and circular disks, respectively. The cylinders are layered concentrically around the beam pipe and provide both an azimuthal angle (ϕ) and a position along the beam pipe (z).

Strips approximately 10 μm wide are etched onto one or both sides of the SMT's silicon wafers, and each strip is individually resolved. In the cylindrical layers, position along the z-axis is determined by comparing hits on either side of the dual layered barrel wafers, or "ladders," of which there are two varieties. Both of these varieties have a set of strips aligned parallel with the beam pipe, but the strips on the other side are offset by either 2° or 90° from the first side of the wafer, allowing for approximate z-axis resolutions of 450 μm or 35 μm within the wafer, respectively. Six four-layer barrels, each 12 cm long, account for about half the readout channels of the SMT.

The rest of the approximately 793,000 channels of readout are from silicon wedges formed into disks.[13]

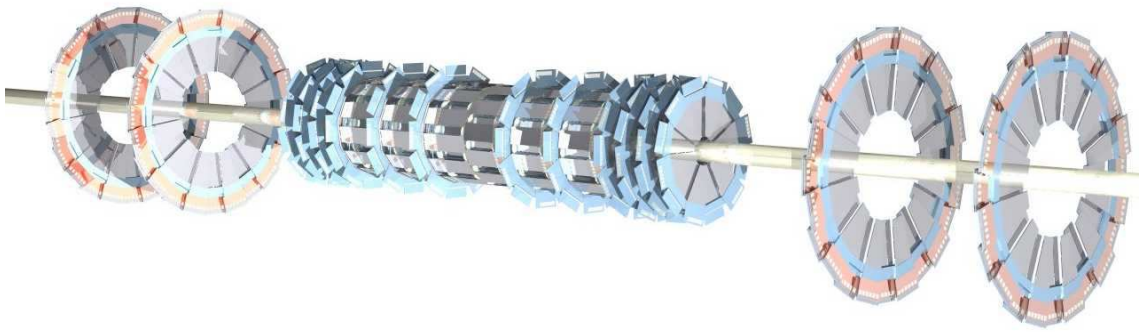

Figure 2.3 : The Silicon Microstrip Tracker (SMT) is at the heart of the DØ detector, lying just outside the beampipe. It is the first detection equipment a particle will reach after an interaction. The inner barrels and disks lie between 2.7 cm and 10.5 cm from the center of the beampipe, while the outermost four disks lie between 9.5 cm and 26 cm.

Smaller circular disks, "F-disks," are made from two-sided wedges and are interspersed between the six barrel sections. The strips on the two sides of these disks are 30° offset from one another, each side offset from a radial line by 15°, providing a measurement of both r and ϕ at a given z. Together the twelve F-disks provide forward tracking in the inner regions of the SMT. Four "H-disks" are made from single-sided wedges glued back-to back, producing an effective 15° offset from each other, or 7.5° each way from a radial line. These disks lie much further out along the beampipe from the bulk of the SMT and provide coverage in the high psuedorapidity region, $2 < |\eta| < 3$, lying between 9.5 cm and 26 cm from the center of the beampipe.

2.4 Central Fiber Tracker

The Central Fiber Tracker (CFT) is made of eight cylindrical superlayers of scintillating fibers and extends from 20.0 cm to about 51.6 cm from the center of the beampipe. These fibers scintillate in the yellow-green part of the visible spectrum, with a peak emission wavelength of 530 nm. Each superlayer consists of an axial layer of fibers and a stereo layer of fibers about 2° off-axis. Superlayers alternate between "U" and "V" stereo layers, each wrapping an opposite direction around the cylinder. Each fiber is 835 μm in diameter and all fiber layers, axial and stereo, are arranged in "doublet layers" such that a second set of scintillating fibers lie in the gaps between the first set. One end of the scintillating fibers are reflectively coated, forcing most of the produced light to escape into the waveguide optically connected to the other end.[14]

Clear fiber waveguides relay the light to the photodetectors underneath the calorimeter. The photodetectors used to read the light pulses are Visible Light Photon Counters (VLPCs), a variant of the solid state photomultiplier. These chips, when operating at their optimal temperature of 9 K, have approximately 70% quantum efficiency in the wavelength range of the scintillating fibers ($\sim$530 nm), gain of about 20,000, and can operate at 10 MHz or better.

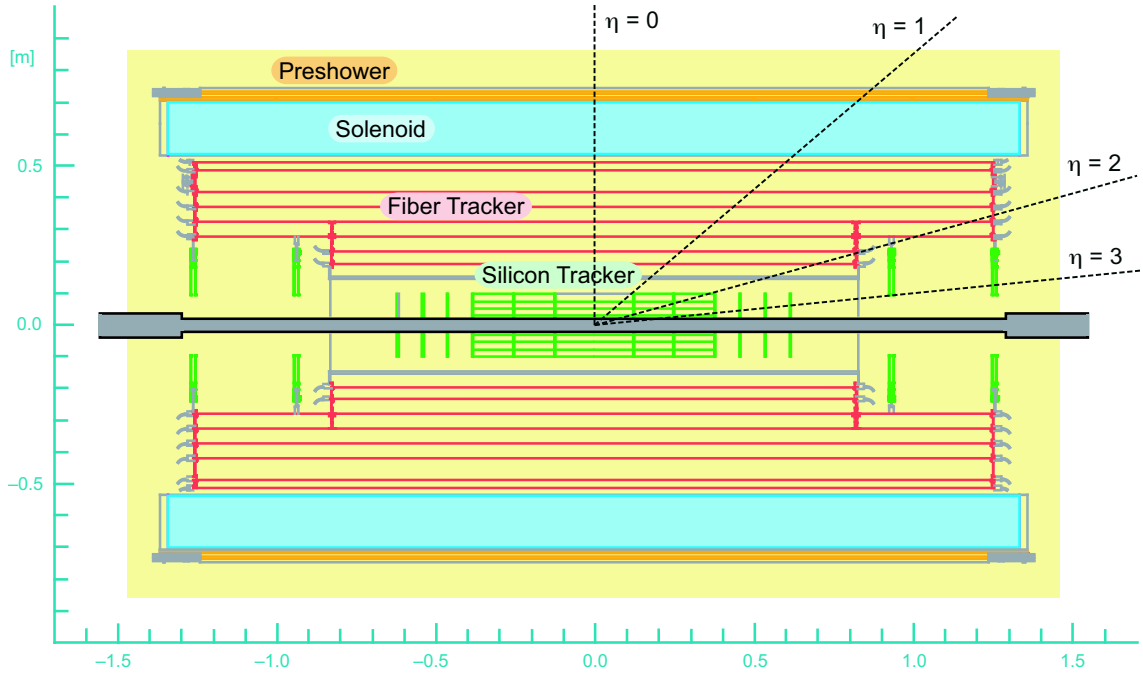

Figure 2.4 : The Central Fiber Tracker (CFT) is the second stage of tracking a particle will reach as it leaves an interaction in the beampipe.

2.4.1 Preshower Detectors

Two more scintillation based detectors, the Central Preshower (CPS) and the Forward Preshower (FPS), share the electronics that readout the CFT. The CPS is located between the superconducting solenoid and the Central Calorimeter (described in Section 2.6), about 71 cm from the center of the beampipe. A layer of lead between the solenoid and the CPS is designed to create a total of two radiation lengths, between the solenoid and the lead, across all rapidities leading into the CPS. The CPS is assembled in three layers, one inner axial and two outer stereo layers, the latter offset about 20° in either direction from the axis. Each layer is formed from a double layer

of extruded triangular prisms of scintillating material with a cylindrical wavelength shifting fiber inserted in the center of each prism. These scintillating triangles fit into each other to create a "flat" surface for the inner and outer face of each layer. The base of the triangular prism is about 0.70 cm wide, and the fiber-to-fiber spacing of the wavelength shifting fibers is about 0.35 cm. The CPS is 273 cm long.

The FPS is made from panels of triangular scintillator strips containing wavelength shifting fibers, much like the CPS. The FPS consists of an inner layer of scintillator, followed by a sheet of lead designed to supply two radiation lengths of material across all rapidities within the FPS, then a second set of scintillators before the surface of the End-Cap Calorimeter. Both the inner and the outer layers of scintillators are made out of two double layers of triangular prism scintillators, the first double layer set at an angle with respect to the second, for stereo readout both before and after the lead.

2.5 Luminosity Monitor

The DØ luminosity monitor consists of two arrays of 24 plastic scintillator wedges arranged in rings around the beampipe at $z = \pm 140$ cm in the forward region of the detector, just before the calorimeter. These arrays cover the psuedorapidity range of $2.7 < |\eta| < 4.4$. The configuration of an array is shown in Figure 2.5.

Instantaneous luminosity measurements at DØ are based on counting the number of empty bunch crossings, considering the probability of not observing an inelastic

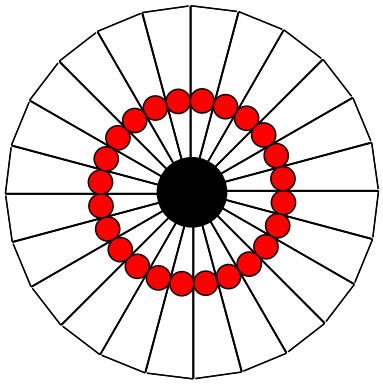

Figure 2.5 : A single 24 wedge array from the luminosity monitoring system. The red circles represent photomultiplier tube locations.

event is:

$$P(0) = e^{-\sigma_{eff}\mathcal{L}/\nu}[2e^{\sigma_{SS}\mathcal{L}/2\nu} - e^{\sigma_{SS}\mathcal{L}/\nu}] \tag{2.6}$$

where $\mathcal{L}$ is the per-bunch luminosity, σ_{eff} is the effective inelastic $p\bar{p}$ cross section for firing both luminosity monitor arrays, σ_{SS} is the similar cross section for firing only one array, and ν is the Tevatron bunch rotation frequency. The CDF and DØ experiments have chosen to base their luminosity measurements off of the same $p\bar{p}$ inelastic cross section of 60.7 ± 2.4 mb [15]. The effective cross sections for DØ RunIIa data are $\sigma_{eff} = 48.0 \pm 0.9$ mb and $\sigma_{SS} = 9.35 \pm 0.13$ [16].

An average instantaneous luminosity is determined for each one-minute chunk of time during data taking. Interruptions in data taking during a given minute of time or problems with the luminosity monitor itself will flag that minute's "luminosity block" as badly measured. Such bad luminosity blocks are ignored in this analysis.

2.6 Calorimeter

Direct particle energy measurements in DØ detector are based on a liquid argon-uranium compensating sampling calorimeter, illustrated in Figure 2.6. Only neutrinos, which are unlikely to interact with any part of DØ, and muons, which will minimally ionize the small portion of the calorimeter they pass through, are expected to leave the calorimeter. Grounded absorber plates, fabricated from uranium, copper or stainless steel, induce particles to shower. Any charged secondary particles within that shower then ionize liquid argon within the system, creating a charge that can be collected on high voltage readout boards within the calorimeter. The electron drift time across the 2.3 mm liquid argon gap is about 450 ns. The uranium plates, the liquid argon, the charge collection plates and their readout circuits create the basic "cells" within the DØ calorimeter. A calorimeter cell is illustrated in Figure 2.7.

Typically, a hadronic shower will produce some electrically neutral particles, which won't ionize the liquid argon and contribute to the shower's energy measurement. For this reason, the relative response of a calorimeter's electromagnetic portion and it's hadronic portion are not equal. A compensating calorimeter attempts to equalize the electromagnetic and hadronic response. At DØ, the compensating effect is produced through the specific choice of the relative thicknesses of absorber and active layers, and through the use of uranium as an absorber material in much of the calorimeter. Fission from slow moving neutrons in the uranium absorber plates produces extra charged particles in the liquid argon that contribute to the hadronic shower's energy

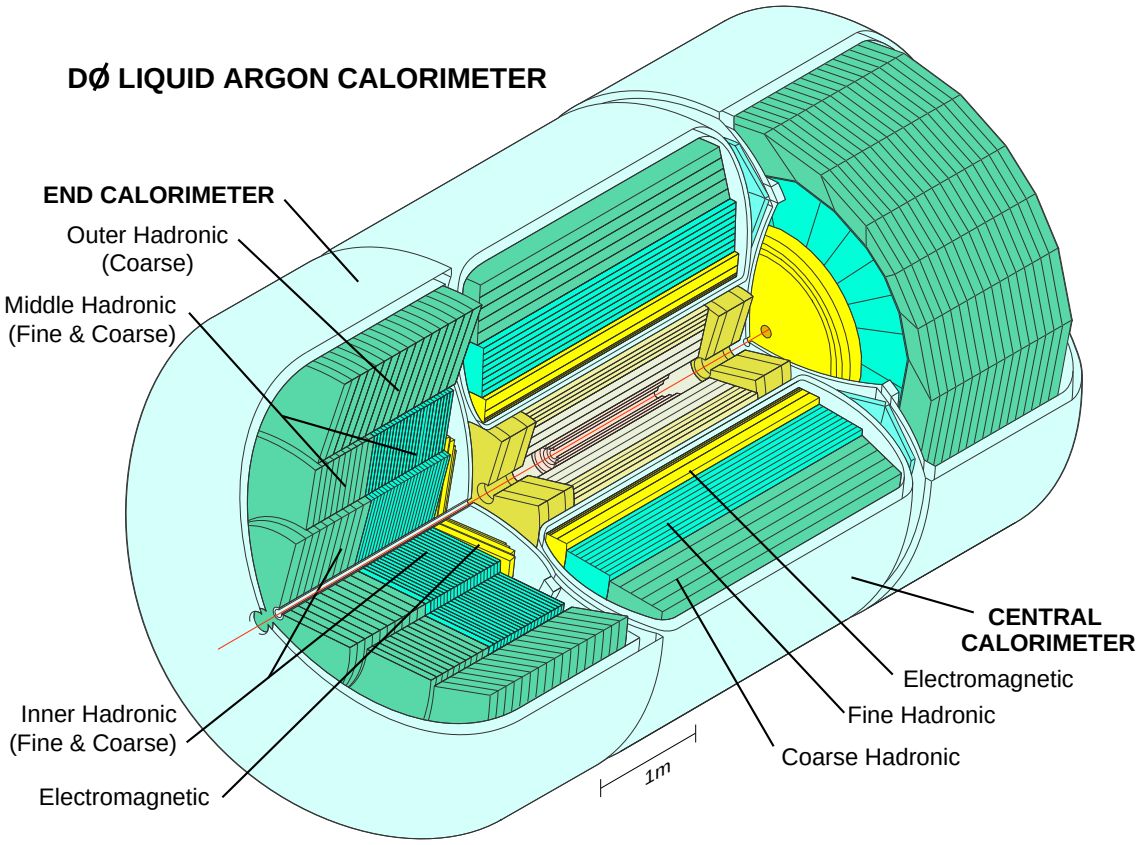

Figure 2.6 : The Liquid Argon Calorimeter is broken into three sections, the Central Calorimeter (CC) and two End-Cap Calorimeters (ECs). Within each of these sections, there are three layers of different cells, the electromagnetic (EM), fine hadronic (FH), and course hadronic (CH). Cells typically have resolutions of $\Delta\eta = 0.1$ and $\Delta\phi = 2\pi/64 \approx 0.1$.

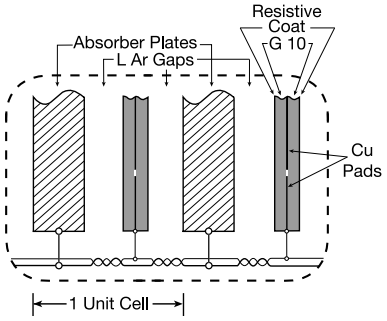

Figure 2.7 : Illustration of a calorimeter cell, including the absorber plate, liquid argon gap, and readout plate.

measurement.

The calorimeter itself is divided into three major sections, the Central Calorimeter (CC), and two End-Cap calorimeters (EC), as seen in Figure 2.6. There are three layers of cell types in each section. The innermost electromagnetic (EM) layer, a fine hadronic (FH) layer beyond that, and an outermost course hadronic (CH) layer. Individual cells are always aligned perpendicularly to their absorber plates. Cells in the CC are always aligned perpendicular to the axis of the beampipe, while EC cells are generally aligned parallel to the beam axis. Cell boundaries are arranged such that cells are centered along a line of constant psuedorapidity. Thus, cell boundaries are staggered between the EM, FH and CH layers. "Towers" of cells are defined along such lines of psuedorapidity, as illustrated in Figure 2.8.

There are four layers of cells in EM regions of the calorimeter, which use absorber plates of uranium. The absorber thickness for each layer of the calorimeter is presented in Table 2.1. There are about 4.0 radiation lengths (X_0) of material between the interaction region and the calorimeter at $\eta = 0$, and 4.4 X_0 at $\eta = 2$. The absorber plates in the FH layer are composed of uranium doped with 2% niobium, while the CH layer absorber material is copper in the CC and stainless steel in the EC. Typically, cells in each layer cover about $\Delta\eta = 0.1$ and $\Delta\phi = 2\pi/64 \approx 0.1$, though the third layer of an EM region has twice the η and ϕ resolution.

To correct for energy deposited in the uninsturmented cryostat walls and support structures, which take up most of the region between $0.8 \leq \eta \leq 1.4$, intercryostat de-

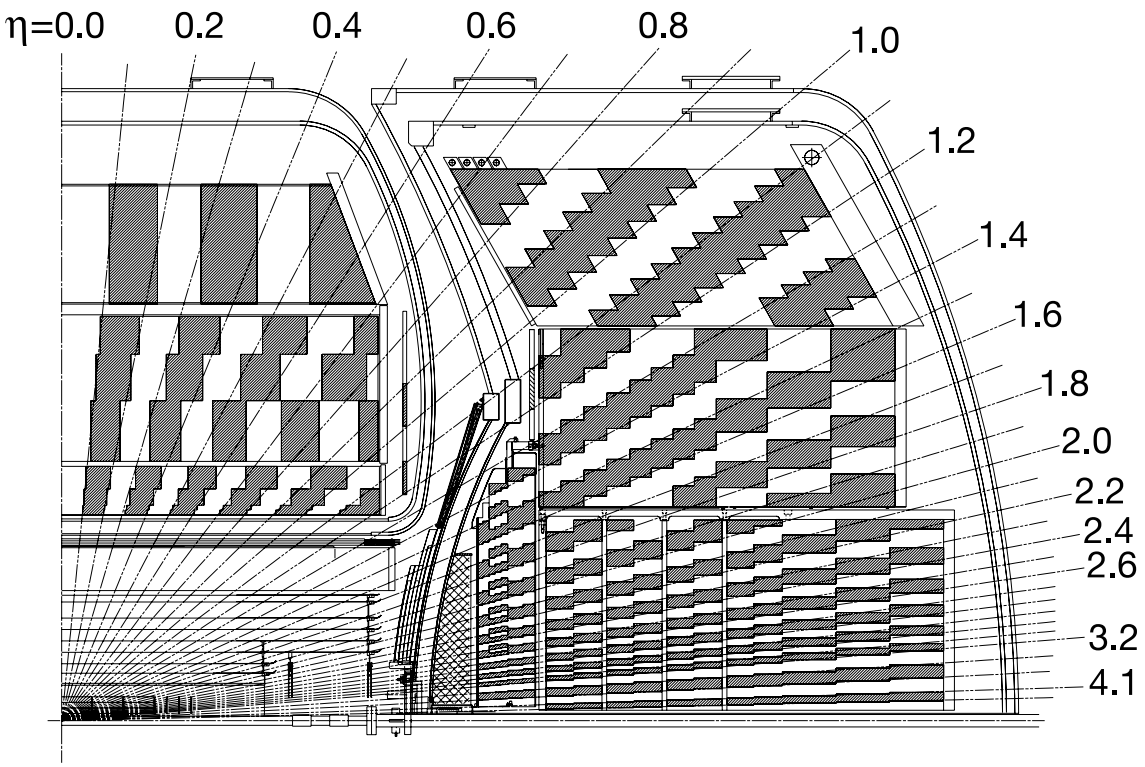

Figure 2.8 : Calorimeter cells are arranged into projective towers in η. Alternating shaded regions indicate projective tower structure.

Layer	CC	EC
EM 1	1.4	1.6
EM 2	2.0	2.6
EM 3	6.8	7.9
EM 4	9.8	9.3
FH 1	1.3	1.1
FH 2	1.0	1.1
FH 3	0.76	1.1
CH	3.2	4.4
Outer CH	—	6.0

Table 2.1 : Calorimeter absorber thickness for each readout layer. Electromagnetic absorber layers are measured in radiation lengths (X_0) and hadronic absorber layers are measured in nuclear interaction lengths (λ_A). Layers are numbered in increasing order of distance from the interaction point. The first EM layer includes all inactive material in the calorimeter before the first liquid argon gap. [17]

tectors (ICD) were mounted on the face of either EC. The ICD is made of scintillating tiles that mimic the η and ϕ resolution of the calorimeter. This system provides a good approximation of the standard sampling of the CC and ECs.

2.7 Muon System

Lying outside the calorimeter, the only particles that reach the muon system from the interaction point in the beampipe are muons and neutrinos. Of these, only the muons will be detected. The muon system consists of five separate solid-iron toroidal magnets, proportional drift tube (PDT) chambers, mini-drift tube (MDT) chambers, and scintillating panels. See Figure 2.9 for a schematic of the drift chambers and Figure 2.10 for a schematic of the scintillating panels. The system is divided into three layers, labeled A, B, and C, where A is the closest layer to the interaction

region, and the toroidal magnet is located between layers A and B. These layers can be identified clearly in Figure 2.2.

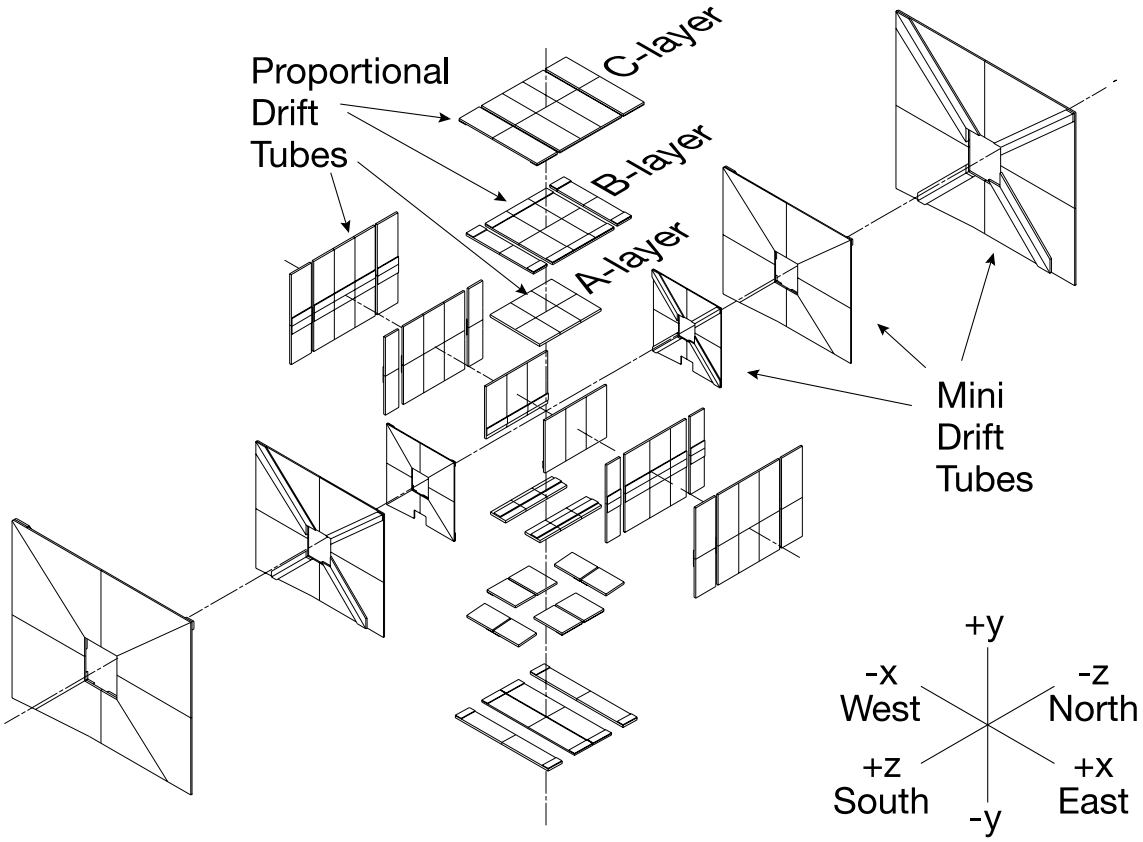

Figure 2.9 : Exploded view of the drift chamber arrangement in the DØ muon system.

In the central region, where $|\eta| < 1$, each of the three layers contain PDTs and, additionally, layers A and C contain scintillating panels. Because the maximum drift time in the PDTs is 750 ns but the time between bunch crossings is 396 ns, the scintillation counters are the only method available to trigger on muons in this central region. In the forward regions, where $1 > |\eta| > 2$, all three muon system layers have both MDTs and scintillating panels, with four layers of MDTs in layer A while layers

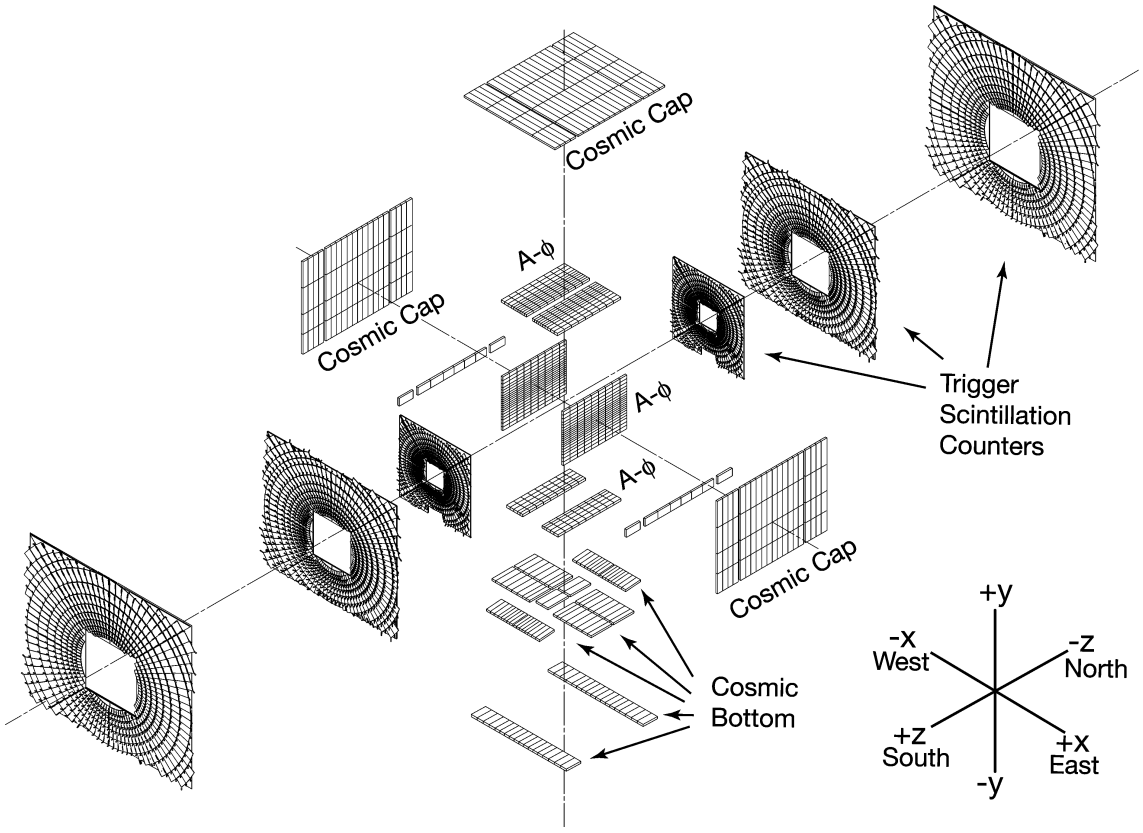

Figure 2.10 : Exploded view of the scintillating panel arrangement in the DØ muon system.

B and C have three layers of MDTs each. The scintillators in each of these forward layers are arranged in an $r - \phi$ geometry. The forward muon system is capable of triggering on both scintillator and MDT hits.

2.8 Trigger Systems at DØ

During normal operation of the Tevatron, there are about 1.7 million proton-antiproton bunch crossings per second occurring inside of the DØ collider detector. Every beam crossing has the potential to produce an interesting physics event, but there is also the possibility that the proton and antiproton bunches fail to interact with each other at all, or only interact diffractively and fail to produce high p_T particles. Additionally, the average raw detector readout for each event is on the order of 200 KB, so it would take a bandwidth of over 300 GB/s to record information from every beam crossing. Therefore, from both a technical and an experimental point of view, it is important to somehow filter events in order to select the interesting event candidates that are worth studying in detail, and only write those events to permanent storage. This filtering process is known as "triggering."

Generally, the most interesting events at DØ are produced through hard scattering between partons during a bunch crossing, where the combined energy of the partons is capable of producing massive particles, such as top quark pairs, or W and Z bosons. The signature of a hard scatter is a high p_T jet or lepton, which are the initial indicators that an event may be worth triggering. A track vertex transversely

displaced from the beampipe may indicate a b or c quark jet, while a large unbalance of energy in the transverse plane may indicate the presence of high p_T neutrinos. These and other conditions are also considered during the triggering process, in order to capture a diverse set of events capable of being used for various studies of the Standard Model and new phenomena.

The DØ triggering system is broken into three major parts, designed to provide more rigorous constraints upon the data at each successive level. At Level 1 (L1), this filtering consists of pattern-matching hardware and firmware that attempt to find charged particle track candidates in the CFT, electron, photon and jet candidates in the calorimeter, and muon candidates in the muon system. This allows a quick measurement of particle properties, though information is not as detailed as during offline reconstruction. Due to time constraints, the SMT is the only major subdetector not considered at L1. Whereas the collision rate at DØ is about 1.7 MHz, the L1 trigger only accepts and passes on events at a rate of about 2 kHz to the Level 2 trigger. Level 2 (L2) CPUs and digital signal processors combine L1 data across subdetectors to provide additional information on found objects. The L2 trigger accepts events at a rate of about 1 kHz. The computer farms for the Level 3 (L3) trigger perform simple event reconstruction including particle identification. Each stage of the trigger system provides a chance to veto an event. Thus, the acceptance rate drops through each stage until the selected events are written out to tape at the maximal allowed rate of 50 Hz.[18]

Individual trigger terms are formed at each trigger level, and specific combinations of these trigger terms must be satisfied in order for an event to be accepted and written to tape. A specific "AND" of such L1, L2 and L3 trigger terms is referred to as a "trigger," and every event written to tape must satisfy at least one such trigger condition. Certain triggers may be "prescaled" if their firing rate is too high. A prescale is attached to the L1 portion of a trigger and defines the probability for an event to be accepted at L1 should it's L1 conditions be satisfied. If a trigger has a prescale of 5, then one in five events that satisfy the L1 condition of that trigger are randomly selected to continue in the triggering process, while the remaining events are discarded. Certain triggers avoid imposing a prescale by using the AND of multiple L1 conditions, possibly from multiple subdetectors. The list of triggers and the prescales for those triggers can be modified between each global physics run of the detector. Trigger lists and prescales are defined for given ranges of instantaneous luminosity, in order to optimize the L1, L2 and L3 accept rates for a given trigger list.

2.8.1 Level 1 Trigger

Limited information is available at L1, due to the very tight time restriction imposed by the beam crossing structure. Detector readout is buffered, providing 4.2 μs for an L1 decision to be made. In this short amount of time, only simple signatures within the CFT, calorimeter and muon subdetectors can be considered.

In the calorimeter, L1 triggers are based on the amount of E_T deposited in a

0.2×0.2 projective tower in η and ϕ. Typical L1 calorimeter triggers are based on finding one or more such projective towers that pass a certain threshold of E_T. Typical L1 calorimeter trigger terms may involve finding one electromagnetic calorimeter trigger tower with $E_T > 11$ GeV or two electromagnetic towers each with $E_T > 6$ GeV. Similar terms exist for jet candidates, using the EM and hadronic calorimeter information. Often an AND of one- and two-tower trigger terms is used to further reduce the L1 accept rate of an event, such as requiring two trigger towers with $E_T > 3$ GeV, one of which must have $E_T > 9$ GeV.

The CFT L1 trigger terms, provided by the Central Track Trigger system (CTT), are based on roughly measuring the momentum of charged tracks. The CTT receives a binary list of hit axial fibers from the CFT and CPS, dividing the hits into 80 sectors of 4.5deg each for faster processing. Track candidates are determined through hardware based pattern matching, using FPGAs that are preprogrammed with track patterns. This pattern matching system requires hits in all 8 axial layers of the CFT in order to identify a track, though the system is highly efficient if hits in all 8 layers are present [19]. Tracks are roughly binned by their p_T, depending on whether they pass thresholds at 1.5, 3, 5 and 10 GeV. Tracks are considered isolated if no other tracks are found in their own sector or their two neighboring sectors. Tracks can also be matched to CPS clusters. The CTT produces trigger terms that specify if one or two tracks were found above each p_T threshold, including separate lists for tracks that are either isolated, CPS-matched, or both. The CTT also provides input to the L1

muon trigger system, so that muons can be roughly matched to central tracks during L1 triggering.

The L1 muon system uses information from the muon system wire chambers (PDTs in the central muon system and MDTs in the forward muon system) and scintillator panels, in addition to track information from the CTT. Trigger terms can involve individual scintillator hits, which must pass a timing cut near the beam crossing, or matching scintillator hits along a road across layers of the muon system. Track stubs can be determined for individual layers of the muon system, and track stubs that match across different layers of the muon system can be used to determine a rough p_T measurement, though it takes approximately 3 GeV to pass through the toroidal magnet between the A and B layers of the muon system. Terms can involve the matching between any of the scintillating panel system, the wire chamber system, or the CTT.

2.8.2 Level 2 Trigger

The L2 system consists of both software and firmware, and is capable of roughly defining physics objects, such as electrons, muons, jets and tracks, across subdetectors. About 100 μs is available for an L2 decision, which allows time for the SMT to participate in triggering decisions through the Silicon Track Trigger (STT). The STT receives a list of tracks from the CTT, which are used as seeds for determining whether any SMT hits are consistent with the CTT track.

The information available for a decision at L2 includes:

- L1 trigger terms that fired in the event
- Tracks from the CTT and STT systems
- Clusters from the CPS and FPS
- Further refined electron/photon, jet and $\not\!\!E_T$ information from the calorimeter
- Muons found in the central and forward muon system

All of this information is routed to a global L2 software process that is capable of generating trigger terms based on the the roughly defined physics objects available. Rudimentary calculations of relationships between physics objects are available, such as η and ϕ discrimination and invariant mass calculation.

2.8.3 Level 3 Trigger

The L3 trigger decision is based on the full detector output for each event. After an L2 accept occurs, the buffered data from all subdetectors is routed to a node on a large computer farm, where the raw detector readout is reconstructed. This reconstruction is optimized for speed, and is a simplified version of the full event reconstruction that occurs after an event has been written to tape. About 50 ms is devoted to the L3 decision for each event.

Generally, trigger decisions at L3 involve reconstructing the physics objects of interested in an event and making a selection based on their properties. Charged

particle tracks are reconstructed using CFT and SMT information, and a primary vertex position is estimated. Electron, muon, tau and jet candidates are reconstructed using the detector precision readout, and quantities such as $\not\!\!E_T$, the invariant mass between objects, and the scalar sum of jet activity in the event are determined. A trigger decision can be made based on any combination of these quantities.

Chapter 3

Reconstruction

3.1 Event Reconstruction at DØ

The raw information produced by the DØ collider detector consists of digital read-out values from nearly one million individual channels. This information must be processed by DØ specific reconstruction software in order to produce the information that is useful to physicists eager to probe the fundamental universe. The output of the reconstruction software contains information about particle candidates such as their energy, momentum, spatial position and charge. Charged particle tracks, electromagnetic calorimeter clusters, muons, and hadronic jets are all important objects in this analysis, so their reconstruction will be covered in detail.

3.2 Charged Particle Track Reconstruction

Two algorithms are used to find charged particle tracks inside the tracking volume of DØ, the Histogramming Track Finder (HTF) and the Alternative Algorithm (AA) [20, 21]. The final track list is the combination of all tracks produced by both algorithms with duplicate tracks removed.

3.2.1 Histogramming Track Finder Algorithm

In a homogeneous magnetic field, $\vec{B}$, with no material present, the trajectory of a particle with charge q in the plane perpendicular to the magnetic field will be a circle. This circle can be parameterized in (ρ, d_0, ϕ) space, where $\rho = qB/p_T$ is the track curvature, d_0 is the distance of closest approach to the coordinate origin, and ϕ is the direction of the track at the point of closest approach. The tracks of interest at DØ are those with low impact parameter, where $d_0 \sim 0$, which have been produced due to a beam interaction.

The HTF method for finding tracks is based on a coordinate transformation of tracking hits from (x, y) space to (ρ, ϕ) space, assuming $d_0 \sim 0$. While any two tracking hits correspond to a single point in (ρ, ϕ) space, a single tracking hit constrained by the origin translates into a line in (ρ, ϕ), as illustrated in Figure 3.1. Multiple tracking hits from the same track will make lines of different slopes in (ρ, ϕ) that all intersect at the same point. By imposing the constraint that $-\rho_0 < \rho < \rho_0$, where ρ_0 corresponds to a minimum p_T of 0.5 GeV, then dividing (ρ, ϕ) space into histogram cells, the number of calculations necessary to process all tracking hits is $\sim N_h \times N_\rho$, where N_h is the number of tracking hits and N_ρ is the number of divisions in ρ.

After the initial processing of all track hits, bins in the (ρ, ϕ) histogram above a certain threshold are considered as track candidates and are further studied. Candidate tracks are passed through a two-dimensional Kalman filter, which determines the parameters of the track trajectory, taking into account material effects and allowing

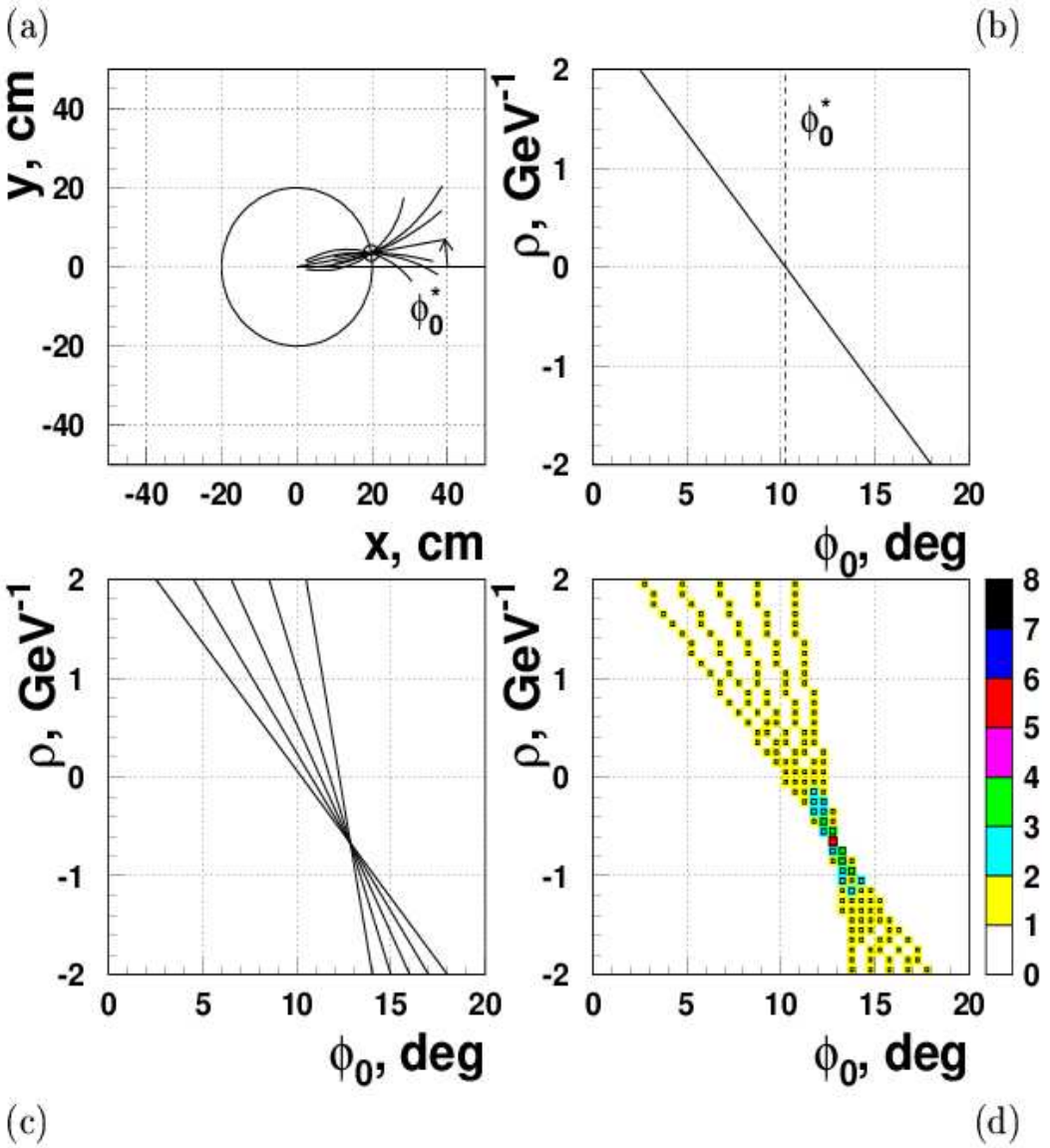

Figure 3.1 : The HTF method applied to a single 1.5 GeV track with 5 hits: (a) Various possible trajectories for a given hit. (b) Translation of a single hit into (ρ, ϕ) parameter space. (c) Lines from hits along a track will intersect at a single point in parameter space. (d) The intersection point becomes a peak in the (ρ, ϕ) histogram. [20]

for missed hits. The Kalman filter accepts or rejects candidates based on the total number of hits in a track, the number of lost hits inside a track, and the χ^2 of the fit to track hits.

Finally, z information is used in order to reduce the number of fake track candidates. A second histogramming is performed, this time considering the coordinate space (r, z) and the parameter space (z_0, C), where z_0 is the position of the track origin along the z axis and $C = dz/dr$ is the track inclination in (r, z) space. A second technique based on η-splitting is also applied to further reduce fake track candidates. A positive and negative η hypothesis is tested on each track. A track with positive η must have η increase with each successive hit as r increases along the track, and similarly a negative η track is expected to have η decrease as r increases. A track that cannot satisfy one of these two hypotheses is rejected.

There are two strategies for implementing the HTF algorithm. The first begins by analyzing SMT hits, attempting to find track candidates in (ρ, ϕ) space that have at least 4 hits. Track candidates are then filtered, examined in (z_0, C) space, filtered again, and finally η-splitting is performed. The remaining track candidates are then passed through a three-dimensional Kalman filter, which builds the SMT tracks. Finally, an attempt is made to extrapolate the track into the CFT to build a complete track.

The second strategy is very similar, only beginning with CFT hits. Initial track candidates are based on only the CFT axial layers, and must have 7 out of the 8

possible hits after histogramming in (ρ, ϕ) space. For each track candidate, every possible three-dimensional hit from CFT stereo layer information is considered at further stages of the algorithm. The second strategy continues similarly to the first, until finally the CFT track is extrapolated into the SMT in order to attempt to build a complete track.

Both strategies are run independently, their results are combined, and duplicate tracks are removed.

3.2.2 Alternative Algorithm

The general strategy of the AA for track reconstruction is to construct a large pool of track hypotheses based on extending seed clusters of tracking hits, reorder those hypotheses based on certain quality criteria, then select tracks in order from the hypothesis pool, removing any overlapping hypotheses from the pool with each selected track until the hypothesis pool is empty.

Track reconstruction begins in the SMT barrels and F-disks, where initial track hypotheses are constructed from sets of three hits in (x, y) space. The innermost of these three hits can be any hit in an SMT barrel or F-disk. The next tracking hit may be in any layer of the SMT beyond the first hit and must satisfy $\Delta\phi < 0.08$, where $\Delta\phi$ is measured with respect to the line through the beam-spot and the first tracking hit. The third hit may be in any layer of the SMT beyond the second hit, and must satisfy the constraints that the radius of the circle defined by the three hits

is greater than 30 cm (corresponding to $p_T = 180$ MeV in a 2 T magnetic field), and that the impact parameter of the track with respect to the beam spot is less than 2.5 cm. Finally, the fit of the tracking hypothesis must have $\chi^2/dof < 16$. Each tracking hypothesis includes one axial and at least one stereo projection, depending on the specific stereo information associated with the set of initial hits.

Each track hypothesis is then extrapolated outward to the next layer of the SMT or CFT, where any hits within the projected window are considered as additional track hits. Multiple hits within the projected window will create multiple track hypotheses, though additional hits must continue to satisfy a χ^2 constraint on the track fit. Many stereo projections may exist for a given track hypotheses, though additional information from hits in each layer of tracking may constrain the possible stereo projects of a track. Missed layers are allowed, to a certain extent, where a layer is considered missed if the tracking layer has no hits in the expectation window. A separate count of inside, forward and backward misses are maintained, where inside misses occur between two layers with hits, forward misses occur outside of the outermost tracking hit, and backward misses occur inside of the innermost tracking hit. A track hypothesis continues construction until it reaches the outermost layer of tracking or three forward misses are found.

A track hypothesis must satisfy the following conditions before it is added to the hypothesis pool:

- At least four tracking layers must have coincidental axial and stereo layer hits

- Track hypothesis has at most 3 inside misses (no more than 2 within SMT)
- A hypothesis with an inside miss has no more than 4 inside plus forward or 3 inside plus backward misses
- Track hypothesis has at most 6 forward plus backward misses
- $N_{hits}/5 \geq N_{misses}$

The track hypothesis pool is ordered based on the number of hits, the number of misses, and the track χ^2 in that priority order. The highest priority is given to track hypotheses with the most hits. In the case of two hypotheses with an equal number of track hits, highest priority is given to candidates with the lowest number of total forward, inside and backward misses. In the case that the number of hits and total misses are equal, track hypotheses with the lowest χ^2 are given the highest priority.

An initial set of track candidates is selected from the pool of track hypotheses, selecting candidates in order of priority and ignoring hypotheses that share too many hits with a previously selected track candidate. This set of track candidates is used to estimate the track vertices within the event. All track hypotheses with a small impact parameter are given two additional "hits" and the pool of track hypotheses is reordered. Finally, track selection is repeated again in the new priority order and track hypotheses that share too many hits with an accepted track are removed from the hypothesis pool.

The AA scheme is repeated a second time, using CFT hits as track hypothesis

seeds with an additional constraint due to the track vertices found during the first pass of the algorithm. The track vertex constraint reduces the number of stereo projections of CFT seeds, allowing for more efficient processing of the algorithm. These CFT tracks are extrapolated into the SMT, which allows for finding tracks with with less than 3 SMT hits.

The final track list is the combination of SMT and CFT seeded tracks, with duplicate tracks removed. The efficiency for finding a track within the fiducial region of the DØ tracking system is $0.930 \pm 0.001\%$ [22].

3.3 Electromagnetic Cluster and Electron Reconstruction

In this analysis, an electron is defined by a track from the central tracking systems that points to a cluster of energy in the electromagnetic calorimeter. During event reconstruction, tracks and EM clusters are found by independent subdetector specific algorithms. Electron properties are then defined by the combination of the information from the central track and the EM cluster in the calorimeter.

3.3.1 Electromagnetic Cluster Reconstruction

Electromagnetic cluster reconstruction begins with a seed EM energy deposit in the calorimeter that is used to attempt to find an electron- or photon-like deposit of energy in the calorimeter [23]. A seed EM cell calorimeter tower with at least 0.5 GeV of transverse energy is the basis of a simple cone algorithm, which sums calorimeter cells

within $\Delta R < 0.4$, where $\Delta R = \sqrt{\Delta\eta^2 + \Delta\phi^2}$. A simple cone cluster is accepted if it has $E_T > 1.5$ GeV and the EM portion of the calorimeter contains at least 90% of the total energy in the cone.

An isolation ratio is computed based on the energy distribution within the $\Delta R < 0.4$ cone. The total energy, E_{Tot}, is computed for all layers of the calorimeter within the full cone and a core energy, E_{Core} is computed for the EM layers of the calorimeter within $\Delta R < 0.2$ of the seed position. If the isolation ratio $(E_{Tot} - E_{Core})/E_{Core} < 0.2$, the cluster is accepted as an EM object. This shower shape cut is designed to reject hadronic showers, which tend to deposit energy into deeper layers of the calorimeter, and tend to have wider transverse shower shapes.

The EM object energy is adjusted for a matching preshower cluster, if one exists. The highest energy CPS cluster within a window of $\eta \times \phi = 0.1 \times 0.1$ about a CC EM object position is considered a match. Similarly, the highest energy FPS cluster within a window of $\theta \times \phi = 0.1 \times 0.1$ about an EC EM object is considered a match. If a matching preshower cluster is found, the EM object's energy is adjusted to include the contribution from the preshower cluster, and the EM object's position is adjusted to reflect the preshower cluster position.

An EM object is considered matched to a track if a central track is spatially matched to within $\eta \times \phi = 0.5 \times 0.5$ of the cluster. The closest spatially matching track to the EM object is used. If an EM object is matched to a track, then the track information is used for η, ϕ and vertex z position.

The energy resolution, σE, of an EM object with energy E is expressed as a function of a constant term, C, a sampling term, S, and a noise term, N, as:

$$\frac{\sigma E}{E} = \sqrt{C^2 + \frac{S^2}{E} + \frac{N^2}{E^2}}. \tag{3.1}$$

The values of C, S and N are presented in Table 3.1.

	CC	EC
Constant Term (C)	$3.73 \pm 0.28\%$	$2.03 \pm 0.59\%$
Sampling Term (S)	0.150 $\sqrt{\text{GeV}}$	0.206 $\sqrt{\text{GeV}}$
Noise Term (N)	0.29 GeV	0.29 GeV

Table 3.1 : EM cluster energy resolution parameters for the CC and EC. [24]

3.3.2 Electron Identification

Additional information is calculated for EM objects that can be used to discriminate electrons and positrons from hadronic backgrounds. A calorimeter shower shape cut, defined by the H-matrix, and an electron likelihood cut each add discrimination power to electron selection.

The H-matrix quantity is a shower shape χ^2 test based on seven correlated variables [25]. The variables used are the fractional energy deposited in each of the four layers of the EM calorimeter, the total EM energy, the vertex z position, and the transverse shower width in ϕ. A 7×7 covariance matrix, M, is built for each calorimeter tower in η, using the symmetry of the calorimeter to apply the same matrix to towers at the same absolute value of η. These 37 matrices are trained on

Monte Carlo (MC) electrons, so that for a given pair of variables, x_i and x_j:

$$M_{ij} = \frac{1}{N}\sum_{n=1}^{N}(x_i^n - \bar{x}_i)(x_j^n - \bar{x}_j) \tag{3.2}$$

where the sum is performed over N reference electrons. To measure the consistency between the shape of an observed cluster with the estimated shape of an electromagnetic cluster, χ^2_{hm} is computed using the inverted matrix $M^{-1} = H$:

$$\chi^2_{hm} = \sum_{i,j=1}^{7}(x_i - \bar{x}_i)H_{ij}(x_j - \bar{x}_j) \tag{3.3}$$

EM objects that closely resemble electrons will have low values of χ^2_{hm}. This variable is used as an input to the electron likelihood function.

The electron likelihood discriminates based on properties of a candidate object's track and EM cluster, and the additional central tracks found in close proximity to the candidate [26, 27]. These quantities are used to calculate the electron likelihood:

- E_T/p_T, where E_T is determined by the calorimeter and p_T by the central track. An electron should have $E_T/p_T \sim 1$.

- χ^2_{hm}, as described above, which can discriminate electron-like calorimeter energy deposits from photon and hadronic deposits.

- The EM layer fraction of the total calorimeter energy in a $\Delta R < 0.4$ cone, which tends to be near 1 for an electron, and must be greater than 0.9 in an electron candidate.

- Distance of closest approach to primary vertex, which is the shortest perpendicular distance to a track from a line through the primary vertex that is parallel to the beam axis.

- Number of central tracks in $\Delta R < 0.05$ cone (candidate track included). Photon conversions that fake an electron often have a second track very near to the electron candidate's track.

- Total p_T of tracks in $\Delta R < 0.4$ cone around candidate track (candidate track excluded). Hadronic jets that fake electrons often produce many high p_T tracks in the vicinity of the candidate.

- Spatial track match χ^2 probability, which can discriminate fake tracks that point to an EM cluster.

The spatial track match χ^2 probability is defined by:

$$\chi^2 = (\frac{\Delta\phi}{\sigma\phi})^2 + (\frac{\Delta z}{\sigma z})^2 \tag{3.4}$$

where $\Delta\phi$ and Δz are the ϕ and z separation between the EM cluster position at the finely segmented third layer of the EM calorimeter and the extrapolated track position, and $\sigma\phi$ and σz are their respective resolutions.

Distributions for each of these variables are produced with both an electron-enriched $Z \rightarrow ee$ data sample, and a background sample consisting EM+jet events where the EM object is back-to-back with a jet. The distributions are smoothed

using linear smoothing techniques and normalized to a unit area in order to represent a probability distribution function for each variable. The probability distribution functions are used to assign a probability for a given object to be signal (P_{sig}) or background (P_{bkg}) based on the seven variables. Assuming there are no correlations, the individual probabilities for the seven variables, x_i, translate into an overall probability in this manner:

$$P(\mathbf{x}) = P(x_1, \ldots, x_7) = \prod_{i=1}^{7} P_i(x_i) \tag{3.5}$$

A likelihood, $\mathcal{L}$, is defined for each electron candidate based on these probabilities:

$$\mathcal{L}(\mathbf{x}) = \frac{P_{sig}(\mathbf{x})}{P_{sig}(\mathbf{x}) + P_{bkg}(\mathbf{x})} \tag{3.6}$$

Electron-like objects will tend to have $\mathcal{L}$ values near 1, while background-like objects will tend to have $\mathcal{L}$ near 0.

3.4 Hadronic Jet Reconstruction

Individual hadronic jets may deposit their energy in the calorimeter in extremely different ways, depending on the specific fragmentation of the jet in question. The ideal algorithm for jet reconstruction would lead to a scheme that consistently reproduces the characteristics of the initially produced particle and could be applied to both live and simulated events for any experimental apparatus. The jet cone algorithm used at DØ is an attempt to implement such a universal algorithm, as it can be applied equally well to MC simulated events and even data taken at other experiments, such as the Collider Detector at Fermilab (CDF). The algorithm consists of multiple

stages, where potential jets are seeded, jet candidates are created, and final jets are constructed by merging or splitting jet candidates [28, 29, 30].

A cornerstone of this algorithm is the addition scheme for items that are combined to form a composite object. The initial items may be partons or particles in MC or calorimeter cells or towers in DØ data, though eventually jet candidates may be added to these initial items or each other. Items are always combined by adding their four-momenta:

$$\mathbf{p}^J = (E^J, p^J) = \sum_i (E^i, p_x^i, p_y^i, p_z^i) \tag{3.7}$$

All kinematic quantities are derived directly from this combined four-momentum. For instance, the transverse momentum is $p_T^J = \sqrt{(p_x^J)^2 + (p_y^J)^2}$, the azimuthal angle is $\phi^J = \tan^{-1}(p_y^J/p_x^J)$, and the rapidity is $y^J = \frac{1}{2}\ln\frac{E^J+p_z^J}{E^J-p_z^J}$.

For a single cell in the calorimeter, the energy portion of the cell's four-momentum is the energy measured in that cell, E_{cell}, while the momentum portion is the three-vector of magnitude $|E_{cell}|$ with direction defined by the primary vertex and the center of the cell. Initially, the individual calorimeter cells from a geometrically projective tower in η and ϕ are added to form the reconstructed tower. Only cells that pass a certain threshold above detector noise are considered. A simple cone algorithm is used to build jet preclusters out of the calorimeter towers. All towers with $p_T^J > 0.5$ GeV are sorted into an ordered list of items from highest p_T^J to lowest. The first item on this list becomes a precluster seed, P, and is removed from the list. The rest of the list is then processed in order, adding any items, I, with $\Delta R_{PI} < 0.3$ to the

precluster P and removing them from the list. This process repeats until all items are part of a precluster. All preclusters satisfying $p_T^J > 1$ GeV are used as seeds for proto-jet generation.

Proto-jets are formed by an iterative process of selecting a position and adding all items (calorimeter towers, in the case of event reconstruction) within a cone in ΔR of a specific size around that position. Two cone sizes are used during DØ reconstitution, 0.7 for JCCA jets and 0.5 for JCCB jets. The list of preclusters, ordered by descending p_T^J, provide the initial seeds for proto-jet generation. A precluster will seed a proto-jet if the precluster is separated from the closest existing proto-jet by a ΔR at least half of the considered jet cone size. Otherwise, the precluster is discarded from the list of proto-jet seeds. The proto-jet candidate position calculated during each iteration seeds the next iteration. After each iteration, the newly calculated proto-jet candidate is compared to the previous iteration's proto-jet candidate. Iterations stop when one of three conditions is satisfied:

- Proto-jet candidate has $p_T^J < 3$ GeV
- Proto-jet candidate stability: ΔR between current proto-jet candidate and it's seed is < 0.001
- Fifty iterations have occurred

Proto-jet candidates with $p_T^J < 3$ GeV are discarded. Otherwise, the proto-jet candidate is added to the list of proto-jets, as long as a duplicate proto-jet does not already

exist within $\Delta R < 0.005$ of the candidate that has p_T^J within 1% of the candidate.

Soft radiation may cause a precluster seeded jet cone algorithm to combine jets that would otherwise be separated. This effect can be minimized by creating a new list of proto-jets that are seeded by the midpoints between all of the precluster seeded proto-jets and adding them to the final list of proto-jets. No midpoint seeds are vetoed during this second proto-jet creation process, even if they are close to existent proto-jets, and no duplicate check is performed.

A final process of merging and splitting is performed on the proto-jets in order to create the final list of hadronic jets. Proto-jets are considered in descending p_T^J order. If the current proto-jet shares at least one item with any other proto-jet, the sum of the p_T of those items shared with it's highest p_T neighbor is calculated. If the shared p_T sum is greater than 50% of the p_T of the neighbor, the two proto-jets are merged, using the described addition scheme. Otherwise, the jets are split, so that each shared item is assigned to the proto-jet which is closest to it in ΔR. After any merges or splits, the list of proto-jets is reordered and the process begins again. After merging and splitting, the resultant jets are considered the final reconstructed objects. The p_T resolution of reconstructed CC jets is shown in Figure 3.2.

3.5 Muon Reconstruction

Muon objects are constructed based on wire chamber and scintillator panel hits in the muon subdetector. Track segments for each individual layer of the muon system are

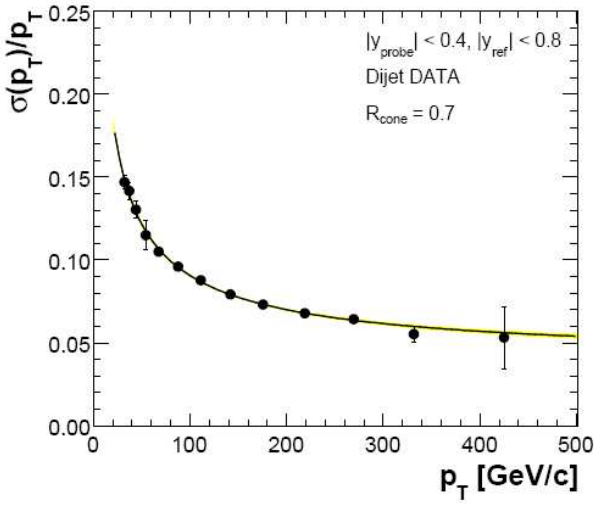

Figure 3.2 : The jet transverse momentum resolution, σ_{p_T}/p_T, for jets reconstructed in the CC. [31]

found first, then matched to scintillator hits in the same layer [32]. Track segments from either side of the muon system toroid can be matched in order to form a local p_T measurement, and central tracks can be matched to local muon tracks in order to form more accurately defined muon objects [33, 34].

Muon reconstruction begins with an algorithm that finds track stubs based on wire chamber hits in individual layers of the muon system. During this process, only a single octant in ϕ of the muon system is considered at a time, and the central muon system is considered separately from the forward muon system. Wire chambers are transformed to a special coordinate system, where wires physically extend along the z axis, wire planes are formed along the y axis, and drift circles lie in the $x-y$ plane. This allows the same algorithm to process wire hits in all parts of the muon system, regardless of the physical orientation of an individual wire chamber. An initial list of

track segments is formed based on pairs of wire hits, with certain restrictions:

- Both hits do not lie on the same drift circle
- No more than 20 cm separate the hits along the y axis
- Hits are not on the same wire plane (x axis position), unless the hits are from the top and bottom of drift circles on neighboring wires

All two-hit track segment candidates are then compared in an attempt to link larger track segments together, when hits from two segments are compatible. A sample track segment is illustrated in Fig. 3.3. These track segments are compared to scintillator hits in an attempt to refine the timing of the wire hits, and are then refit to produce a χ^2 value for the track. The two tracks with the lowest χ^2/N_{hits} are kept for each layer of an octant in the central or forward muon system.

Muon system track segments are then matched between layers. Matched segments between the B and C layers can provide tighter constraints on the final muon position. Matched track segments between the inside and outside of the muon toroidal magnet can be used to form a local measurement of the muon charge sign and p_T, as illustrated in Fig. 3.4. Local p_T measurement is restricted due to the geometry of the muon system. The minimum p_T to pass through the muon system toroid is η dependent, and tracks with $p_T \leq 3$ GeV are unlikely to reach the B/C layers of the muon system. Above $p_T \sim 10$ GeV, the resolution of the wire chambers leads to a large uncertainty on track momentum.

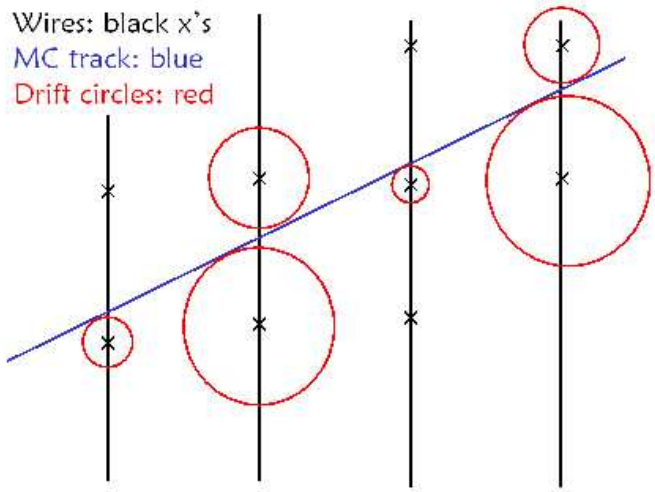

Figure 3.3 : A local track segment in the muon system. The "×" marks represent wires that extend out of the page, red circles represent wire hit drift circles, and the blue line represents the track candidate. [32]

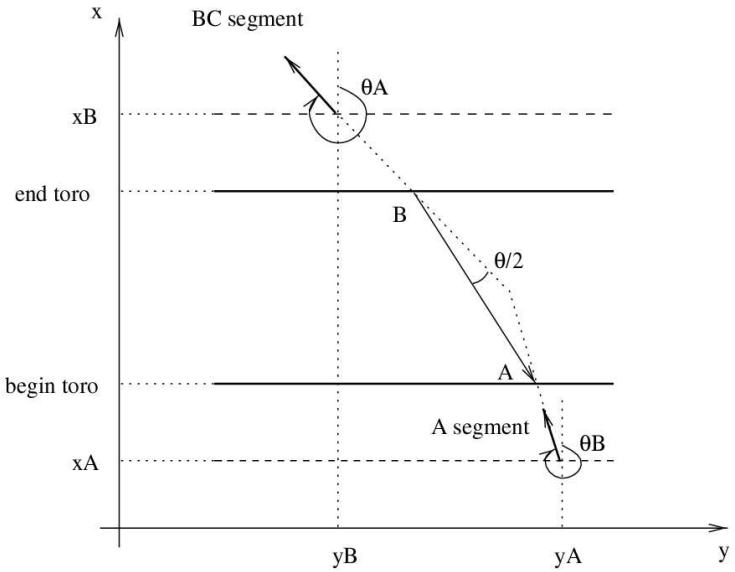

Figure 3.4 : A local measurement of muon charge sign and p_T is possible by considering the deflection angle of the track through the toroidal magnet. [33]

A match to a central track greatly improves muon p_T resolution. Local muon tracks with a p_T measurement can be extrapolated into the central tracking volume to search for track matches, and central tracks can be extrapolated out to the muon system layers to find matches to track stubs. The central track momentum is used for matches to individual stubs, while a global fit provides kinematic information for central tracks that are matched to muons with local p_T measurements. The muon transverse momentum resolution, σ_{p_T}/p_T, for various types of central track matches is shown in Figure 3.5.

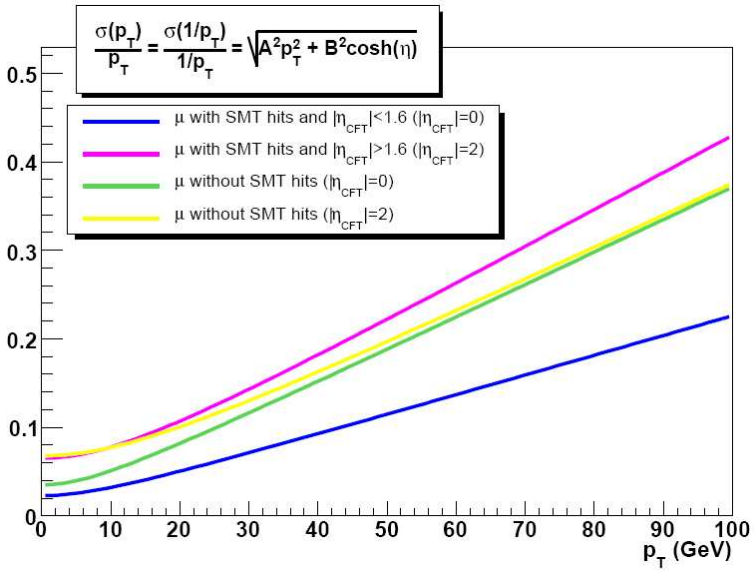

Figure 3.5 : The transverse momentum resolution, σ_{p_T}/p_T, for muons with various types track matches. [35]

3.5.1 Muon Quality

Muons are grouped by the quality of their muon system information, their isolation from charged particle tracks and calorimeter energy deposits, and the quality of their match to a central track, if one exists. This analysis requires muons that meet specific requirements in each of these categories.

Within the local muon system, muons must meet "medium" identification requirements. This definition requires that a muon has an A layer track stub matched to A layer scintillator activity and a B/C layer track stub matched to B/C layer scintillator activity. An exception is made in the central muon system for $5\pi/4 < \phi < 7\pi/4$, where calorimeter support structure limits muon system coverage. In this region, a track stub matched to scintillator activity in any layer is sufficient. By requiring a hit outside of the muon toroid, fake muons from jets that punch through the calorimeter is highly suppressed. Allowing a looser constraint in the region $5\pi/4 < \phi < 7\pi/4$ retains a significant amount of acceptance that would otherwise be lost.

Muons are required to have a "medium" quality match to a central track. This requires that the distance of closest approach of the central track to the primary vertex position is < 0.2 cm if the central track has no SMT hits and is < 0.02 cm if the central track has SMT hits. Additionally, the χ^2 per degree of freedom of the track fit must be less than 4. The p_T measurement of a muon is based exclusively on the tracking system, and very high p_T tracks can have a large uncertainty because the track curvature is so small. Mismeasured high p_T muons can lead to large amounts

of fake missing transverse energy, $\not\!\!E_T$, and large $\not\!\!E_T$ is an important signature for leptonically decaying WW events. This track constraint helps ensure an accurate measurement of muon p_T and minimizes the fake $\not\!\!E_T$ from muon mismeasurement.

A tight constraint on muon isolation is also required. The scalar sum of the p_T of all tracks in a $\Delta R = 0.5$ cone around the muon's central track, excluding the muon's track itself, must be less than 2.5 GeV. A hollow cone of $0.1 < \Delta R < 0.4$ is defined around the muon in the calorimeter, and the scalar sum of all E_T in that hollow cone must be less than 2.5 GeV. These constraints on extra tracking and calorimeter activity help suppress muons that arise from jet fragmentation.

Chapter 4

The WW Signal and Background Processes

4.1 The WW Signature

A $WW \to \ell^- \bar{\nu}_\ell \ell'^+ \nu_{\ell'}$ event produces two oppositely charge signed high p_T leptons, which can be of different flavor, and a large amount of missing transverse energy, $\not\!\!E_T$, an unbalance of detected energy in the plane transverse to the colliding beam. Since the z-component of either neutrino momentum cannot be reconstructed, the exact kinematics of the initially produced bosons cannot be determined. However, the WW system is produced with, on average, 13.8 GeV of transverse energy, with a distribution that peaks near $\sim$2 GeV, as shown in Figure 4.1. The quantity q_T is a measure of the p_T boost of the WW system calculated from the observables in the event:

$$q_T = |\vec{p}_{T,\ell} + \vec{p}_{T,\ell'} + \vec{\not\!\!E}_T|. \tag{4.1}$$

This is a useful quantity for discriminating WW signal events from various backgrounds since q_T is large for many background processes.

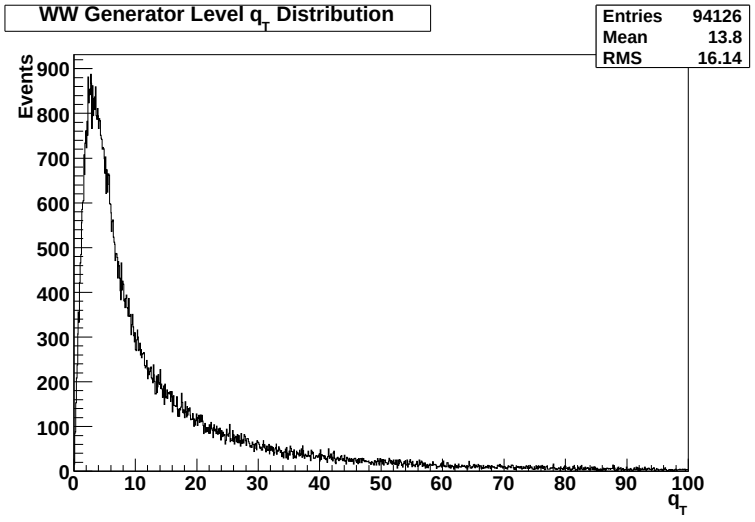

Figure 4.1 : The p_T boost of the WW system from PYTHIA [36] MC events without detector simulation.

4.2 Background Processes

Various background processes can mimic the fully leptonic WW decay signature, including Z, $t\bar{t}$, WZ, $W\gamma$, ZZ, W+jet and dijet QCD events. The theoretical cross sections of these backgrounds (except for QCD) are presented in Section 4.3, Table 4.1. All backgrounds except QCD are estimated based on standard DØ Monte Carlo (MC) events that are generated by PYTHIA [36, 37] and processed by a detailed detector simulation based on GEANT [38, 39, 40]. Details of the parameters used to represent the underlying event in PYTHIA are discussed in Appendix A. The W+jet MC has been shown to model the data well in previous DØ analysis, including the RunIIa $H \rightarrow WW$ analyses [41, 42, 43]. The QCD background is estimated from data, as described in Section 4.6. A data-based cross-check of all backgrounds involving a fake

lepton is provided in Appendix B.

Generally, the WW decay signature is faked due to mismeasuring objects in the event. A jet can be reconstructed as an electron or muon if it happens to hadronize such that most of it's energy goes a single pion, because the favored decay for the neutral pion is $\pi^0 \to \gamma\gamma$ and the favored decay of a charged pion is $\pi^+ \to \mu^+\nu_\mu$. A high p_T lepton that is mismeasured or falls outside the fiducial region of the detector will contribute to the $\not\!\!E_T$ measurement, and can lead to a fake $\not\!\!E_T$ signature. Finally, it is possible to have more than one proton-antiproton interaction per beam crossing, especially at high instantaneous luminosities, and these additional interactions can provide real or fake charged lepton and $\not\!\!E_T$ signatures.

While vetoing events with extra lepton or jet activity would be a useful strategy for removing certain backgrounds, such a veto would also inherently suppress higher instantaneous luminosity events due to the increased probability of multiple interactions. Therefore, such vetoes are explicitly avoided in this analysis.

A leptonic Z boson decay produces two high p_T leptons with opposite charge. If the p_T of one of these leptons is mismeasured, the fake $\not\!\!E_T$ will allow the $Z \to \ell\ell$ event to mimic the WW signature. High p_T muons are particularly susceptible to mismeasurement because the momentum is determined exclusively from track curvature. If $\not\!\!E_T$ is faked in this manner, q_T will still be small, but if the $\not\!\!E_T$ is from a single large p_T mismeasurement, then the angular separation between the $\not\!\!E_T$ and the mismeasured p_T vectors will be small. In this case, a cut on the angle between the $\not\!\!E_T$ and the

lepton will suppress the background. Large fake $\not\!\!E_T$ can also occur from a lepton that falls outside of the fiducial region of the detector, in which case an additional fake high p_T lepton is required in the event in order to mimic the WW signature. These events can be discriminated against because the fake lepton will match the charge of the fiducial Z product lepton half of the time, and the q_T of the event may be large, depending on the orientation of the fake lepton.

The top quark almost exclusively decays into a W boson and a b quark, so the $t\bar{t}$ signature can naturally involve two oppositely charged leptons and $\not\!\!E_T$ when both W bosons decay leptonically. However, the q_T variable for $t\bar{t}$ events is large because it is effectively boosted by the p_T of the jets.

Fully leptonic WZ decays will yield three high p_T charged leptons, of various charge sign and flavor, and large $\not\!\!E_T$. The q_T for these events tends to be large, in a similar way to $t\bar{t}$ events, because it is effectively boosted by the third high p_T lepton in the event.

A leptonic $W\gamma$ decay can fake a WW event in the ee or $e\mu$ channels when the W boson provides a charged lepton and $\not\!\!E_T$ and the photon creates a fake electron. An early conversion of the photon into electrons as it passes through the inner layers of the central tracking system could lead to a fake electron. A fake track or a real track from a charged particle close enough to the photon's calorimeter energy deposit could also create a fake electron. However, the electron likelihood variable is constructed to discriminate against such fake electrons by considering track quality and E_T/p_T

for the track compared to the calorimeter energy deposit. These events are further suppressed because the fake electron track will have a random charge sign.

Leptonic decays of Z boson pairs can produce events like $ZZ \to \ell^+\ell^-\nu_{\ell'}\bar{\nu}_{\ell'}$, which can directly mimic the ee and $\mu\mu$ decays of a W boson pair. In this case, the pair of charged leptons tend to have an invariant mass near the Z peak and tend to have $\Delta\phi_{\ell\ell} \sim \pi$, which allows for some discrimination with respect to a WW signal. The four charged lepton decay $ZZ \to e^+e^-\mu^+\mu^-$ can mimic the WW decay signature in the $e\mu$ channel, if one of the four charged leptons is lost or a mismeasured muon contributes to $\not\!\!E_T$. However, this ZZ decay mode has a very low branching ratio, since $BR(Z \to \ell^+\ell^-) \sim 3.4\%$.

The background from leptonic decays of W bosons that are produced with extra jet activity can be very difficult to discriminate from true WW events, if the jet fakes a high quality lepton. The cross-section of $W \to \ell\nu+X$ is over 200 times larger than the inclusive cross section for WW production (see Table 4.1), and $\sim 25\%$ of those events include one or more jets, without considering contributions from multiple interactions. About half of these events are immediately suppressed by requiring opposite charge sign between the candidate leptons. For the rest of these events, a few distinguishing characteristics allow for strong discrimination against jets that fake leptons. A fake lepton from a jet is usually not isolated from other particles in the detector, so extra tracks or calorimeter energy found nearby the candidate lepton is characteristic of a jet faking the object. For electrons, the transverse shower shape of the energy

deposit in the electromagnetic calorimeter tends to be wider when neutral pions are faking an electron signature. Additionally, the transverse energy as measured in the calorimeter may not match the transverse momentum of the track, leading to an E_T/p_T ratio far from 1. These quantities are taken into account when calculating the electron likelihood (see Section 3.3), so a tight cut on likelihood can suppress electrons faked by jets. Fake muons from jets can be suppressed through direct cuts on extra tracks and calorimeter energy near the muon. Jets may also fake muons if the jet produces particles that escape the calorimeter and hit the innermost layer of the muon system. These jet remnants usually will not pass through the muon system toroid, so requiring hits on either side of the muon toroidal magnet suppresses these fakes from calorimeter punch through.

Strong interactions between partons will directly lead to multiple jet production, which are labeled the "QCD" background in this analysis. The $\not\!\!E_T$ signature of WW events can be reproduced by a poorly measured jet, while both charged leptons can be faked by jets. Once again, about half of this background is immediately suppressed by requiring oppositely signed lepton candidates. The rest of the discrimination against this background comes from suppressing lepton candidates that are likely faked by jets, as discussed above. The p_T spectrum of jets produced by QCD interactions falls quickly with increasing p_T, so by requiring two high p_T jets and using tight lepton identification, the QCD background can be heavily suppressed.

4.3 Initial Data and Monte Carlo Samples

This analysis uses the "RunIIa" data sample of the DØ Collider Detector, including events starting from run number 151817 on April 19, 2002, and ending with run number 215670 on February 22, 2006. This data sample corresponds to approximately 1 fb^{-1} of integrated luminosity.

Events are triggered based on an OR of single electron triggers in the ee and $e\mu$ channels, and an OR of single muon triggers in the $\mu\mu$ channel. Generally, individual electron triggers require large E_T energy deposits in the EM layers of the calorimeter, with the possibility of requiring a high p_T central track. Energy thresholds and track match constraints vary for individual triggers depending on the instantaneous luminosity range they are tuned for. For example, the `E1_SHT_22` trigger in v13 of the trigger list requires one electromagnetic calorimeter trigger tower with $E_T > 11$ GeV at L1, an EM cluster with $E_T > 15$ GeV at L2, and an electron object with $E_T > 22$ GeV that satisfies a tight shower shape requirement at L3. The `E3_SHT_22` trigger in v13 of the trigger list has nearly the same set of conditions, except that it requires one EM calorimeter tower with $E_T > 9$ GeV and one with $E_T > 3$ GeV at L1, which can allow an electron that hits the boundary between two towers to trigger when it may not satisfy the L1 condition in `E1_SHT_22`.

Individual single muon triggers require muon system activity with the possible requirement of a high p_T central track, in a manner similar to the electron triggers. The `MUH1_TK12_TLM12` trigger in v13 of the trigger list requires a coincidence of scin-

tillator panel hits in the A and B/C layers of the muon system that is consistent with a muon and a central track with $p_T > 10$ GeV at L1, has no requirement at L2 and requires a central track with $p_T > 12$ GeV matched to a muon with local muon system $p_T > 12$ GeV at L3. Another muon trigger on the v13 list, `MUH1_LM15`, shares the same L1 and L2 requirements as `MUH1_TK12_TLM12`, but at L3 requires a muon with local muon system $p_T > 15$ GeV.

The final integrated luminosities for each final state are 1103.60 pb^{-1} for the ee channel, 1071.78 pb^{-1} for the $e\mu$ channel, and 1002.24 pb^{-1} for the $\mu\mu$ channel. The ee and $e\mu$ luminosities differ due to the data quality constraint on muons for required the $e\mu$ channel, which is not considered in the ee channel. Though they use the same data quality constraints, the $\mu\mu$ luminosity is lower than the $e\mu$ channel due to the difference in trigger live time and trigger prescales between the single electron trigger list and the single muon trigger list used. A detailed discussion of triggering and luminosity calculation is available in Appendix C.1.

Signal and background Monte Carlo samples are generated with Pythia [36], a LO event generator, and then processed by a detailed detector simulation based on Geant [38, 39, 40].

Monte Carlo events are scaled to represent the number of events expected for each process in the total integrated luminosity for each final state. This is accomplished by multiplying all events in a MC sample by the scaling factor

$$S_{MC} = \frac{\sigma_{MC} \times \mathcal{L}}{W_{MC}}, \tag{4.2}$$

where S_{MC} is the scaling factor, σ_{MC} is the cross section (times branching ratio) for the process in question, $\mathcal{L}$ is the integrated luminosity as appropriate for the final state, and W_{MC} is the total weight of all events for the MC sample. For $Z \to \ell\ell$ and $W \to \ell\nu + jet$ MC samples, W_{MC} depends on the reweighting scheme that corrects the generated gauge-boson p_T spectrum. For all other samples, W_{MC} is equal to the number of generated MC events. Refer to Table 4.1 for the cross section used to scale each MC sample. Each cross section in Table 4.1 is listed with its calculation order, where a leading-order (LO) calculation includes Feynman diagrams with one pair of particle vertices, next-to-leading-order (NLO) includes one more pair of vertices, and next-to-NLO (NNLO) includes yet another pair of vertices. For an electroweak process, LO terms are proportional to the square of the fine structure constant, $\alpha^2 \sim 1/137^2$, since one factor of α is introduced at each vertex. Electroweak NLO diagrams are proportional to α^4, and NNLO diagrams are proportional to α^6.

Process	σ (pb)	% Error	Order	Ref.
WW (inclusive)	12.0	—	NLO	[44]
$Z/\gamma* \to \ell\ell$ ($15 < m_Z < 60$ GeV)	465.0	$+1.99, -4.68$	NNLO*	[45, 44]
$Z/\gamma* \to \ell\ell$ ($60 < m_Z < 130$ GeV)	256.6	$+1.99, -4.68$	NNLO*	[45, 44]
$Z/\gamma* \to \ell\ell$ ($130 < m_Z < 250$ GeV)	2.08	$+1.99, -4.68$	NNLO*	[45, 44]
$t\bar{t}$	7.81	± 6.90	LO	[46]
WZ (inclusive)	3.68	± 6.79	NLO	[44]
$W\gamma \to \ell\nu\gamma$ (ISR & Trilinear)	1.85	± 8.41	NLO†	[47]
ZZ (inclusive)	1.42	± 5.63	NLO	[44]
$W \to \ell\nu$(+jet)	2582.7	$+3.66, -3.25$	NNLO	[44]

Table 4.1 : Cross sections used to scale various Monte Carlo samples, in pb, the percentage error used to calculate systematic uncertainties, and the order of the theoretical calculation. Citations to references for these cross section values are given in the right-most column.

4.4 Preselection

This analysis requires high quality charged lepton candidates, in order to suppress backgrounds from one or more fake leptons in an event. Electrons in this analysis must satisfy these criteria, as defined in Section 3.3:

- EM fraction > 0.9, where EM fraction is E_{EM}/E_{tot} within a $\Delta R < 0.4$ cone in the calorimeter
- Isolation < 0.2, where isolation is $(E_{tot} - E_{core})/E_{core}$, where E_{tot} is the total energy in a $\Delta R < 0.4$ cone in the calorimeter and E_{core} is the energy in a $\Delta R < 0.2$ cone in the electromagnetic calorimeter
- Matched to central track
- Electron likelihood > 0.85, using the electron likelihood defined in Section 3.3.2
- $|\eta_{CAL}| < 1.1$ (CC) or $1.5 < |\eta_{CAL}| < 3.0$ (EC), to remove the gap in full EM calorimeter coverage between the CC and EC

Muons must satisfy these criteria, as discussed in detail in Section 3.5:

- Medium ID (At least one scintillator and two wire hits in A and BC layers of Muon System, except in the region $5\pi/4 < \phi < 7\pi/4$ with $|\eta_{MUON}| < 1.6$ where A *or* BC layer scintillator and wire activity will suffice)

---

* The $Z/\gamma* \to \ell\ell$ cross sections are based on finding a scaling factor to make [44] match [45] in the 60-130 GeV mass window, then applying the same scaling factor to [44] in the other mass windows.

† The $W\gamma$ cross section listed is LO times a k-factor of 1.34, which on the average corrects to NLO. Also, it assumes the kinematic cuts $E_{T,\gamma} > 12$ GeV and $\Delta R_{\gamma\ell} > 0.4$.

- Matched central track has distance of closest approach (DCA) < 0.02 cm if track has SMT hits, DCA < 0.2 cm if track is CFT only (DCA is the smallest distance between the track and a line parallel to the z axis that passes through the primary vertex)
- Matched central track has $\chi^2/dof < 4.0$
- ($\Sigma^{tracks}|p_T|$ in a $\Delta R < 0.5$ cone around the muon) < 2.5 GeV (scalar sum of track p_T in a cone around the muon)
- ($\Sigma^{cells}|E_T|$ in a $0.1 < \Delta R < 0.4$ hollow cone around the muon) < 2.5 GeV (scalar sum of calorimeter E_T in a hollow cone around the muon)

where $\Delta R = \sqrt{\Delta\eta^2 + \Delta\phi^2}$. Across all three channels, events must satisfy these requirements in order to pass preselection:

- Two oppositely charged lepton candidates (ee, $e\mu$ or $\mu\mu$)
- $p_{T,lead} > 25.0$ GeV, where the leading lepton has the highest p_T of all charged leptons in the event
- $p_{T,trail} > 15.0$ GeV, where the trailing lepton has second highest p_T of all charged leptons in the event
- $\Delta R_{\ell\ell} > 0.5$ (except in ee channel, where $\Delta R_{ee} > 0.8$ in order to completely separate the electron isolation cones from each other)
- Oppositely charged leptons

- At least one charged lepton must be matched to and fire an appropriate trigger (see Sec. C.1)
- Track $\Delta Z_{\ell\ell} < 2.0$ cm and ΔZ between the leading lepton track and the primary vertex < 2.0 cm

The primary vertex is the tracking vertex with the highest scalar sum of track p_T associated with it.

4.5 Monte Carlo Corrections

Additional momentum resolution smearing is applied to all MC muons based on DØ common analysis tools in order to better match the muon momentum resolution in data. Details of the these tools are available in Section C.2. Additionally, LO Pythia $Z \to \ell\ell$ MC samples are reweighted to match the NLO Resbos [48] Z p_T spectrum, as a function of both the Z boson's p_T and invariant mass [49]. Standard DØ tools are used to adjust the instantaneous luminosity profile and the primary vertex z distribution in MC to better match the data (see Section C.2) for more detail). Each MC event is overlayed with a "minimum bias" data event, which was triggered based on a coincidence of activity between the north and south luminosity monitors that estimates a primary vertex z position in the central area of the detector. The instantaneous luminosity of a MC event is based on the instantaneous luminosity of its minimum bias overlay, which may not share the same instantaneous luminosity profile as the signal data sample.

Missing E_T is an important quantity in each channel, in order to discriminate WW candidates from Z backgrounds, in particular. The $\not\!\!E_T$ is calculated using the primary vertex position and lists of EM objects, jets and muons in each event. To calculate $\not\!\!E_T$, this analysis uses EM objects with $p_T > 5$, EM fraction < 0.9 and isolation < 0.15, Jet Energy Scale (JES) corrected "JCCB" (cone size 0.5) jets with $p_T > 15$ that do not overlap with any EM objects, and all muons that satisfy medium ID requirements and have a track match. The $\not\!\!E_T$ represents the vector necessary to correct the overall p_T imbalance of an event, and is calculated as the negative vector sum of the p_T of all of the objects listed above, using the primary vertex position to assign a four-momentum to calorimeter energy clusters that are not associated with a track.

All $Z \to \ell\ell$ and WW samples are corrected to match the lepton charge mis-ID rate seen in data, as measured by comparing Z candidates in data to $Z \to ee$ or $Z \to \mu\mu$ MC. The electron charge mis-ID rate is measured via a tag and probe method, using ee events that satisfy the preselection criteria in Sec. 4.4. The leading and trailing electrons are considered candidates for being the tag or probe in an event, and both combinations of tag and probe are considered. In addition to the normal preselection requirements, the event must have $\not\!\!E_T < 20$ GeV, and $80 < M_{e,e} < 100$. In such events, a good tag electron must be in the Central Calorimeter, have significance of curvature $|(1/p_T)/\sigma_{1/p_T}| > 15$, and have $0.8 < E_{T,CAL}/p_{T,TRK} < 1.2$. Note that in MC σ_{1/p_T} is poorly modeled, so is scaled by a factor of $\sqrt{2}$ in order to better match

data. In these events, if the tagged lepton's charge matches the probe lepton's charge, the probe lepton is assumed to have the incorrect charge assigned. Probe leptons in the Central and Endcap Calorimeters are considered separately.

The results of these measurements are given in Table 4.2, and the measured charge mis-ID rate in data and MC as a function of p_T is shown in Fig. 4.2. The scaling factors used to scale same-signed MC samples to match data are given in Tab. 4.3.

Lepton	Data CMID Rate	MC CMID Rate
CC Electrons	0.2995 ± 0.0485%	0.0756 ± 0.0148%
EC Electrons	4.7117 ± 0.2280%	2.1891 ± 0.0927%
Muons	0.2995 ± 0.0403%	0.0736 ± 0.0074%

Table 4.2 : Lepton charge mis-ID rates in Data and MC. CC electrons must have $|\eta_{CAL}| < 1.1$, while EC electrons must have $1.5 < |\eta_{CAL}| < 3.0$.

Channel	MC Scaling Factor
ee (CC-CC events)	3.95161 ± 0.71096
ee (CC-EC events)	2.20350 ± 0.13736
$e\mu$ (CC e events)	4.00634 ± 0.61363
$e\mu$ (EC e events)	2.20544 ± 0.13651
$\mu\mu$	4.06259 ± 0.48337

Table 4.3 : The MC Scaling Factor is the number used to scale the same-signed MC samples to match the data.

The muon charge mis-ID rate is measured in a very similar way, beginning with preselected events as described in Section 5.4 and additionally requiring that the tag muon's significance of curvature is greater than 15, the muon corrected $\not\!\!E_T < 20$

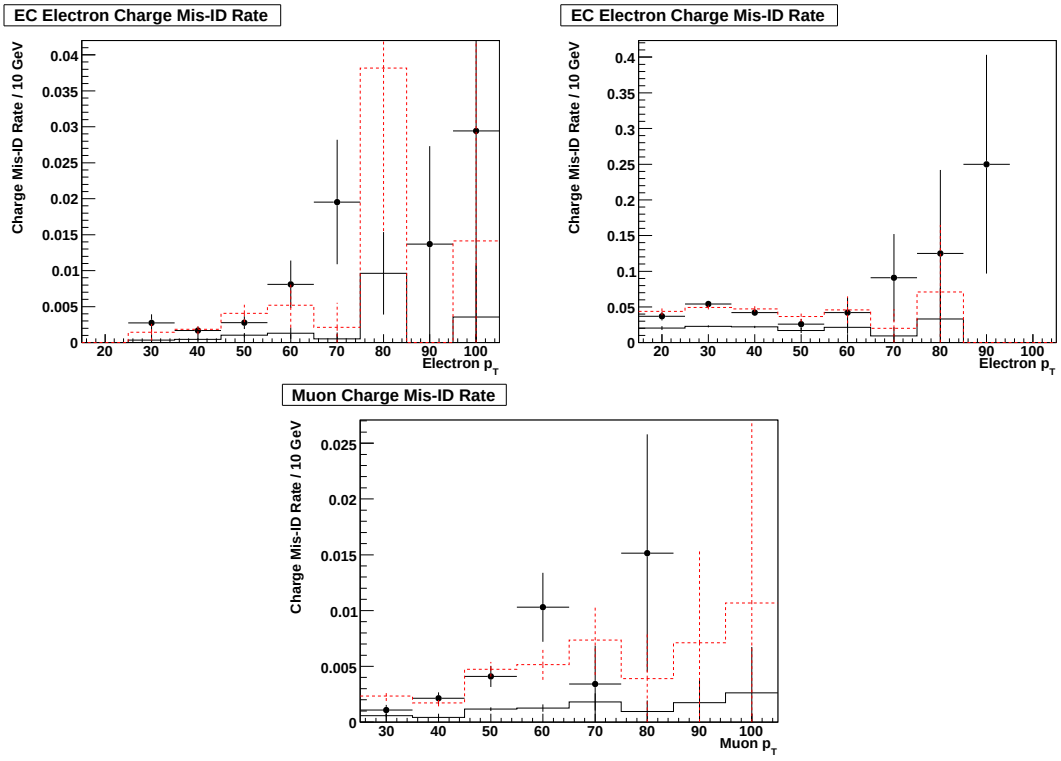

Figure 4.2 : Lepton charge mis-ID rate as a function of lepton p_T. Dots represent the data rate, while the solid black and dotted red histograms represent the $Z \rightarrow ee/\mu\mu$ MC before and after the correction factor is applied, respectively.

GeV, and $70 < M_{\mu\mu} < 110$. A scaling factor for the $e\mu$ channel is derived from the individual electron and muon charge mis-ID rates in data and MC.

In all channels, opposite-signed MC samples are reduced by the same number of events that the same-signed samples are increased by due to these corrections, in order to preserve the absolute luminosity normalization. This translates into a 1-2% reduction in the number of same-signed $Z \to \ell\ell$ and WW MC events, depending on the specific analysis channel.

4.6 QCD Background Estimation

A QCD background estimate for each channel is created by first selecting a sample of events with two "bad" leptons from the data. An electron is considered "bad" if Electron Likelihood < 0.2, and a muon is considered bad if EtHalo > 4.0 (where EtHalo is the sum of energy in calorimeter cells where $0.1 < \Delta R_{\mu,cell} < 0.4$). This sample provides the kinematic distributions used to estimate the behavior of the QCD background, but must be scaled to produce the proper absolute number of expected events. The QCD contribution, after all other preselection cuts as described in Sec. 4.4, is expected to be randomly distributed between same-signed and opposite-signed lepton events. This analysis accepts only opposite-signed lepton events as signal candidates, so the same-signed data sample for each channel is used to normalize the total number of QCD events for that channel. The invariant mass distributions of the same-signed QCD sample for each channel are shown in the lower-left plots of Figs. 4.3-4.7.

The QCD sample is normalized by a fit to the invariant mass spectrum of the same-signed lepton events that pass all other preselection criteria, as described in Section 5. This fit finds a scaling factor for the QCD sample such that the scaled QCD sample plus all of the fully corrected MC samples match the data with the minimal χ^2. This scaling factor is found once for each analysis channel, after preselection cuts have been applied, and then remains fixed for the rest of the selection process.

The fit is based on a χ^2 minimization to find the best fit value and an uncertainty on the fit parameter. The statistical uncertainty from the data and the statistical, efficiency, and charge mis-ID uncertainties from the MC samples all factor into the χ^2 value used in the fit. The QCD scaling factor is restricted to being a positive number during the fitting process, while all other quantities are fixed. The result of the fit to data across the invariant mass distributions of each channel are shown in the right-side plots of Figs. 4.3-4.7. The scaling factors are shown in Tab. 4.4.

Channel	QCD Scaling Factor	χ^2/dof
ee (CC-CC events)	(2.35 $\pm$ 0.82) $\times 10^{-4}$	25.6 / 9
ee (CC-EC events)	($\sim$0.0 $\pm$ 1.12) $\times 10^{-4}$	3.7 / 9
$e\mu$ (CC e events)	(3.91 $\pm$ 5.14) $\times 10^{-4}$	2.3 / 9
$e\mu$ (EC e events)	(1.38 $\pm$ 1.00) $\times 10^{-3}$	1.2 / 4
$\mu\mu$	($\sim$0.0 $\pm$ 1.25) $\times 10^{-2}$	24.1 / 9

Table 4.4 : The QCD Scaling Factor is the number used to scale the raw "bad lepton" sample in order to match the estimated number of QCD events for each channel. The χ^2/dof of the fit used to determine the scale factor appears in the right column.

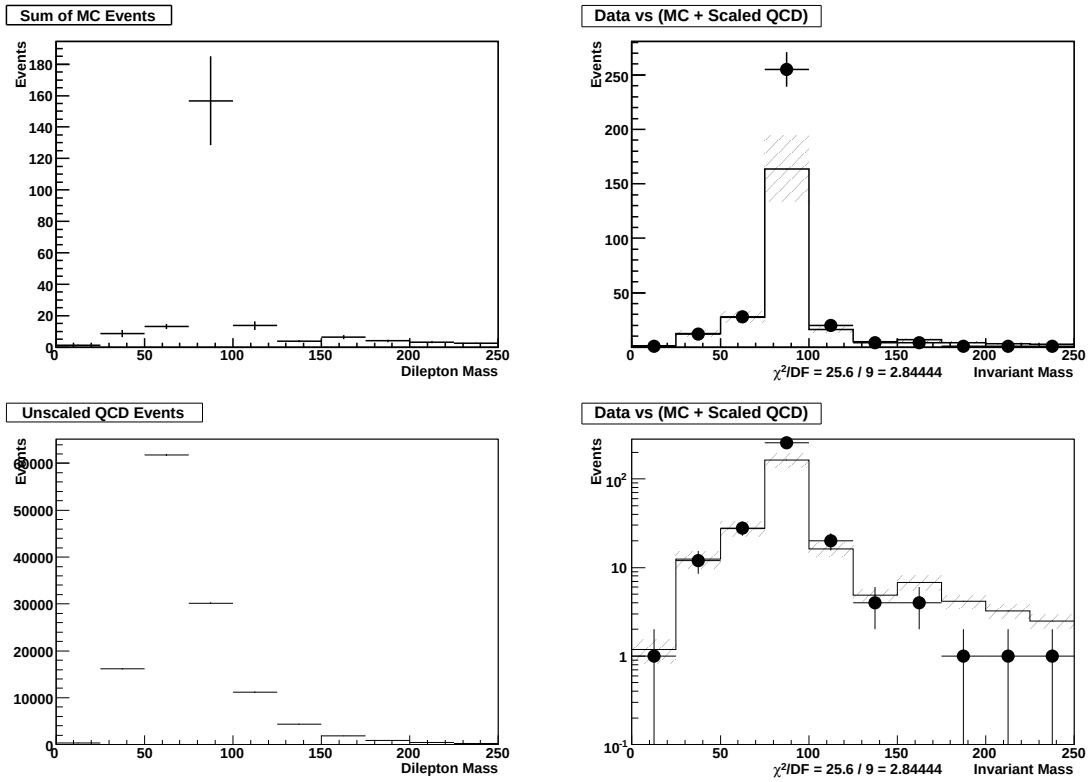

Figure 4.3 : QCD scaling factor fit to invariant mass for *ee* channel CC-CC events. The upper left plot shows the sum of all same-signed signal and background MC events after preselection. The lower left plot shows the same-signed preselected QCD data sample, prior to applying a scaling factor. The upper and lower right plots show the distribution of data (points with error bars), to the sum of all MC plus the scaled QCD sample (histogram with error band).

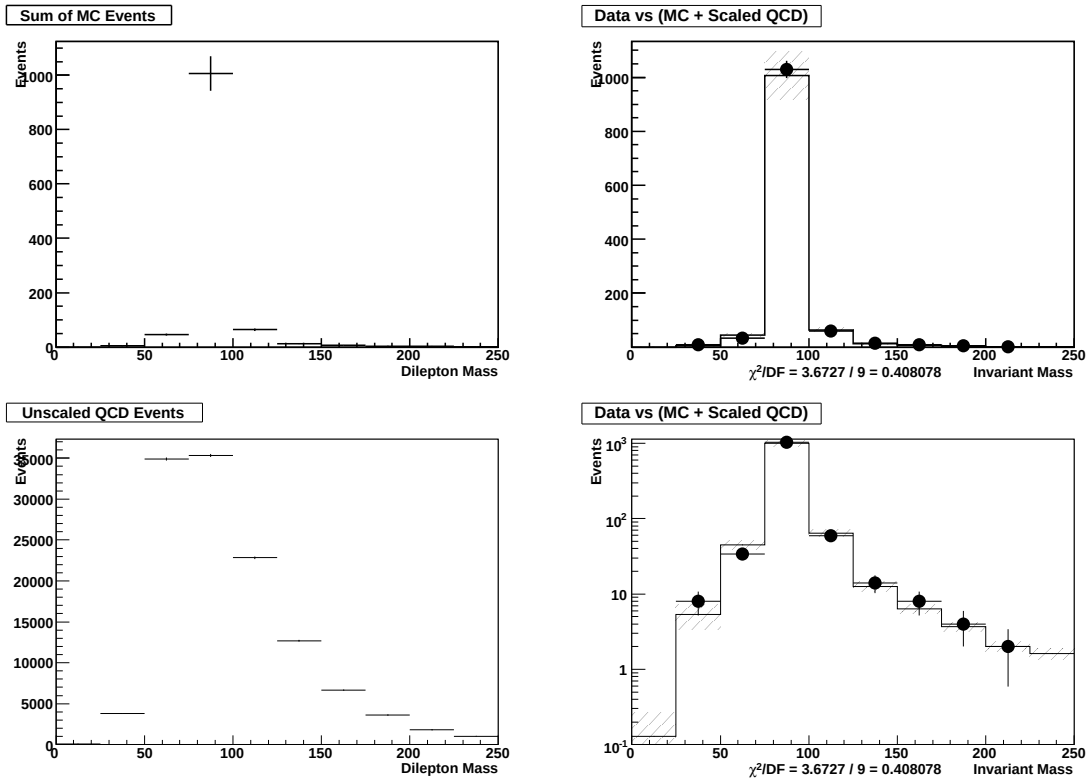

Figure 4.4 : QCD scaling factor fit to invariant mass for *ee* channel CC-EC events. The upper left plot shows the sum of all same-signed signal and background MC events after preselection. The lower left plot shows the same-signed preselected QCD data sample, prior to applying a scaling factor. The upper and lower right plots show the distribution of data (points with error bars), to the sum of all MC plus the scaled QCD sample (histogram with error band).

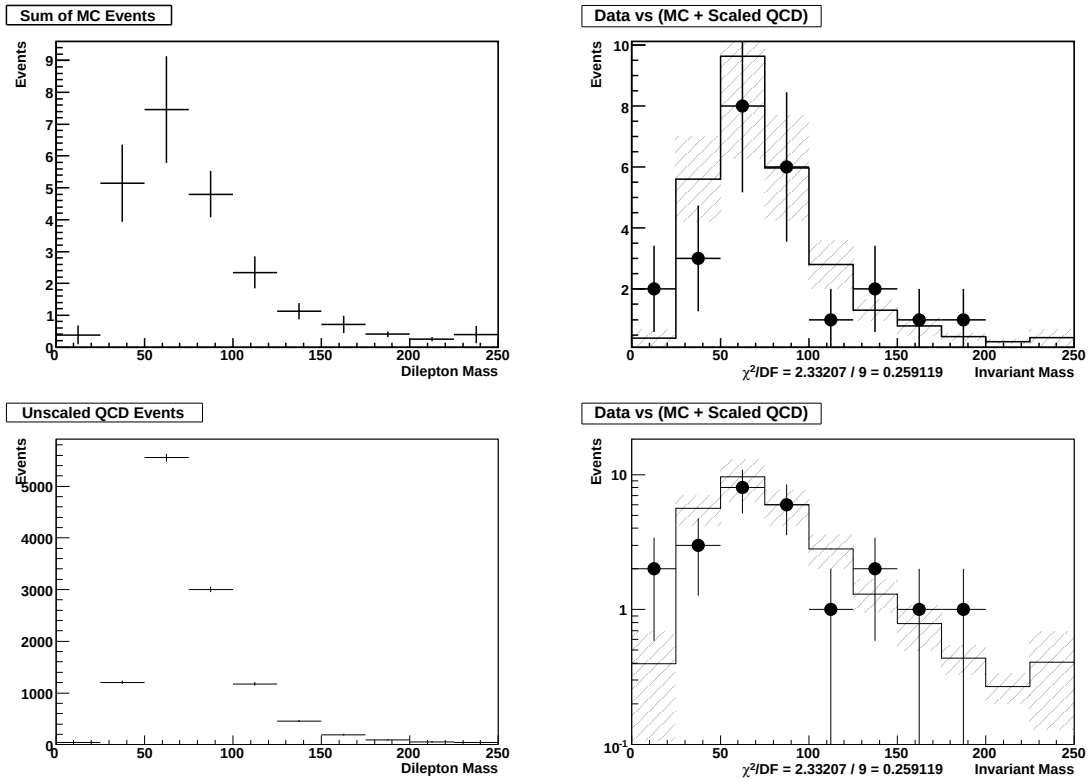

Figure 4.5 : QCD scaling factor fit to invariant mass for $e\mu$ channel CC-Electron events. The upper left plot shows the sum of all same-signed signal and background MC events after preselection. The lower left plot shows the same-signed preselected QCD data sample, prior to applying a scaling factor. The upper and lower right plots show the distribution of data (points with error bars), to the sum of all MC plus the scaled QCD sample (histogram with error band).

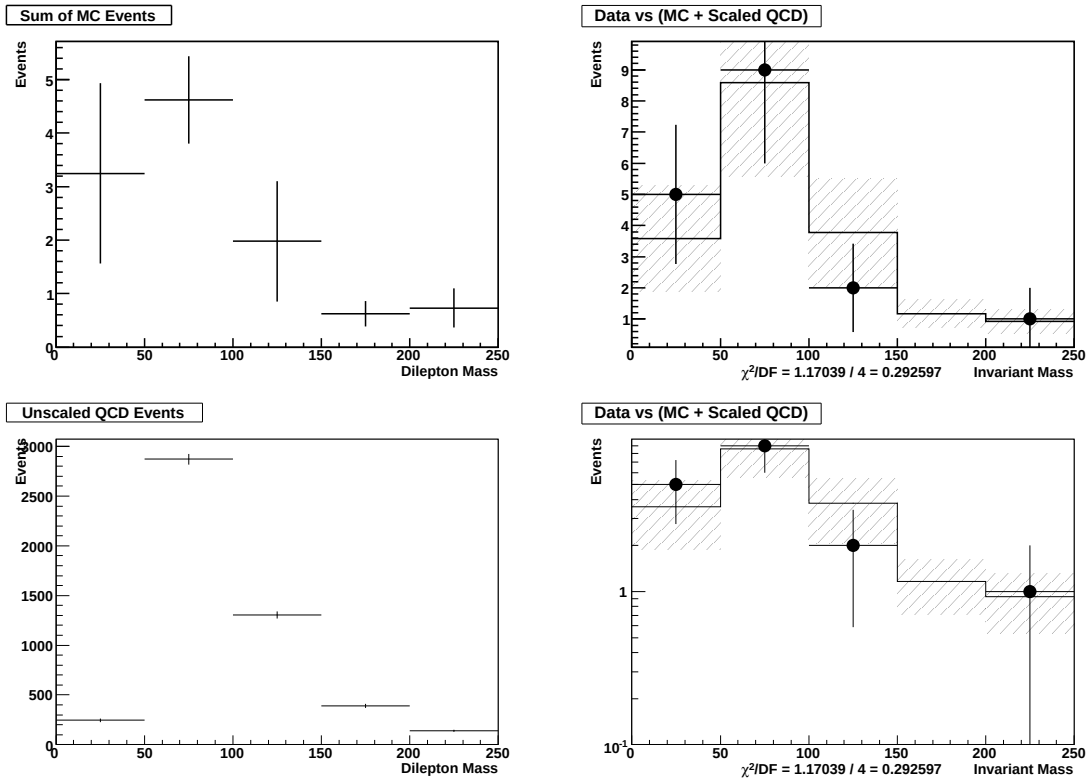

Figure 4.6 : QCD scaling factor fit to invariant mass for $e\mu$ channel EC-Electron events. The upper left plot shows the sum of all same-signed signal and background MC events after preselection. The lower left plot shows the same-signed preselected QCD data sample, prior to applying a scaling factor. The upper and lower right plots show the distribution of data (points with error bars), to the sum of all MC plus the scaled QCD sample (histogram with error band).

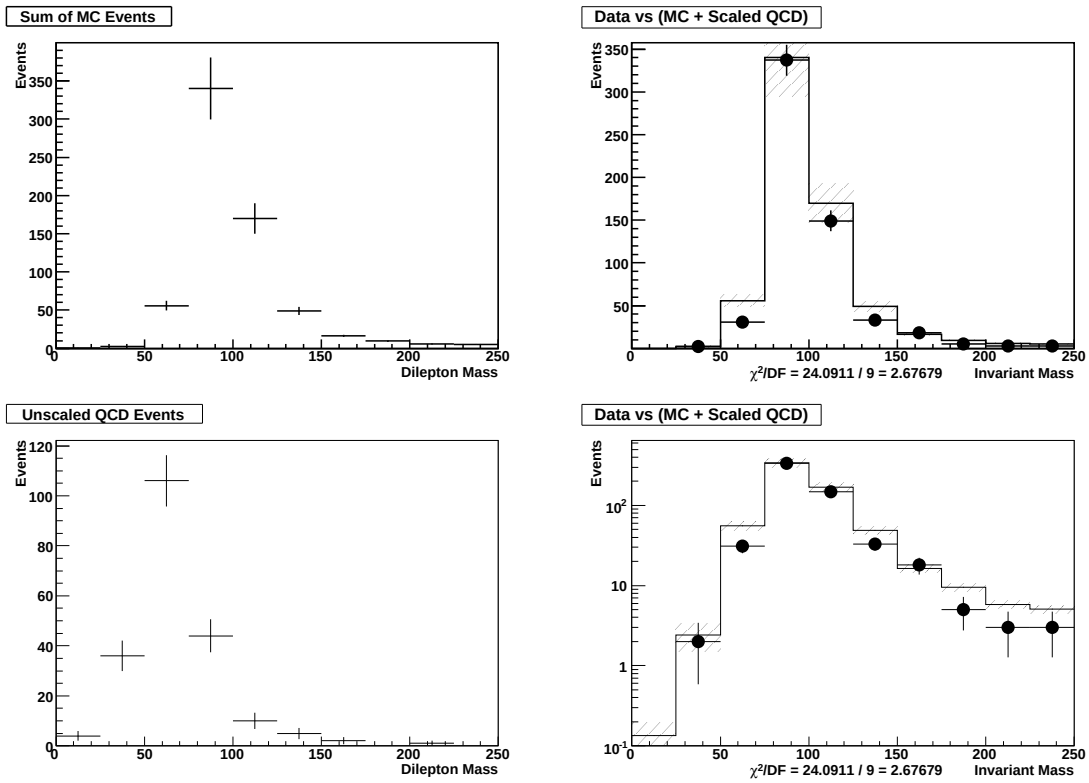

Figure 4.7 : QCD scaling factor fit to invariant mass for $\mu\mu$ channel events. The upper left plot shows the sum of all same-signed signal and background MC events after preselection. The lower left plot shows the same-signed preselected QCD data sample, prior to applying a scaling factor. The upper and lower right plots show the distribution of data (points with error bars), to the sum of all MC plus the scaled QCD sample (histogram with error band).

Chapter 5

Signal Selection Cuts

5.1 Significance Metric Derivation

This analysis intends to make the most accurate measurement of the WW cross section possible with 1 fb^{-1} of integrated luminosity. To accomplish this goal, the fractional uncertainty on the cross section, δ_σ/σ, must have the minimal value possible (or, alternatively, the value of σ/δ_σ should be maximized). The cross section is determined by this equation:

$$\mathcal{L}A\epsilon_P\epsilon_S\sigma = N - B \tag{5.1}$$

where $\mathcal{L}$ is the luminosity, A is the signal acceptance, ϵ_P is the signal preselection efficiency, ϵ_S is the signal selection cut efficiency, N is the number of events measured by the experiment, and B is the expected number of background events.

If $\mathcal{L}$, A, and ϵ_P are considered to be constant while choosing a selection cut, then:

$$\delta\sigma^2 = \frac{1}{(\mathcal{L}A\epsilon_P\epsilon_S)^2}\Big(\delta_N^2 + \delta_B^2 + \Big[\frac{-\delta_{\epsilon_S}(N-B)}{\epsilon_S}\Big]^2\Big) \tag{5.2}$$

Considering that N is determined by a counting experiment such that $\delta_N = \sqrt{N}$, the

quantity that should be maximized is:

$$\begin{aligned} \frac{\sigma}{\delta\sigma} &= \frac{N-B}{\sqrt{N+\delta_B^2+(N-B)^2\delta_{\epsilon_S}^2/\epsilon_S^2}} \\ &= \frac{S}{\sqrt{S+B+\delta_B^2+S^2\delta_{\epsilon_S}^2/\epsilon_S^2}} \end{aligned} \tag{5.3}$$

where S is the number of signal events, such that $N = S+B$. Here, δ_B represents the uncertainty on the background estimate, and $S\delta_{\epsilon_S}/\epsilon_S$ represents the uncertainty on the signal estimate introduced due to the uncertainty in the signal selection efficiency. A typical $\delta_{\epsilon_S}^2/\epsilon_S^2$ for this analysis, as computed from the WW MC sample, is less than 5%.

In the limit that $S^2\delta_{\epsilon_S}^2/\epsilon_S^2$ is small compared to N, the quantity that should be maximized for a set of signal selection cuts is:

$$\frac{\sigma}{\delta\sigma} = \frac{S}{\sqrt{S+B+\delta_B^2}} \tag{5.4}$$

Selection cuts for all channels are based on optimizing this quantity using the signal and background estimates discussed in Chapter 4. The cut variables used in each channel are those capable of providing the highest $\sigma/\delta\sigma$ when applied in succession. A multidimensional grid search is performed across these variables to seek out the specific cut values in these variables that provides the maximum $\sigma/\delta\sigma$.

5.2 Event Selection in the *ee* Channel

The *ee* channel is based on the Common Sample Group's "2EMhighpt" data skim, which requires two reconstructed electron objects each with $p_T > 12.0$ GeV in each

event. In this context, the "leading lepton" refers to the highest p_T lepton in the event, while the "trailing lepton" refers to the second highest p_T lepton in the event. Selected electrons must satisfy these conditions:

- EM Fraction > 0.9, Isolation < 0.2, electron matched to track
- Electron Likelihood > 0.85
- $p_{T,lead} > 25.0$ GeV, $p_{T,trail} > 15.0$
- $|\eta_{CAL}| < 1.1$ or $1.5 < |\eta_{CAL}| < 3.0$, at least one electron in Central Calorimeter
- $\Delta R_{ee} > 0.8$
- Track $\Delta Z_{ee} < 2.0$ cm and ΔZ between the lead track and the primary vertex < 2.0 cm
- Oppositely charged electrons
- Either electron is matched to and fires a single electron trigger (see Table C.1)

An electron is considered to fire a trigger if it is spatially matched to all L1, L2 and L3 components of a specific trigger and that trigger fired during the event. This distinction is important to prevent event triggers from electrons not considered part of the WW decay, which would make the event trigger probability in data higher than that being assigned to the MC samples. The single electron triggers used in this analysis are listed in Table C.1. The total integrated luminosity represented by

this data set is 1104 ± 67 pb^{-1}. Details of the luminosity calculation can be found in Appendix C.1.

If more than one track is associated with an electron object, then the track with the best spatial track match to the EM cluster is used. The p_T of the electron is recalculated using the energy in the EM cluster and the η of the track. This ensures that the p_T represents the electron as defined using the best spatial track match.

After preselection, the invariant mass, shown in Figure 5.1, and the lepton ϕ and η distributions, shown in Figure 5.2, appear to be modeled well. Individual plots of the signal and background distributions of invariant mass and q_T after preselection are available in Appendix D. The kinematic distributions after preselection in data and MC are shown in Figure 5.3, and show good agreement between data and MC. A useful kinematic quantity for studying the WW system is the minimal transverse mass, shown in Figure 5.3. Two transverse masses can be calculated for the fully leptonic WW final state by associating the $\not\!\!E_T$ vector with either of the two charged leptons:

$$m_T = \sqrt{2\left|\not\!\!E_T\right|\left|p_T\right|\left(1-\cos\phi\right)} \tag{5.5}$$

where p_T is the transverse momentum of either charged lepton and ϕ is the azimuthal angular separation between the $\not\!\!E_T$ and that charged lepton. The lower of the two m_T quantities calculated in this manner is considered the minimum transverse mass. The minimum transverse mass distribution of WW events tends to extend to higher values than many backgrounds, especially $Z \to \ell\ell$ events.

The number of events after preselection and each sequential selection cut are given in Table 5.1. The statistical uncertainty of a MC sample is the square root of the sum of the squares of the individual event weights. The systematic uncertainty of a MC sample is similarly defined based on the individual event uncertainties from ID efficiency corrections (see Appendix C.2) and the trigger probability uncertainty [50, 51]. The charge mis-ID correction uncertainty is also part of the systematic uncertainty for the WW and $Z \to \ell\ell$ samples, and is the average difference between using a charge mid-ID correction factor that is 1σ up or down for the entire MC sample (see Section 4.5). The kinematic selection cuts are optimized such that the final combination of cuts yields the highest significance, as described in Section 5.1.

Missing transverse energy, $\not\!\!E_T$, is the first selection cut applied to the data. Since the WW system contains two high p_T neutrinos, it contains a significant amount of unbalanced transverse energy. Cutting on $\not\!\!E_T$ significantly reduces backgrounds that do not contain high energy neutrinos. Backgrounds that survive this cut either have real neutrinos, or have a source of fake $\not\!\!E_T$, such as charged leptons that are mis-measured or are not within the fiducial region of the DØ detector. The distribution of $\not\!\!E_T$ after preselection is shown in Figure 5.3.

In WW events, because neutrinos from the W decays are the source of $\not\!\!E_T$, the vector sum of the p_T of the two charged leptons and the $\not\!\!E_T$ (q_T) will be equal to the p_T boost of the WW system, which is on the order of a few GeV. Backgrounds with authentic $\not\!\!E_T$ that is unrelated to the candidate charged leptons, such as $Z \to \ell\ell$ plus

ee Channel Cut Flow							
	$Z \to ee$	$Z \to \tau\tau$	$t\bar{t}$	WZ	$W\gamma$	ZZ	W+jet
Preselection	59441.0 ± 195.9	180.2 ± 7.5	27.79 ± 0.47	31.00 ± 0.71	2.69 ± 0.66	6.246 ± 0.071	16.0 ± 3.0
Cut 1	20.9 ± 3.2	4.6 ± 1.4	20.05 ± 0.40	5.68 ± 0.29	0.92 ± 0.32	2.981 ± 0.051	6.8 ± 2.2
Cut 2	1.08 ± 0.58	0.55 ± 0.11	1.27 ± 0.11	1.91 ± 0.16	0.62 ± 0.27	2.151 ± 0.043	4.0 ± 1.3
Cut 3	0.60 ± 0.32	0.47 ± 0.11	1.24 ± 0.10	1.51 ± 0.15	0.62 ± 0.27	1.752 ± 0.039	3.9 ± 1.3

	QCD	Bkg. Total	$WW \to ee$	$WW \to \ell\tau$	Total Expected ($\pm$ lumi)	Data
Preselection	29.8 ± 27.0	59734.8 ± 198.4	34.1 ± 1.1	5.42 ± 0.42	59774.3 ± 198.5 (± 3644.4)	60879
Cut 1	0.17 ± 0.16	62.1 ± 4.2	16.48 ± 0.73	2.47 ± 0.28	81.0 ± 4.3 (± 4.9)	92
Cut 2	0.032 ± 0.032	11.6 ± 1.5	13.78 ± 0.67	1.96 ± 0.25	27.4 ± 1.6 (± 1.7)	27
Cut 3	0.028 ± 0.028	10.1 ± 1.4	13.28 ± 0.65	1.87 ± 0.24	25.2 ± 1.6 (± 1.5)	26

Table 5.1 : Data and MC events left after preselection and each selection cut in the ee channel. Errors include contributions from statistical, efficiency and charge mis-ID uncertainties. Cut 1 is $\not\!\!E_T >$ 40 GeV, Cut 2 is $q_T <$ 20 GeV, and Cut 3 is ($\not\!\!E_T >$ 50 GeV if $|M_Z - M_{ee}| <$ 7 GeV). The $WW \to \ell\tau$ channel represents $WW \to e\tau/\tau\tau \to ee$ events.

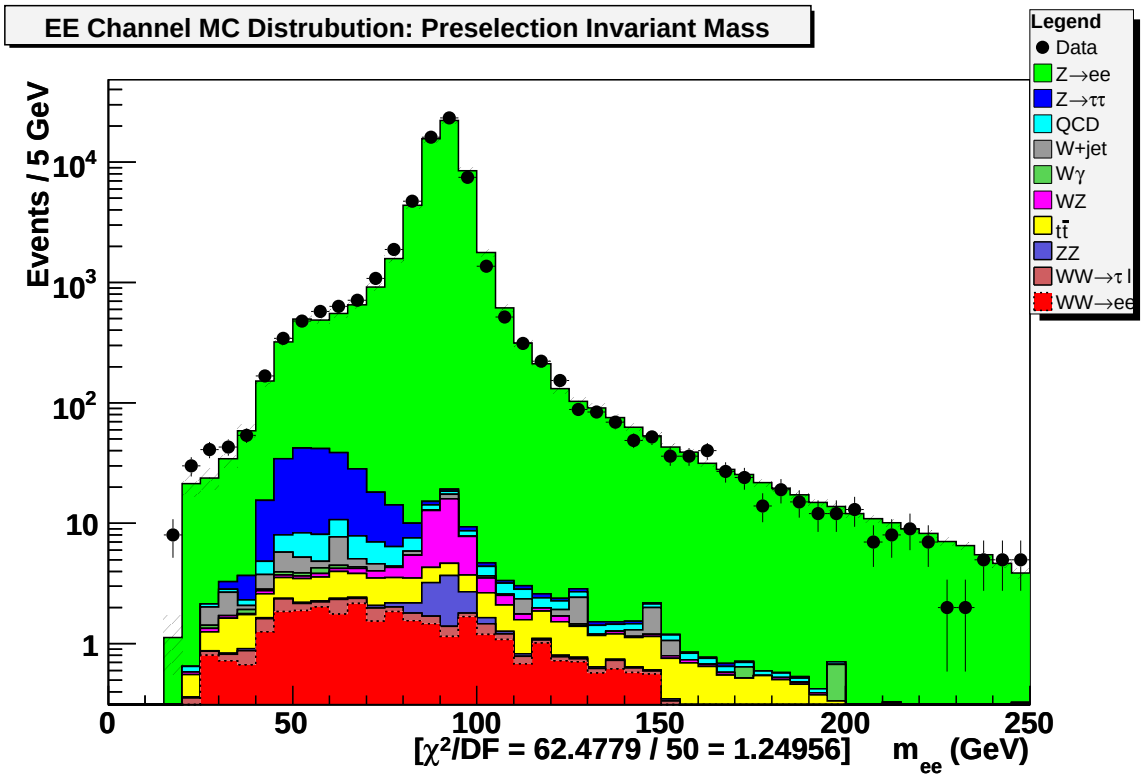

Figure 5.1 : Preselected event invariant mass distribution in the ee channel. For each bin, $\chi^2 = (N_{data} - N_{MC})^2/(N_{data} + \sigma^2_{MC})$; $\chi^2/DF = [\Sigma_{bins}\chi^2]/N_{bins}$.

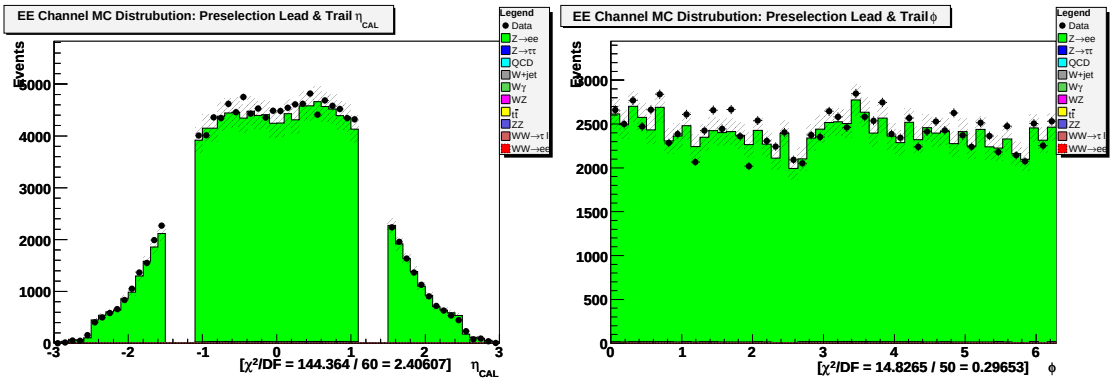

Figure 5.2 : Leading and trailing electron η_{CAL} (left) and ϕ (right) distributions after preselection in the ee Channel. For each bin, $\chi^2 = (N_{data} - N_{MC})^2/(N_{data} + \sigma^2_{MC})$; $\chi^2/DF = [\Sigma_{bins}\chi^2]/N_{bins}$.

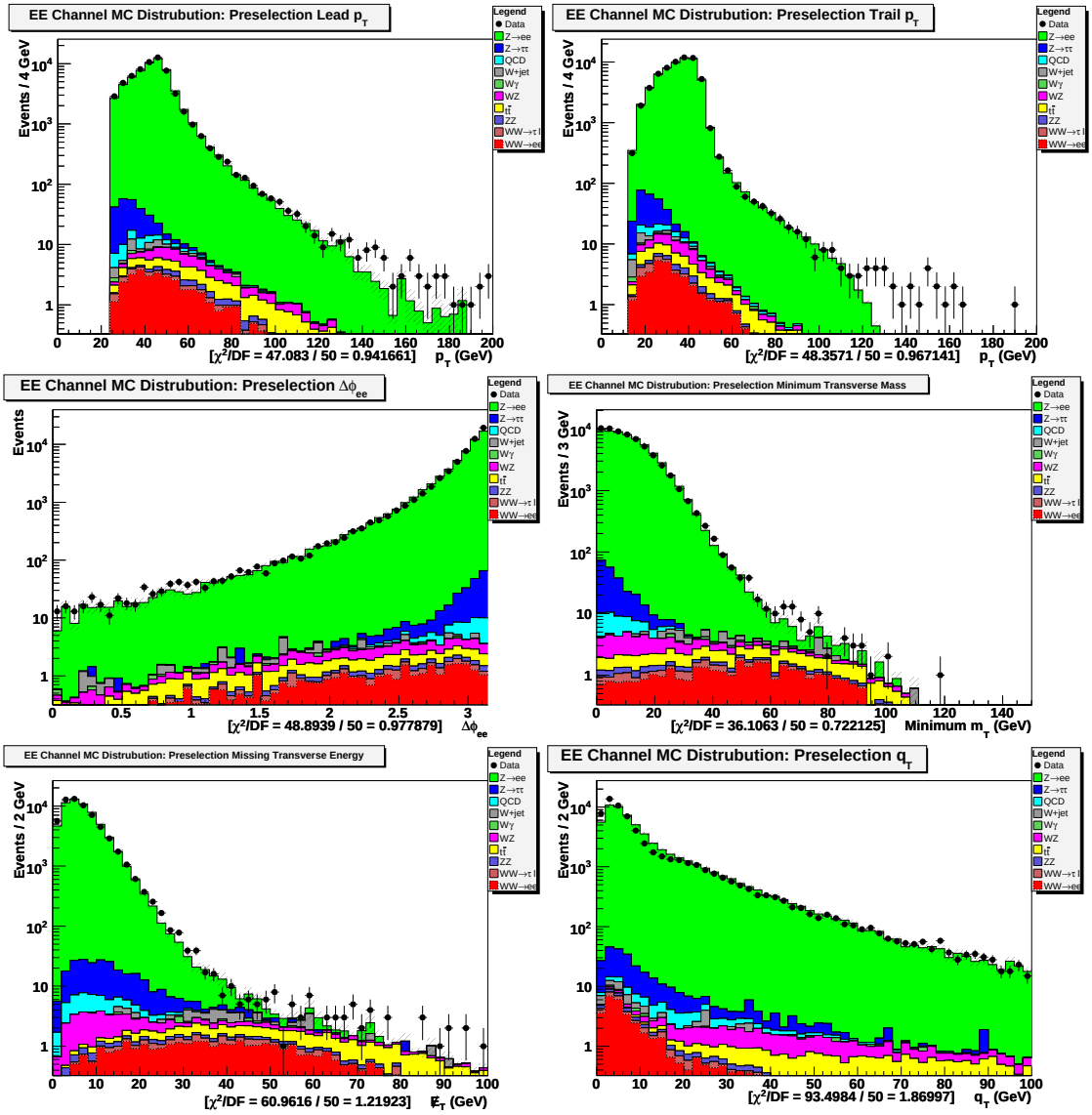

Figure 5.3 : Kinematic distributions after preselection in the ee channel. Clockwise, from top-left: leading e p_T, trailing e p_T, minimum transverse mass, q_T, $\not\!\!E_T$ and azimuthal separation ($\Delta\phi_{ee}$). For each bin, $\chi^2 = (N_{data} - N_{MC})^2/(N_{data} + \sigma^2_{MC})$; $\chi^2/DF = [\Sigma_{bins}\chi^2]/N_{bins}$.

a secondary interaction, are likely to have a high value of this quantity. However, background events with large fake $\not\!\!E_T$ from mis-measured charged leptons will tend to have a balanced vector sum, and may not be rejected. The distribution of q_T after the initial $\not\!\!E_T$ cut is shown in Figure 5.4. The invariant mass distribution after the initial $\not\!\!E_T$ cut is shown in Figure 5.5.

Finally, in order to further reduce background from $Z \rightarrow \ell\ell$ and ZZ events, a invariant mass window cut around the Z mass peak is used. The distribution of $|M_Z - m_{ee}|$ after the $\not\!\!E_T$ and q_T cuts is shown in Figure 5.4. The dominant background that remains is from W+jet events, which can readily mimic the kinematics of a WW event when the jet fakes an electron.

The optimization of signal selection, based on the significance metric defined in Section 5.1, led to the following cuts in the ee channel:

- $\not\!\!E_T >$ 40 GeV
- $q_T <$ 20 GeV
- $\not\!\!E_T >$ 50 GeV if $|M_Z - m_{ee}| <$ 7 GeV

After signal selection, a total of 25.2 ± 1.6 (stat & syst) ± 1.5 (lumi) events are expected, and 26 events are observed. The invariant mass and minimum transverse mass distributions after all selection cuts are shown in Figure 5.5 and Figure 5.6, respectively. Agreement between data and the signal plus background estimates is good after preselection and throughout the selection process for ee events.

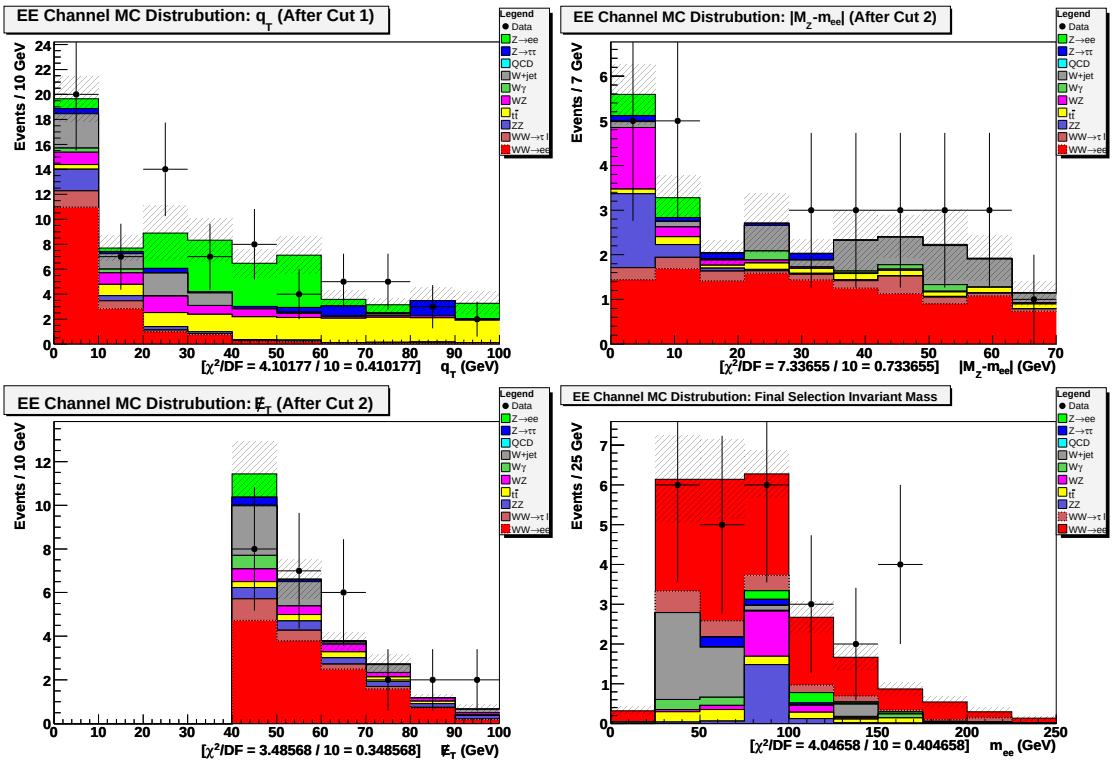

Figure 5.4 : Selection cut distributions in ee channel. Upper left plot shows q_T distribution after $\not\!\!E_T$ cut. Upper right and lower left plots show $|M_Z - m_{ee}|$ and $\not\!\!E_T$, respectively, after initial $\not\!\!E_T$ and q_T cuts. Lower right shows invariant mass distribution after all selection cuts. For each bin, $\chi^2 = (N_{data} - N_{MC})^2/(N_{data} + \sigma^2_{MC})$; $\chi^2/DF = [\Sigma_{bins}\chi^2]/N_{bins}$.

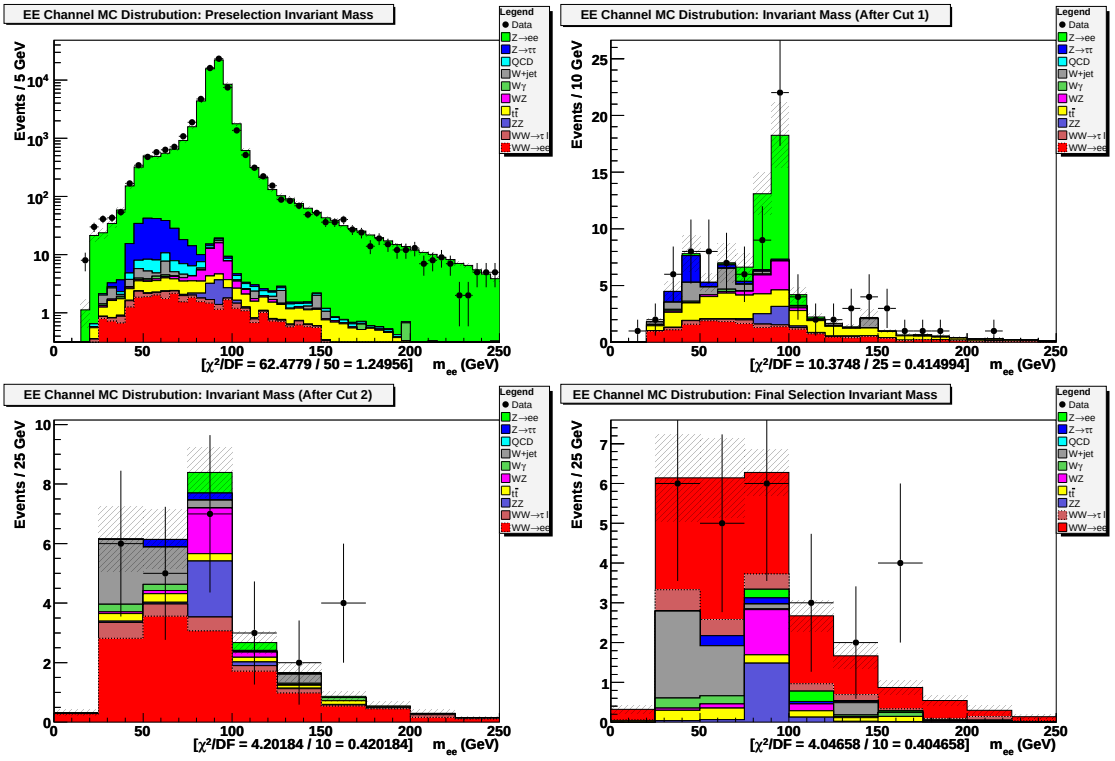

Figure 5.5 : Invariant mass distributions in ee channel as cuts are applied. Upper left plot shows m_{ee} distribution after preselection. Upper right shows m_{ee} after $\not\!\!E_T$ cut. Lower left shows m_{ee} after $\not\!\!E_T$ and q_T cuts. Lower right shows m_{ee} after all selection cuts. For each bin, $\chi^2 = (N_{data} - N_{MC})^2/(N_{data} + \sigma^2_{MC})$; $\chi^2/DF = [\Sigma_{bins}\chi^2]/N_{bins}$.

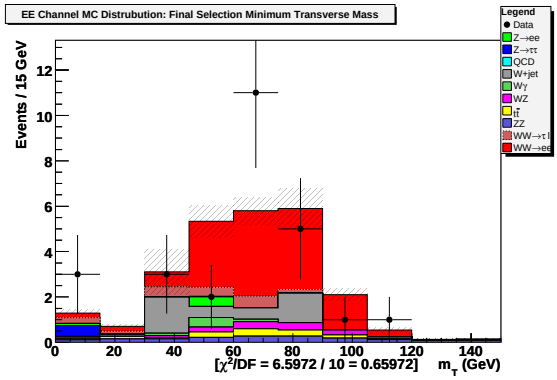

Figure 5.6 : Minimum transverse mass after final selection cuts in ee channel. For each bin, $\chi^2 = (N_{data} - N_{MC})^2/(N_{data} + \sigma^2_{MC})$; $\chi^2/DF = [\Sigma_{bins}\chi^2]/N_{bins}$.

5.3 Event Selection in the $e\mu$ Channel

The $e\mu$ channel is based on the Common Sample Group's "EMMU" data skim, which requires one reconstructed electron object with $p_T > 5.0$ GeV and one reconstructed muon object that satisfies medium ID requirements with $p_T > 5.0$ GeV in each event. Selected events must satisfy the following conditions:

- Electron satisfies:
  - EM Fraction > 0.9, Isolation < 0.2, matched to track
  - Likelihood > 0.85
  - $|\eta_{CAL}| < 1.1$ or $1.5 < |\eta_{CAL}| < 3.0$
- Muon satisfies:
  - Medium ID requirements (At least one scintillator and two wire hits in A and BC layers of Muon System, except in the region $5\pi/4 < \phi < 7\pi/4$ with $|\eta_{MUON}| < 1.6$ where A or BC layer scintillator and wire activity will suffice)
  - Matched central track has $\chi^2/dof < 4.0$; DCA < 0.02 cm if track has SMT hits, DCA < 0.2 cm if track is CFT only
  - ($\Sigma^{tracks}|p_T|$ in a $\Delta R < 0.5$ cone around the muon) < 2.5 GeV (scalar sum of track p_T in a cone around the muon)

    - $(\Sigma^{cells}|E_T|$ in a $0.1 < \Delta R < 0.4$ hollow cone around the muon) < 2.5 GeV

      (scalar sum of calorimeter E_T in a hollow cone around the muon)

- $p_{T,lead} > 25.0$ GeV, $p_{T,trail} > 15.0$
- $\Delta R_{e\mu} > 0.5$
- Track $\Delta Z_{e\mu} < 2.0$ cm and ΔZ between the electron and the primary vertex < 2.0 cm
- Oppositely charged e, μ
- Electron is matched to and fires a single electron trigger (see Table C.1)

The total integrated luminosity represented by this data set is 1071 ± 65 pb^{-1}. Details of the luminosity calculation can be found in Appendix C.1.

After preselection, the invariant mass, shown in Figure 5.7, and the lepton ϕ and η distributions, shown in Figure 5.8, appear to be modeled well. Individual plots of the signal and background distributions of invariant mass and q_T after preselection are available in Appendix D. Missing transverse energy, $\not\!\!E_T$, and the vector sum of $\not\!\!E_T$ and charged lepton p_Ts are once again strong discriminants for separating WW signal events from many kinds of background. The distribution of these and other kinematic quantities after preselection are shown in Figure 5.9.

In the $e\mu$ final state, a significant portion of the background events come from $Z \to \tau\tau \to e\mu$ decays. The reconstructed Z mass for these events appears much lower

$e\mu$ Channel Cut Flow						
	$Z \to \tau\tau$	Z+jets	$t\bar{t}$	WZ	$W\gamma$	ZZ
Preselection	292.7 ± 4.7	67.6 ± 2.9	47.78 ± 0.60	4.71 ± 0.27	2.11 ± 0.51	0.713 ± 0.021
Cut 1	46.2 ± 1.8	25.7 ± 1.8	43.92 ± 0.58	3.87 ± 0.24	1.78 ± 0.47	0.373 ± 0.016
Cut 2	26.4 ± 1.4	4.85 ± 0.76	3.88 ± 0.17	1.44 ± 0.15	1.30 ± 0.42	0.1036 ± 0.0082
Cut 3	3.03 ± 0.45	2.17 ± 0.48	3.48 ± 0.16	1.17 ± 0.13	1.10 ± 0.39	0.0860 ± 0.0074

	W+jet	QCD	Bkg. Total	$WW \to e\mu$	$WW \to \ell\tau$	Total Expected ($\pm$ lumi)	Data
Preselection	15.7 ± 3.2	5.0 ± 4.9	436.4 ± 8.3	61.3 ± 1.0	8.41 ± 0.36	$506.0 \pm 8.4\,(\pm 30.6)$	571
Cut 1	11.3 ± 2.6	1.8 ± 1.8	134.9 ± 4.4	50.18 ± 0.91	7.19 ± 0.34	$192.3 \pm 4.6\,(\pm 11.6)$	199
Cut 2	10.8 ± 2.6	0.34 ± 0.32	49.2 ± 3.2	42.58 ± 0.84	5.90 ± 0.31	$97.7 \pm 3.4\,(\pm 5.9)$	102
Cut 3	9.3 ± 2.5	0.13 ± 0.13	20.5 ± 2.7	38.92 ± 0.80	5.11 ± 0.29	$64.5 \pm 2.8\,(\pm 3.9)$	61

Table 5.2 : Data and MC events left after preselection and each selection cut in the $e\mu$ channel. Errors include contributions from statistical, efficiency and charge mis-ID uncertainties. Cut 1 is $\not\!\!E_T >$ 20 GeV, Cut 2 is $q_T < 24$ GeV, and Cut 3 is ($\not\!\!E_T >$ 50 GeV if $\Delta\phi_{e\mu} > 2.85$). The $WW \to \ell\tau$ channel represents $WW \to e\tau/\tau\mu/\tau\tau \to e\mu$ events.

due to the three body τ decays, as can be seen in the invariant mass distribution in Figure 5.7. This reduces the utility of an invariant mass window cut, and instead the ϕ angle opening between the charged leptons, $\Delta\phi_{e\mu}$, becomes the most useful discriminant for removing $Z \to \tau\tau$ background. Additional WW signal acceptance can be retained if events with very high $\not\!\!E_T$ are not removed, even when the charged lepton ϕ opening angle is near π. The distribution of $\Delta\phi_{e\mu}$ after preselection is shown in Figure 5.9.

The optimization of signal selection, based on the significance metric defined in Section 5.1, led to the following cuts in the $e\mu$ channel:

- $\not\!\!E_T >$ 20 GeV
- $q_T <$ 24 GeV
- $\not\!\!E_T >$ 50 GeV if $\Delta\phi_{e\mu} > 2.85$

Data and MC distributions of these quantities as these cuts are individually applied are available in Figure 5.10. After signal selection, a total of 64.5 ± 2.8 (stat & syst) $\pm$ 3.9 (lumi) events are expected, and 61 events are observed. The invariant mass and minimum transverse mass distributions after all selection cuts are shown in Figure 5.11 and Figure 5.12, respectively. The largest discrepancy between data and MC in the $e\mu$ channel is the modeling of the $Z \to \tau\tau$ peak after preselection, where the MC expectation appears to be $\sim 25\%$ lower than the data. This discrepancy is accounted for by attributing an additional $+25\%$ uncertainty to the $Z \to \tau\tau$ cross section for

all channels, which results in a small increase in the overall systematic uncertainty of the WW cross section measurement (see Section 6).

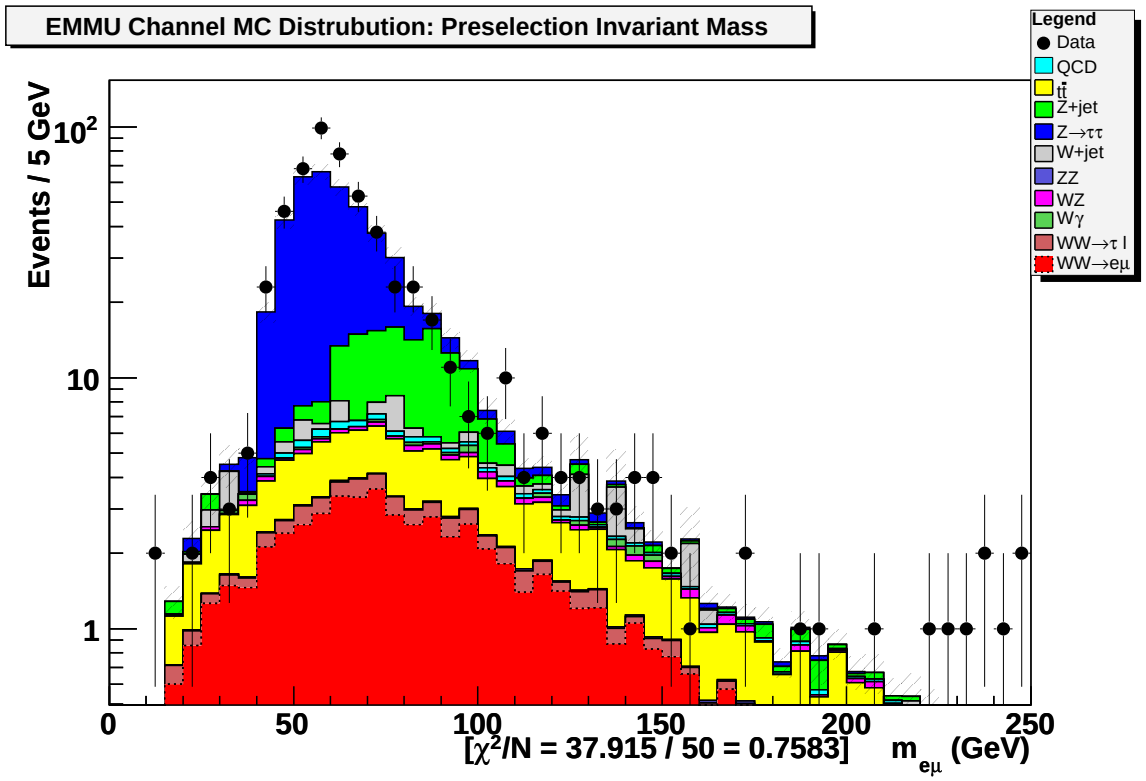

Figure 5.7 : Preselected event invariant mass distribution in the $e\mu$ channel. For each bin, $\chi^2 = (N_{data} - N_{MC})^2/(N_{data} + \sigma^2_{MC})$; $\chi^2/DF = [\Sigma_{bins}\chi^2]/N_{bins}$.

5.4 Event Selection in the $\mu\mu$ Channel

The $\mu\mu$ channel is based on the Common Sample Group's "2MUhighpt" data skim, which requires two reconstructed muon objects with "Medium" ID matched to central tracks with $p_T > 10.0$ GeV in each event. Selected muons must satisfy these conditions:

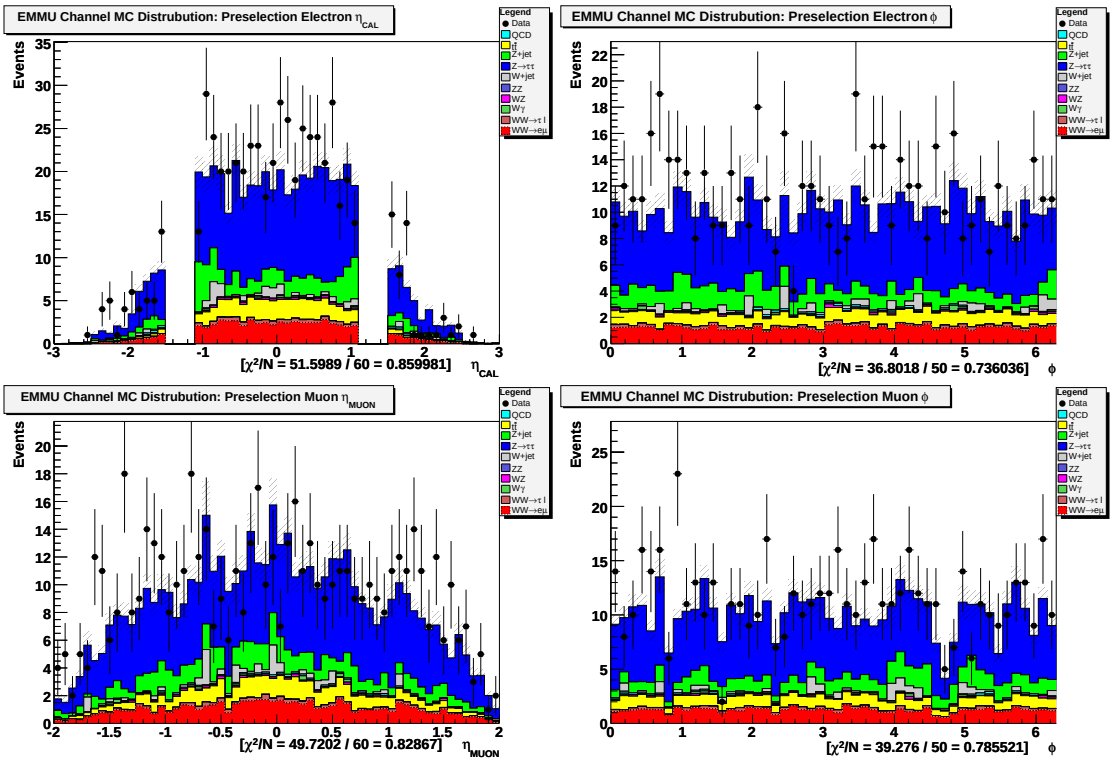

Figure 5.8 : Electron η_{CAL} and ϕ and muon η_{MUON} and ϕ distributions after preselection in the $e\mu$ Channel. For each bin, $\chi^2 = (N_{data} - N_{MC})^2/(N_{data} + \sigma^2_{MC})$; $\chi^2/DF = [\Sigma_{bins}\chi^2]/N_{bins}$.

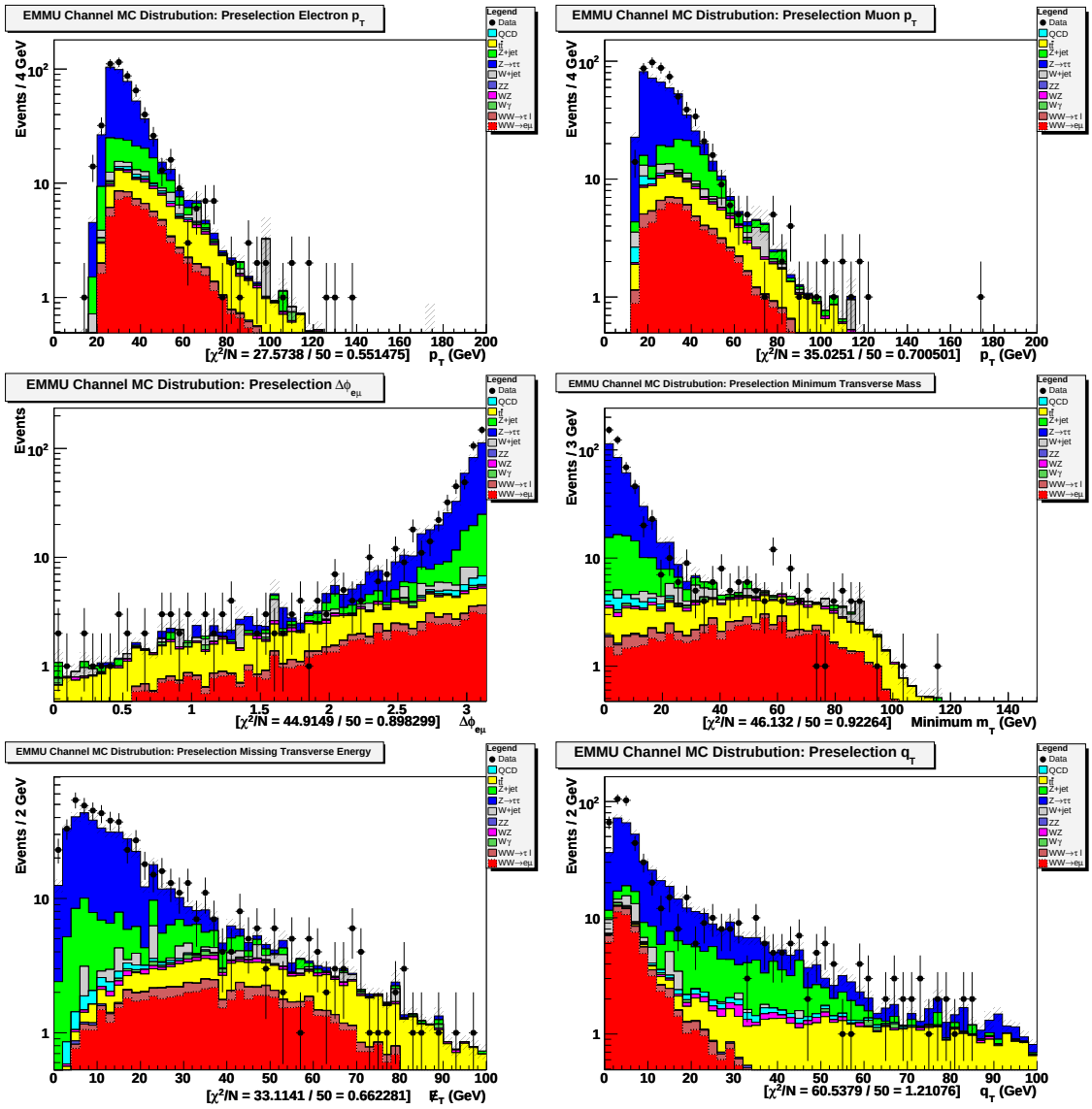

Figure 5.9 : Kinematic distributions after preselection in the $e\mu$ Channel. Clockwise, from top-left: e p_T, μ p_T, minimum transverse mass, q_T, $\not\!\!E_T$ and azimuthal separation ($\Delta\phi_{e\mu}$). For each bin, $\chi^2 = (N_{data} - N_{MC})^2/(N_{data} + \sigma^2_{MC})$; $\chi^2/DF = [\Sigma_{bins}\chi^2]/N_{bins}$.

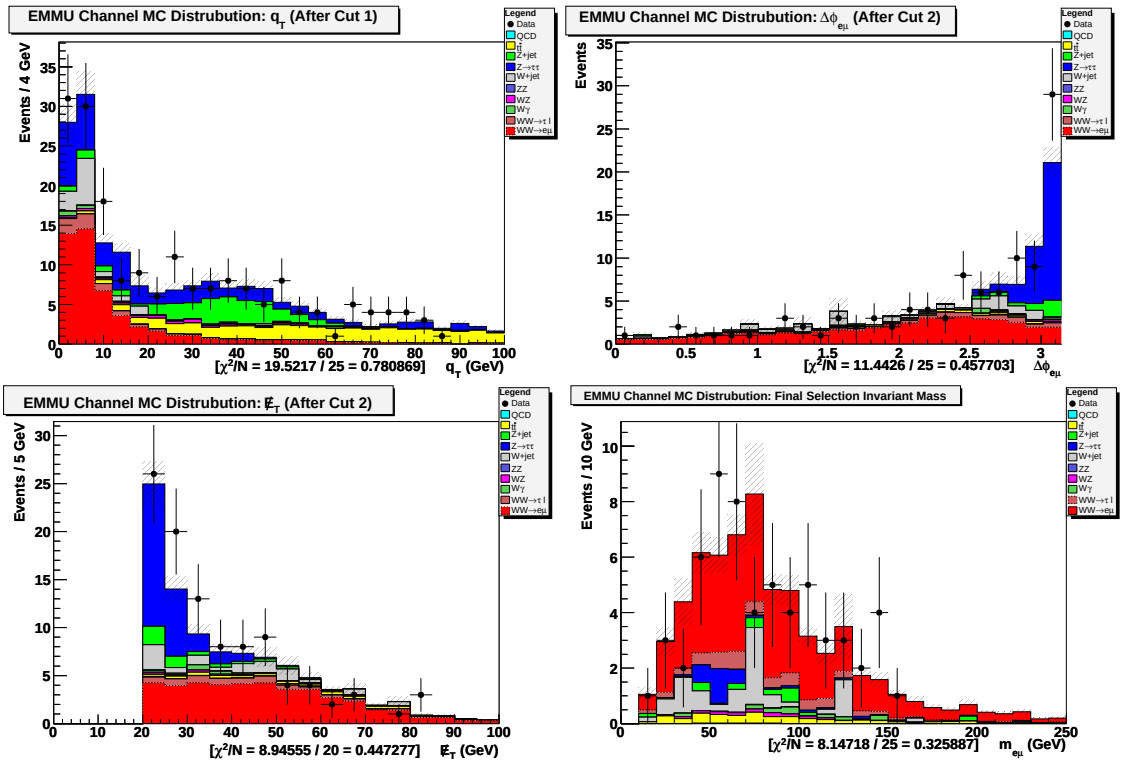

Figure 5.10 : Selection cut distributions in $e\mu$ channel. Upper left plot shows q_T distribution after $\not\!\!E_T$ cut. Upper right and lower left plots show $\Delta\phi_{e\mu}$ and $\not\!\!E_T$, respectively, after $\not\!\!E_T$ and q_T cuts. Lower right shows invariant mass distribution after all selection cuts. For each bin, $\chi^2 = (N_{data} - N_{MC})^2/(N_{data} + \sigma^2_{MC})$; $\chi^2/DF = [\Sigma_{bins}\chi^2]/N_{bins}$.

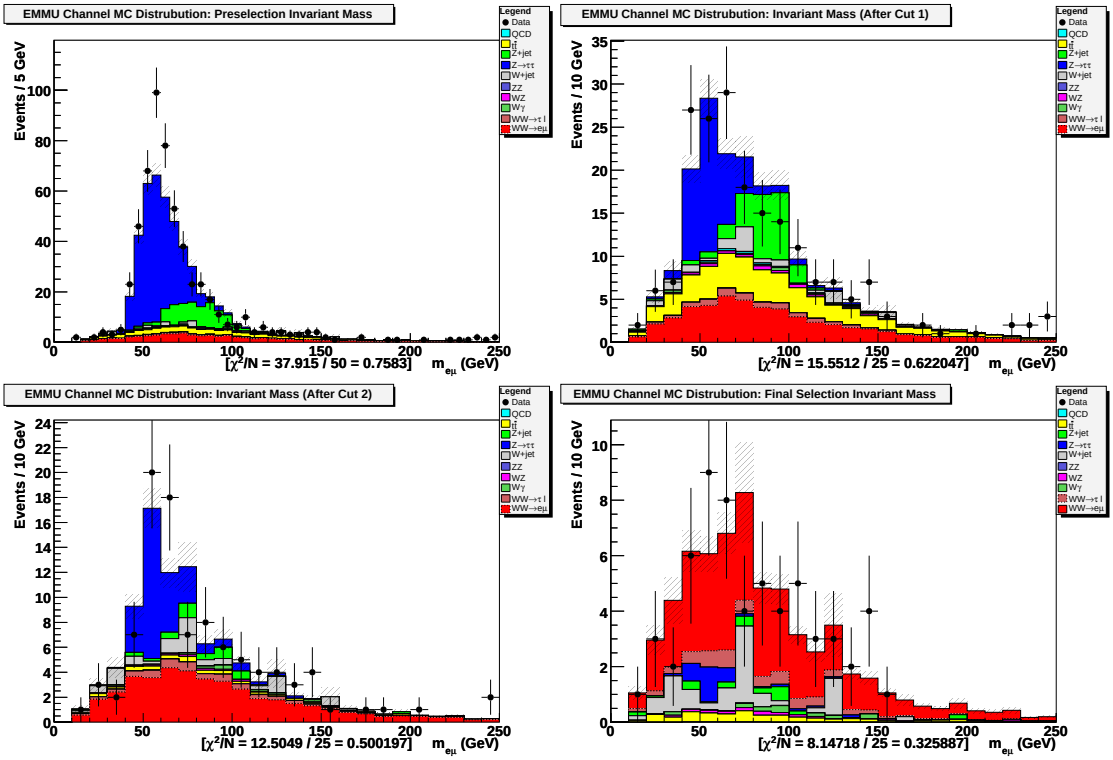

Figure 5.11 : Invariant mass distributions in $e\mu$ channel as cuts are applied. Upper left plot shows $m_{e\mu}$ distribution after preselection. Upper right shows $m_{e\mu}$ after $\not\!\!E_T$ cut. Lower left shows $m_{e\mu}$ after $\not\!\!E_T$ and q_T cuts. Lower right shows $m_{e\mu}$ after all selection cuts. For each bin, $\chi^2 = (N_{data} - N_{MC})^2/(N_{data} + \sigma^2_{MC})$; $\chi^2/DF = [\Sigma_{bins}\chi^2]/N_{bins}$.

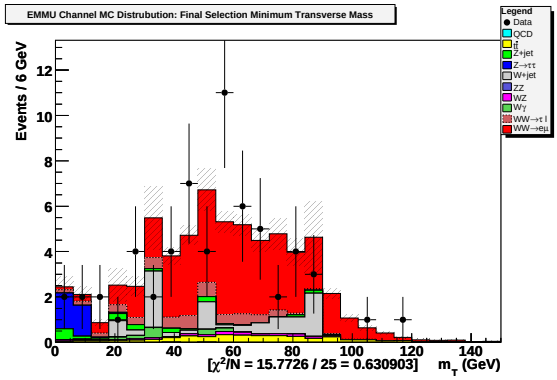

Figure 5.12 : Minimum transverse mass after final selection cuts in $e\mu$ channel. For each bin, $\chi^2 = (N_{data} - N_{MC})^2/(N_{data} + \sigma^2_{MC})$; $\chi^2/DF = [\Sigma_{bins}\chi^2]/N_{bins}$.

- Medium ID (At least one scintillator and two wire hits in A and BC layers of Muon System, except in the region $5\pi/4 < \phi < 7\pi/4$ with $|\eta_{MUON}| < 1.6$ where A or BC layer scintillator and wire activity will suffice)
- Matched central track has DCA < 0.02 cm if track has SMT hits, DCA < 0.2 cm if track is CFT only
- Matched central track has $\chi^2/dof < 4.0$
- ($\Sigma^{tracks}|p_T|$ in a $\Delta R < 0.5$ cone around the muon) < 2.5 GeV (scalar sum of track p_T in a cone around the muon)
- ($\Sigma^{cells}|E_T|$ in a $0.1 < \Delta R < 0.4$ hollow cone around the muon) < 2.5 GeV (scalar sum of calorimeter E_T in a hollow cone around the muon)
- $p_{T,lead} > 25.0$ GeV, $p_{T,trail} > 15.0$
- $\Delta R_{\mu\mu} > 0.5$
- Track $\Delta Z_{\mu\mu} < 2.0$ cm and ΔZ between lead track and primary vertex < 2.0 cm
- Oppositely charged muons
- Either muon is matched to and fires a single muon trigger (see Table C.2)

A muon is considered to fire a trigger if it is spatially matched to all L1, L2 and L3 components of a specific trigger and that trigger fired during the event. The single muon triggers used in this analysis, listed in Table C.2, are part of the standard DØ

"Single Muon Trigger OR" [51]. The total integrated luminosity represented by this data set is 1002 ± 61 pb^{-1}. Details of the luminosity calculation can be found in [51].

After preselection, the invariant mass, shown in Figure 5.13, and the lepton ϕ and η distributions, shown in Figure 5.14, appear to be modeled well. Individual plots of the signal and background distributions of invariant mass and q_T after preselection are available in Appendix D. Missing transverse energy, $\not\!\!E_T$, and q_T are once again strong discriminants for separating WW signal events from many kinds of background. The distributions of these and other kinematic quantities after preselection are shown in Figure 5.15.

Because the momentum resolution for high p_T muons is worse than that for high p_T electrons, a $|M_Z - m_{\mu\mu}|$ mass window cut is not as effective at rejecting $Z \to \mu\mu$ background as the similar cut in the ee channel is at remove $Z \to ee$ events. Instead, a cut on $\Delta\phi_{\mu\mu}$ provides superior Z background rejection. Additionally, because mismeasured high p_T muons are a source for fake $\not\!\!E_T$, events are rejected if, for either muon, $\cos(\Delta\phi_{\not\!\!E_T,\mu}) > 0.98$, where $\Delta\phi_{\not\!\!E_T,\mu}$ is the azimuthal separation between the $\not\!\!E_T$ and either muon. The distributions of these quantities after preselection are shown in Figure 5.15.

The optimization of signal selection, based on the significance metric defined in Section 5.1, led to the following cuts in the $\mu\mu$ channel:

- $\not\!\!E_T > 35$ GeV
- $\cos(\Delta\phi_{\not\!\!E_T,\mu}) < 0.98$ (for both muons)

- $q_T < 19$ GeV
- $\Delta\phi_{\mu\mu} < 2.55$

Data and MC distributions of these quantities as these cuts are individually applied are available in Figure 5.16. After signal selection, a total of 20.7 ± 2.3 (stat & syst) $\pm$ 1.3 (lumi) events are expected, and 21 events are observed. The invariant mass and minimum transverse mass distributions after all selection cuts are shown in Figure 5.17 and Figure 5.18, respectively. Agreement between data and the signal plus background estimates is good for all distributions after preselection except for the invariant mass, which shows an excess at low $m_{\mu\mu}$. These events are likely due to low mass Drell-Yan that include muons with mismeasured p_T. This theory is supported by the fact that the excess at low $m_{\mu\mu}$ disappears after imposing the $\not\!\!E_T$ selection cut. The signal plus backgrounds underestimate the data after the $\not\!\!E_T$ cut because the muon momentum resolution in MC does not match that in data even after the additional muon smearing discussed in Section 4.5. Applying the "$\not\!\!E_T$ clean-up" cut of $\cos(\Delta\phi_{\not\!\!E_T,\mu}) < 0.98$ removes data events that likely contain a grossly mismeasured muon, and restores agreement between the data and the signal plus background estimates.

$\mu\mu$ Channel Cut Flow						
	$Z \to \mu\mu$	$Z \to \tau\tau$	$t\bar{t}$	WZ	ZZ	W+jet
Preselection	50151.7 ± 106.3	152.6 ± 6.6	21.19 ± 0.39	25.58 ± 0.61	4.420 ± 0.059	7.2 ± 2.5
Cut 1	655.7 ± 9.2	5.6 ± 1.1	16.80 ± 0.35	6.99 ± 0.32	2.475 ± 0.045	5.8 ± 2.3
Cut 2	102.6 ± 3.9	2.13 ± 0.73	12.58 ± 0.30	4.35 ± 0.26	1.688 ± 0.037	5.0 ± 2.3
Cut 3	26.8 ± 1.9	0.022 ± 0.015	0.553 ± 0.060	1.66 ± 0.16	1.253 ± 0.032	4.4 ± 2.2
Cut 4	3.01 ± 0.67	0 ± 0	0.444 ± 0.055	1.30 ± 0.13	1.107 ± 0.031	4.4 ± 2.2

	QCD	Bkg. Total	$WW \to \mu\mu$	$WW \to \ell\tau$	Total Expected ($\pm$ lumi)	Data
Preselection	0 ± 1.8	50362.7 ± 108.0	28.81 ± 0.66	4.50 ± 0.26	50396.0 ± 108.1 (± 3074.2)	52477
Cut 1	0 ± 0.38	693.4 ± 9.7	17.73 ± 0.53	2.48 ± 0.19	713.6 ± 9.7 (± 43.5)	915
Cut 2	0 ± 0.082	128.4 ± 4.6	13.71 ± 0.47	1.55 ± 0.15	143.6 ± 4.7 (± 8.8)	147
Cut 3	0 ± 0.019	34.7 ± 2.9	10.71 ± 0.41	1.20 ± 0.13	46.6 ± 3.0 (± 2.8)	60
Cut 4	0 ± 0.0062	10.2 ± 2.3	9.45 ± 0.38	1.01 ± 0.12	20.7 ± 2.3 (± 1.3)	21

Table 5.3 : Data and MC events left after preselection and each selection cut in the $\mu\mu$ channel. Errors include contributions from statistical, efficiency and charge mis-ID uncertainties. Cut 1 is $\not\!\!E_T > 35$ GeV, Cut 2 is $\cos(\Delta\phi_{\not\!\!E_T,\mu}) < 0.98$, Cut 3 is $q_T < 19$ GeV, and Cut 4 is $\Delta\phi_{\mu\mu} < 2.55$. The $WW \to \ell\tau$ channel represents $WW \to \mu\tau/\tau\tau \to \mu\mu$ events.

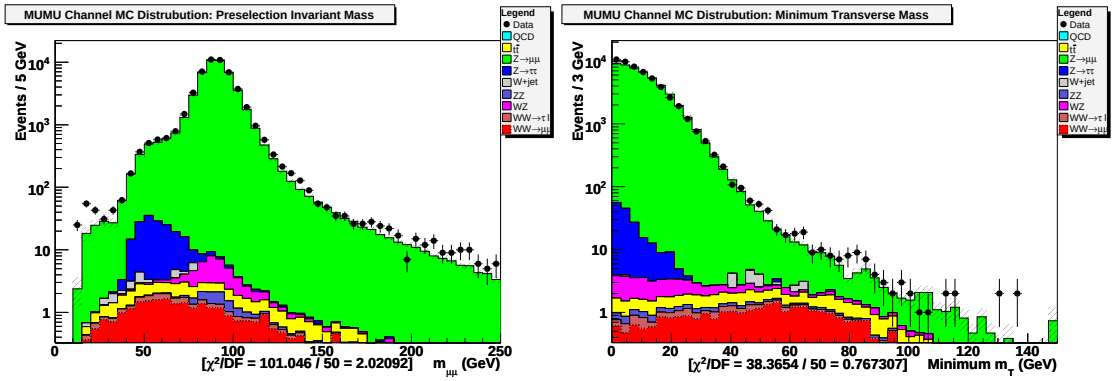

Figure 5.13 : Invariant mass (left) and minimum transverse mass (right) distributions after preselection in the $\mu\mu$ channel. For each bin, $\chi^2 = (N_{data} - N_{MC})^2/(N_{data} + \sigma^2_{MC})$; $\chi^2/DF = [\Sigma_{bins}\chi^2]/N_{bins}$.

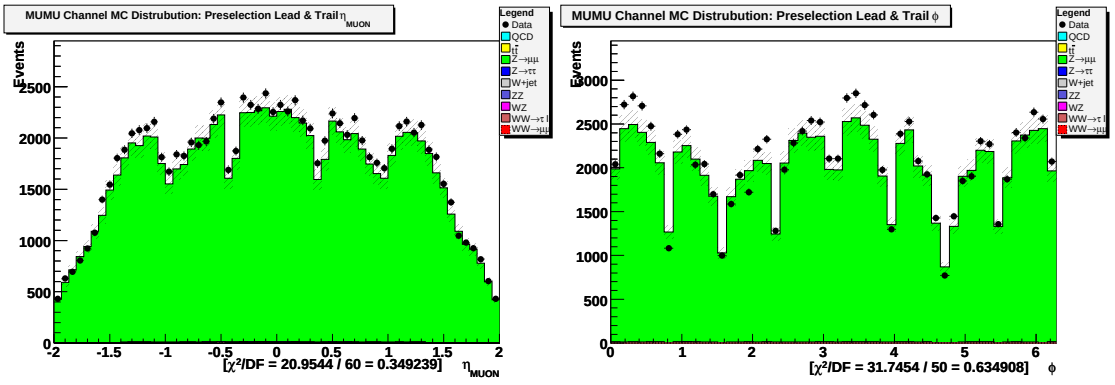

Figure 5.14 : Leading and trailing muon η_{MUON} and ϕ distributions after preselection in the $\mu\mu$ Channel. For each bin, $\chi^2 = (N_{data} - N_{MC})^2/(N_{data} + \sigma^2_{MC})$; $\chi^2/DF = [\Sigma_{bins}\chi^2]/N_{bins}$.

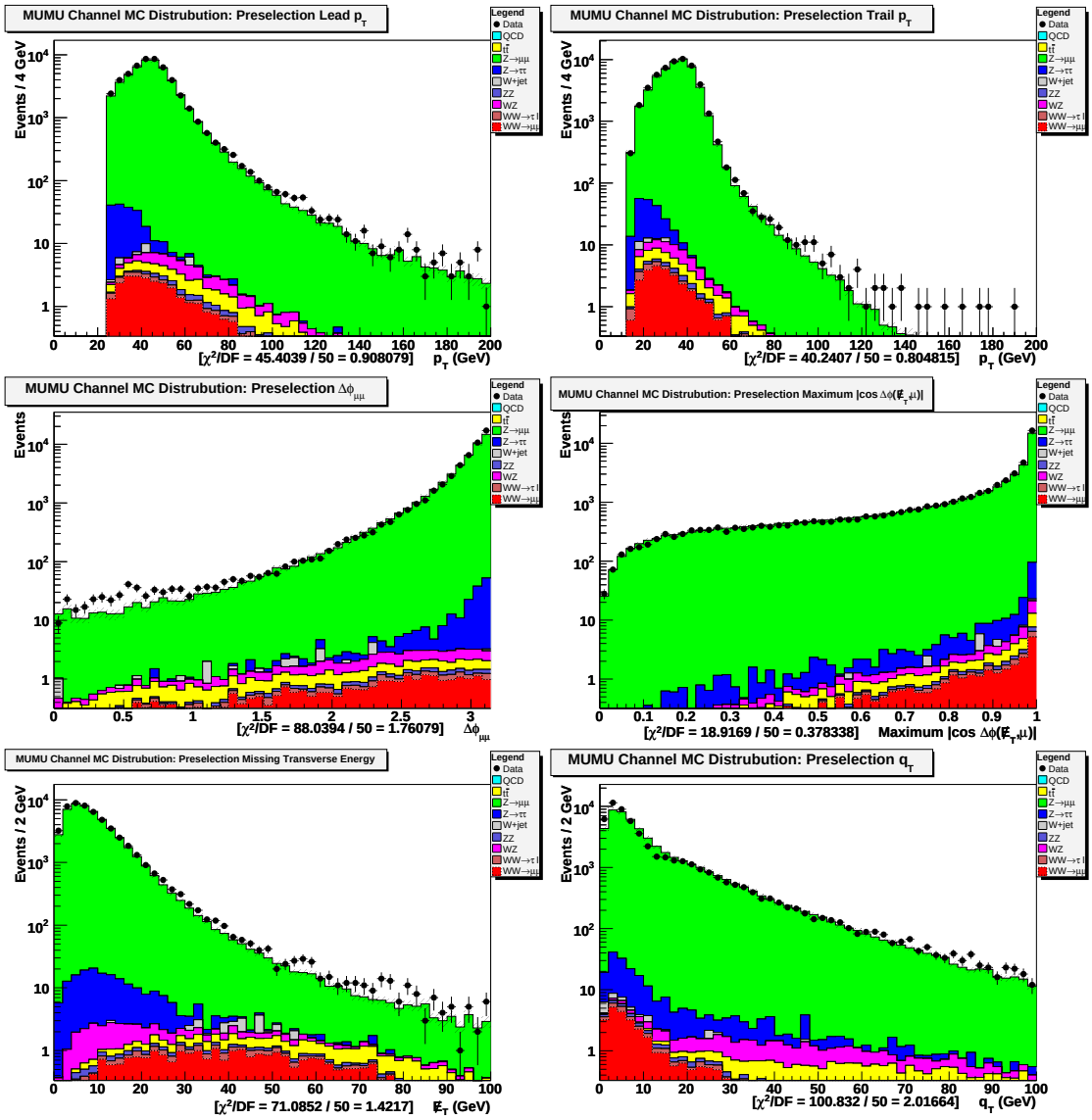

Figure 5.15 : Kinematic distributions after preselection in the $\mu\mu$ Channel. Clockwise, from top-left: leading μ p_T, trailing μ p_T, maximum $\cos(\Delta\phi_{\not{E}_T,\mu})$, q_T, $\not{E}_T$ and azimuthal separation ($\Delta\phi_{\mu\mu}$). For each bin, $\chi^2 = (N_{data} - N_{MC})^2/(N_{data} + \sigma^2_{MC})$; $\chi^2/DF = [\Sigma_{bins}\chi^2]/N_{bins}$.

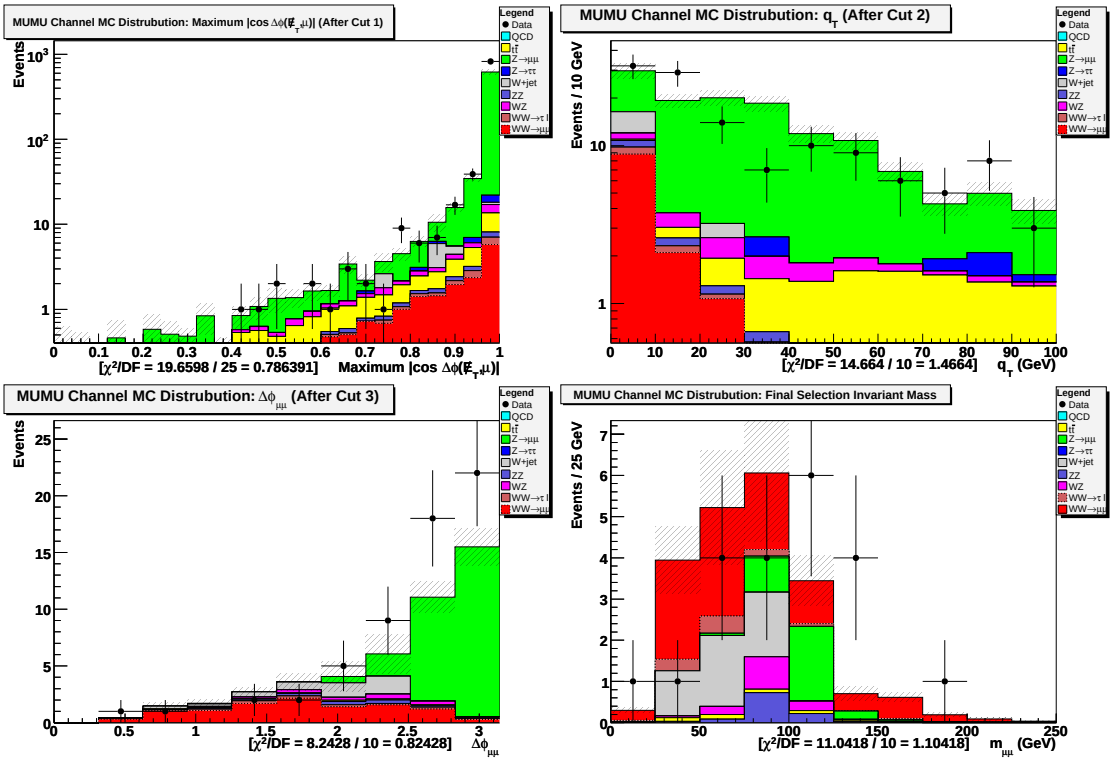

Figure 5.16 : Selection cut distributions in $\mu\mu$ channel. Top left plot shows maximum $\cos(\Delta\phi_{\not\!\!E_T,\mu})$ distribution after $\not\!\!E_T$ cut. Top right plots shows q_T after $\not\!\!E_T$ and maximum cosine cut. Lower left plot shows $\Delta\phi_{\mu\mu}$ after $\not\!\!E_T$, q_T and maximum cosine selection cuts are applied. Lower right plot shows invariant mass distribution after all selection cuts are applied. For each bin, $\chi^2 = (N_{data} - N_{MC})^2/(N_{data} + \sigma^2_{MC})$; $\chi^2/DF = [\Sigma_{bins}\chi^2]/N_{bins}$.

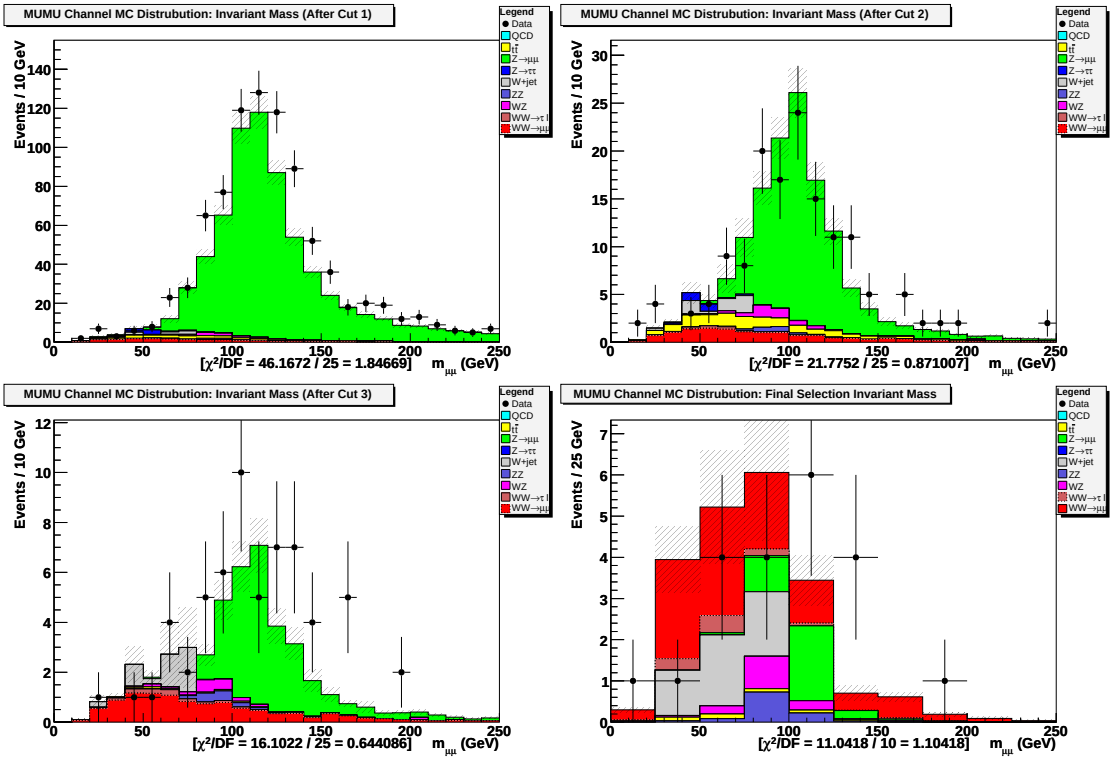

Figure 5.17 : Invariant mass distributions in $\mu\mu$ channel as cuts are applied. Upper left shows $m_{\mu\mu}$ after $\not\!\!E_T$ cut. Upper right shows $m_{\mu\mu}$ after $\not\!\!E_T$ and $\cos(\Delta\phi_{\not\!\!E_T,\mu})$ cuts. Lower left shows $m_{\mu\mu}$ after $\not\!\!E_T$, $\cos(\Delta\phi_{\not\!\!E_T,\mu})$ and q_T cuts. Lower right shows $m_{\mu\mu}$ after all selection cuts. For each bin, $\chi^2 = (N_{data} - N_{MC})^2/(N_{data} + \sigma^2_{MC})$; $\chi^2/DF = [\Sigma_{bins}\chi^2]/N_{bins}$.

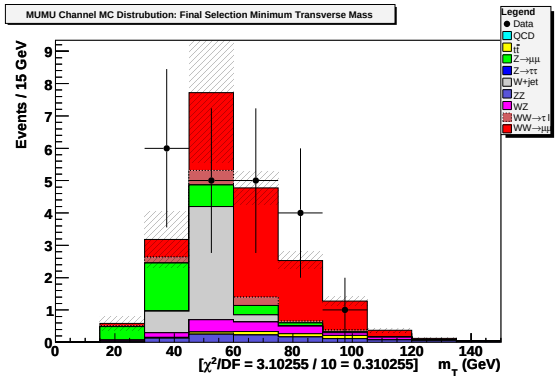

Figure 5.18 : Minimum transverse mass after final selection cuts in $\mu\mu$ channel. For each bin, $\chi^2 = (N_{data} - N_{MC})^2/(N_{data} + \sigma^2_{MC})$; $\chi^2/DF = [\Sigma_{bins}\chi^2]/N_{bins}$.

Chapter 6

Cross-section Calculation

The cross section calculation is based on the number of data and MC events remaining after the selection process for each channel, as described in Sec. 5. Data and MC events remaining after signal selection in the ee, $e\mu$ and $\mu\mu$ channels can be found in Tables 5.1, 5.2 and 5.3, respectively.

The final acceptance of each channel is based on the PYTHIA WW MC sample. The final acceptance for each channel is shown in Tab. 6.1.

Process	BR	$A \times \varepsilon$
$WW \to ee$	1.16 %	8.68 ± 0.43 %
$WW \to \tau e/\tau\tau \to ee$	0.47 %	2.99 ± 0.39 %
$WW \to e\mu$	2.27 %	13.32 ± 0.27 %
$WW \to \tau\ell \to e\mu$	0.92 %	4.31 ± 0.24 %
$WW \to \mu\mu$	1.12 %	7.03 ± 0.28 %
$WW \to \tau\mu/\tau\tau \to \mu\mu$	0.45 %	1.87 ± 0.22 %

Table 6.1 : Final acceptance and efficiency for each decay channel, where $A \times \varepsilon_P$ is the final acceptance times efficiency value after all selection cuts have been applied.

Except where noted, systematic uncertainty includes effects from lepton ID efficiency (see Appendix C.2), charge misidentification (see Section 4.5), triggering [50, 51] and statistical uncertainties in MC background samples, acceptance times efficiency uncertainty in MC signal samples, and scale factor uncertainties in the QCD

background estimation (see Section 4.6).

In the ee final state, a total of 25.2 ± 1.6 (stat & syst) $\pm$ 1.5 (lumi) events are expected, and 26 events are observed. The expected number of background events in the ee channel is 10.1 ± 1.4 (stat & syst) $\pm$ 0.6 (lumi). Observations in this channel correspond to a WW cross section of 12.60 ± 4.04 (stat) $\pm$ 1.24 (syst) $\pm$ 0.77 (lumi) pb.

In the $e\mu$ final state, a total of 64.5 ± 2.8 (stat & syst) $\pm$ 3.9 (lumi) events are expected, and 61 events are observed. The expected number of background events in the $e\mu$ channel is 20.5 (stat & syst) $\pm$ 2.71.3 (lumi). Observations in this channel correspond to a WW cross section of 11.04 ± 2.13 (stat) $\pm$ 0.76 (syst) $\pm$ 0.67 (lumi) pb.

In the $\mu\mu$ final state, a total of 20.7 ± 2.3 (stat & syst) $\pm$ 1.3 (lumi) events are expected, and 21 events are observed. The expected number of background events in the $\mu\mu$ channel is 21 (stat & syst) $\pm$ 2.30.6 (lumi). Observations in this channel correspond to a WW cross section of 12.34 ± 5.26 (stat) $\pm$ 2.67 (syst) $\pm$ 0.75 (lumi) pb.

The WW cross section corresponding to the combined observations across all three final states, ee, $e\mu$ and $\mu\mu$, is 11.58 ± 1.79 (stat) ± 0.68 (syst) ± 0.71 (lumi) pb. Further contributions to systematic uncertainties are considered, including MC cross section uncertainties and W and τ branching ratio uncertainties. The $Z \to \tau\tau$ process systematic contribution has been modified to include a +25% uncertainty on the MC

cross section, to account for the discrepancy between data and MC in the $e\mu$ channel after preselection. These contributions to the systematic uncertainty in each channel are shown in Tab. 6.2. The final WW cross section measurement, accounting for all systematic uncertainties, is:

$$\sigma(p\bar{p} \rightarrow WW) = 11.6 \pm 1.8 \text{ (stat)} \pm 0.7 \text{ (syst)} \pm 0.7 \text{ (lumi) pb.}$$

In comparison, the theoretical cross section calculated using MCFM (a cross section calculator for hadron-hadron colliders) and CTEQ6M (a specific parton distribution function) is 12.0 ± 0.6 (scale) ± 0.3 (PDF) pb [44]. The latest public result from the CDF collaboration is $\sigma(p\bar{p} \rightarrow WW) = 13.6 \pm 2.3(\text{stat}) \pm 1.6(\text{syst}) \pm 1.2(\text{lum})$ pb, using 825 pb^{-1} [52]. The most recent published result from the Fermilab Tevatron Collider is $\sigma(p\bar{p} \rightarrow WW) = 11.8^{+3.7}_{-3.3}(\text{stat})\,^{+1.0}_{-0.8}(\text{syst}) \pm 0.6(\text{lum})$ pb, using 224-252 pb^{-1} [53].

Systematic Source	ee		$e\mu$		$\mu\mu$		Combination	
Background Estimation	-9.84	9.84	-6.86	6.86	-21.63	21.63	-5.87	5.87
$Z \to \ell\ell$	-0.82	0.32	-1.97	0.6	-0.56	1.31	-1.47	0.65
$t\bar{t}$	-0.54	0.54	-0.59	0.59	-0.28	-0.28	-0.53	0.44
WZ	-0.65	0.65	-0.2	0.2	-0.82	0.82	-0.4	0.4
$W\gamma$ (ISR)	-0.33	0.33	-0.23	0.23	—		-0.22	0.22
ZZ	-0.62	0.62	-0.01	0.01	-0.58	0.58	-0.25	0.25
W+jet	-0.89	0.79	-0.84	0.75	-1.49	1.32	-0.96	0.85
MC σ Total	-1.63	1.39	-2.25	1.17	-1.9	2.14	-1.91	1.27
BR($W \to e$)	-2.22	2.3	-1.12	1.15	—		-1.2	1.22
BR($W \to \mu$)	—		-1.31	1.35	-2.64	2.74	-1.23	1.26
BR($W \to \tau$)	-0.24	0.24	-0.22	0.22	-0.19	0.19	-0.22	0.22
BR($\tau \to e$)	-0.04	0.04	-0.02	0.02	—		-0.02	0.02
BR($\tau \to \mu$)	—		-0.02	0.02	-0.03	0.03	-0.02	0.02
BR Total	-2.23	2.31	-1.74	1.78	-2.64	2.75	-1.73	1.77
Total Systematic (%)	-10.22	10.2	-7.42	7.18	-21.88	21.91	-6.41	6.26
Total Systematic (pb)	-1.29	1.29	-0.82	0.79	-2.7	2.7	-0.74	0.72

Table 6.2 : Systematic uncertainties (in percent, except where noted) for the WW cross section measurement in each channel individually and in the combination of all three channels. Background estimation systematics include contributions from lepton ID efficiency, charge misidentification, triggering and statistical uncertainties in MC background samples, acceptance times efficiency uncertainty in MC signal samples, and scale factor uncertainties in the QCD background estimation. See Tab. 4.1 for the errors on MC cross sections used to calculate these contributions. The $Z \to \tau\tau$ process includes a +25% uncertainty on the MC cross section, to account for the discrepancy between data and MC in the $e\mu$ channel after preselection.

Chapter 7

Trilinear Gauge Coupling Limits

7.1 Simplifying Assumptions Used in Limit Setting

The fourteen complex terms found in the general effective Lagrangian in Equation 1.8 are too numerous to be studied effectively, so dynamical principles are used in order to reduce the number of terms. If electromagnetic gauge invariance is enforced and CP-violating terms are removed (since, as an approximate symmetry principle, CP-violation is expected to be small) the effective Lagrangian is reduced to:

$$\frac{\mathcal{L}_{WWV}}{g_{WWV}} = ig_1^V(W^\dagger_{\mu\nu}W^\mu V^\nu - W^\dagger_\mu V_\nu W^{\mu\nu}) + i\kappa_V W^\dagger_\mu W_\nu V^{\mu\nu} + \frac{i\lambda_V}{M_W^2}W^\dagger_{\lambda\mu}W^\mu{}_\nu V^{\nu\lambda} \quad (7.1)$$

where $V = \gamma$ or Z, W^μ is the W^- field, $W_{\mu\nu} = \partial_\mu W_\nu - \partial_\nu W_\mu$, $V_{\mu\nu} = \partial_\mu V_\nu - \partial_\nu V_\mu$, the overall couplings are $g_{WW\gamma} = -e$ and $g_{WWZ} = -e\cot\theta_W$, and $g_1^Z = 1$. In the Standard Model, the five remaining couplings are fixed to the values $g_1^Z = \kappa_Z = \kappa_\gamma = 1$ and $\lambda_Z = \lambda_\gamma = 0$.

Finally, precision measurements from the CERN e^+e^- Collider (LEP) provide a stringent test of the $SU(2)_L \otimes U(1)_Y$ structure of electroweak interactions. Enforcing this symmetry introduces two relationships between the remaining parameters, reducing the number of free parameters to three [10]:

$$\kappa_Z = g_1^Z - (\kappa_\gamma - 1)\tan^2\theta_W \quad (7.2)$$

$$\lambda_Z = \lambda_\gamma \tag{7.3}$$

By parameterizing the effect that varying each of the free parameters has on the expected WW cross section and kinematic behavior, and comparing that expectation to data, a 95% C.L. interval will be set for each individual parameter. Additionally, 95% C.L. contours will be set for the three planes where one of the three free parameters is fixed to its Standard Model value.

7.2 Generating Limits on Anomalous Couplings

A leading order generator by Hagiwara, Woodside and Zeppenfeld is used to model the behavior of the WW system as coupling parameters are varied about their Standard Model values [7]. A total of 99 points in three-dimensional ($\Delta\kappa_\gamma$,λ_γ,Δg_1^Z) space are generated in order to define the behavior of the anomalous WW system.

Generated events for each point are passed through the Parameterized Monte Carlo Simulation (PMCS, version p20br-v04-03 [54]) to simulate the efficiency, acceptance and smearing effects of the DØ detector, then passed through the same selection cuts used in the cross section measurement. Appropriate efficiencies are applied for object selection, along with the same trigger efficiencies that are applied in the cross section analysis. The absolute scale of each grid of points is set by the Standard Model point within the grid, which is forced to match the number of expected WW events in that decay channel.

Because two neutrinos are produced in fully leptonic WW decays, the production

angles of the bosons cannot be reconstructed, leaving the overall cross section and the charged lepton p_T values as the most sensitive variables to anomalous couplings. In order to enhance the sensitivity to anomalous couplings, events are binned two-dimensionally in lepton p_T, using leading and trailing lepton p_T values in the ee and $\mu\mu$ channels, and e and μ p_T values in the $e\mu$ channel.

For each bin in lepton p_T space, the expected number of WW events produced is parameterized in ($\Delta\kappa_\gamma$,λ_γ,Δg_1^Z) space using this function:

$$N_{WW} = p_0 + p_1 x + p_2 y + p_3 z + p_4 xy + p_5 yz + p_6 xz + p_7 x^2 + p_8 y^2 + p_9 z^2 \qquad (7.4)$$

where $x = \Delta\kappa_\gamma$, $y = \lambda_\gamma$, $z = \Delta g_1^Z$ and each p_n represents a free parameter in a three dimensional fit.

For a given pair of anomalous coupling parameters, for instance $\Delta\kappa_\gamma$ and λ_γ when Δg_1^Z is set to zero, a two-dimensional likelihood surface is produced in the following manner. Small steps are taken in $\Delta\kappa_\gamma$ and λ_γ space, such that the generated likelihood values can later be numerically integrated in order to produce a 95% C.L. contour. At each of these steps, the expected number of signal events for each p_T bin, estimated by using the appropriate parameterized function, and the expected background, taken from the cross section analysis, are compared to the number of data events observed by calculating a bin-by-bin likelihood across all p_T bins in all final state channels. Each bin is assumed to have a Poisson distribution with a mean equal to the sum of the signal and background bins. The errors on the signal and background distributions are accounted for by weighting with Gaussian distributions. Correlations between

the signal and background errors for each channel are assumed to be small, so they are considered separately. The error on the luminosity is considered to be 100% correlated, and so varies the same way for all channels. The likelihood is calculated as

$$L = \int \mathcal{G}_{f_l} P_{ee}(f_l) P_{e\mu}(f_l) P_{\mu\mu}(f_l) df_l \tag{7.5}$$

$$P_{\ell\ell'}(f_l) = \int \mathcal{G}_{f_n} \int \mathcal{G}_{f_b} \prod_{i=1}^{N_{\text{bins}}} \mathcal{P}\left(N^i_{\ell\ell'}; (f_l f_n n^i_{\ell\ell'} + f_l f_b b^i_{\ell\ell'})\right) df_n df_b \tag{7.6}$$

where $\mathcal{P}(a;\alpha)$ is the Poisson probability of obtaining a events if the mean expected number is α, $n^i_{\ell\ell'}$ and $b^i_{\ell\ell'}$ are the simulated number of signal and background events for the $\ell\ell'$ channel in bin i, $N^i_{\ell\ell'}$ is the measured number of events for this channel in this bin, and f_l, f_n and f_b are the luminosity, signal, and background weights drawn from the Gaussian distributions $\mathcal{G}_{f_l}$, $\mathcal{G}_{f_n}$ and $\mathcal{G}_{f_b}$ respectively.

The resultant likelihood surface is numerically integrated in order to find the 95% C.L. contour. During the integration, the highest likelihood bin not yet included in the integrated volume is always chosen as the next bin to include. One dimensional 95% C.L. intervals are calculated in a similar manner, by numerically integrating along a line.

7.3 Anomalous Coupling Limits

The final selected data from each channel of the cross section analysis are divided into two-dimensional bins based on the p_T of the charged leptons as shown in Figure 7.1.

Comparisons between the three-dimensional fits in ($\Delta\kappa_\gamma$, λ_γ and Δg_1^Z) space to the

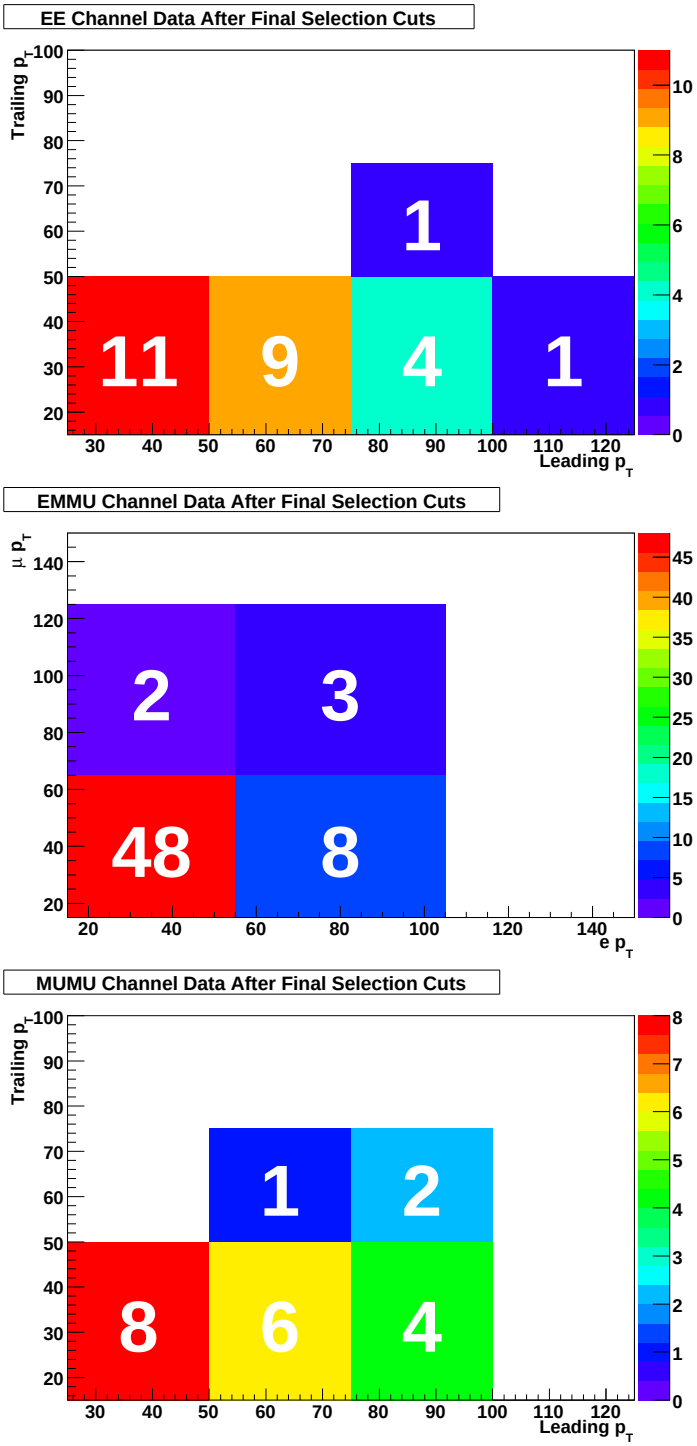

Figure 7.1 : Final selected data from the ee (top), $e\mu$ (center) and $\mu\mu$ (bottom) final states, as divided in charged lepton p_T for trilinear gauge coupling limit setting procedures. The superimposed numbers represent the amount of data in each bin.

simulated number of WW events from various grid points are shown in Figures 7.2, 7.3 and 7.4 for the ee, $e\mu$ and $\mu\mu$ channels, respectively.

One- and two-dimensional 95% C.L. limits on anomalous values of the trilinear gauge couplings, using the constraints from Equations 7.2 and 7.3 and a dipole form factor with $\Lambda = 2$ TeV, can be found in Figures 7.5-7.7. The one-dimensional 95% C.L. limits on the three free couplings under study are:

$$-0.63 < \Delta\kappa_\gamma < 0.99$$

$$-0.15 < \lambda_\gamma < 0.19$$

$$-0.14 < \Delta g_1^Z < 0.34$$

The previously published one-dimensional 95% C.L. limits from a WW study at DØ are summarized in Table 7.1. In the previous publication, various sets of TGC relationships were studied, including:

- $WW\gamma = WWZ$: $\Delta\kappa_\gamma = \Delta\kappa_Z$, $\lambda_\gamma = \lambda_Z$ and $g_1^Z = 0$
- HISZ: $\Delta\kappa_Z = \Delta\kappa_\gamma(1 - \tan^2\theta_W)$, $\Delta g_1^Z = \Delta\kappa_\gamma/(2\cos^2\theta_W)$ and $\lambda_Z = \lambda_\gamma$
- Standard Model WWZ: $\Delta\kappa_Z = \lambda_Z = g_1^Z = 0$
- Standard Model $WW\gamma$: $\Delta\kappa_\gamma = \lambda_\gamma = g_1^Z = 0$

Since the HISZ constraints conserve $SU(2)_L \otimes U(1)_Y$ gauge symmetry, they may be the most comparable previous result to the limits set in this analysis. However, in the HISZ model, the sensitivity to $\Delta\kappa_\gamma$ is enhanced through its dependence on g_1^Z. The

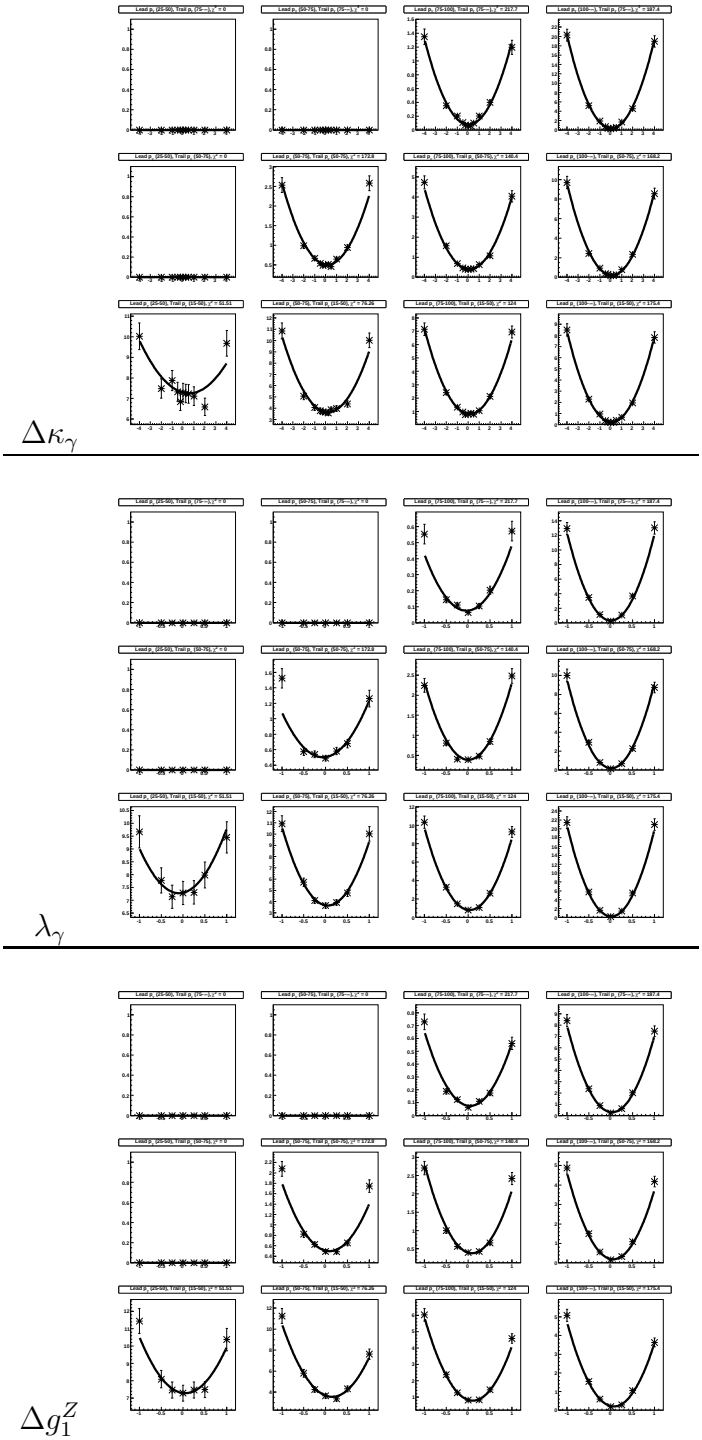

Figure 7.2 : Comparison in the *ee* channel of the three-dimensional fit in ($\Delta\kappa_\gamma$, λ_γ, Δg_1^Z) space to the simulated number of WW events along the $\Delta\kappa_\gamma$ axis (top), λ_γ axis (center) and Δg_1^Z (bottom). Each fit in a set is labeled with respect to the two-dimensional p_T bin it represents.

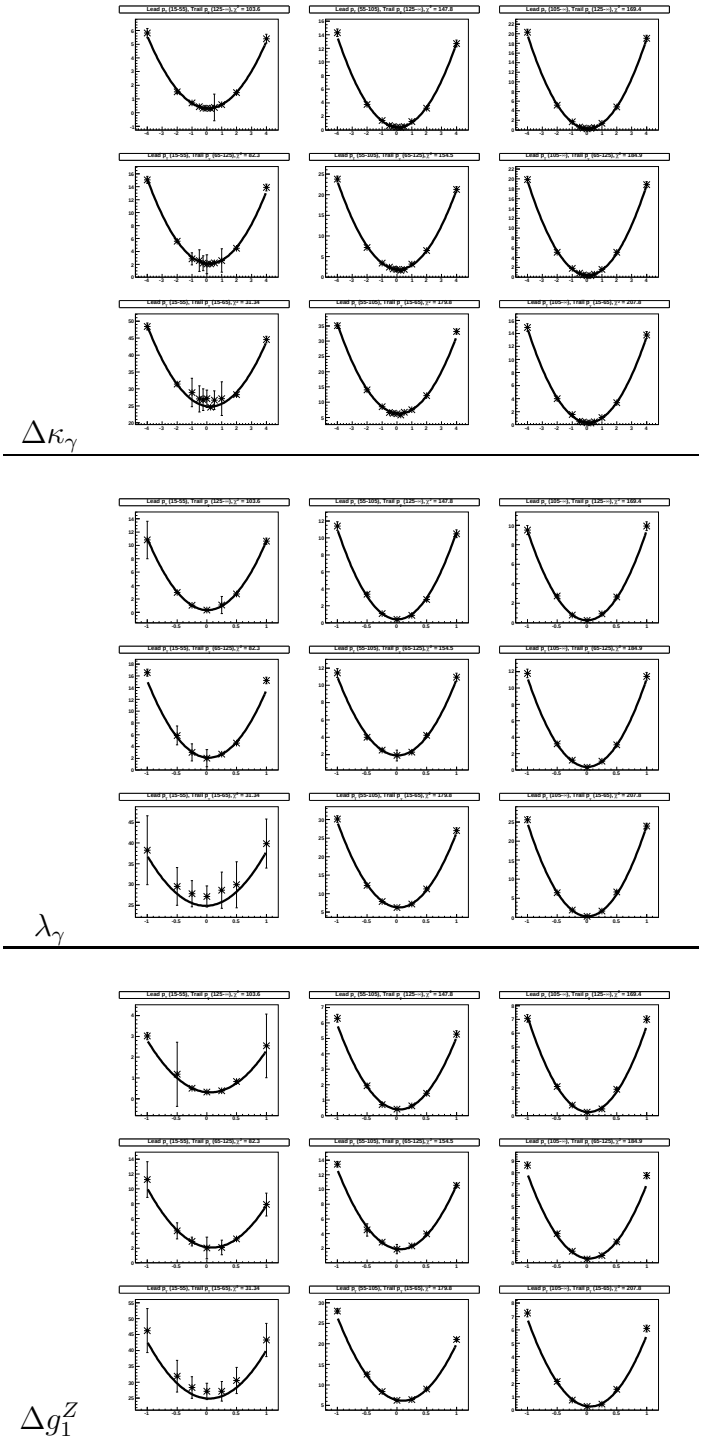

Figure 7.3 : Comparison in the $e\mu$ channel of the three-dimensional fit in ($\Delta\kappa_\gamma$, λ_γ, Δg_1^Z) space to the simulated number of WW events along the $\Delta\kappa_\gamma$ axis (top), λ_γ axis (center) and Δg_1^Z (bottom). Each fit in a set is labeled with respect to the two-dimensional p_T bin it represents.

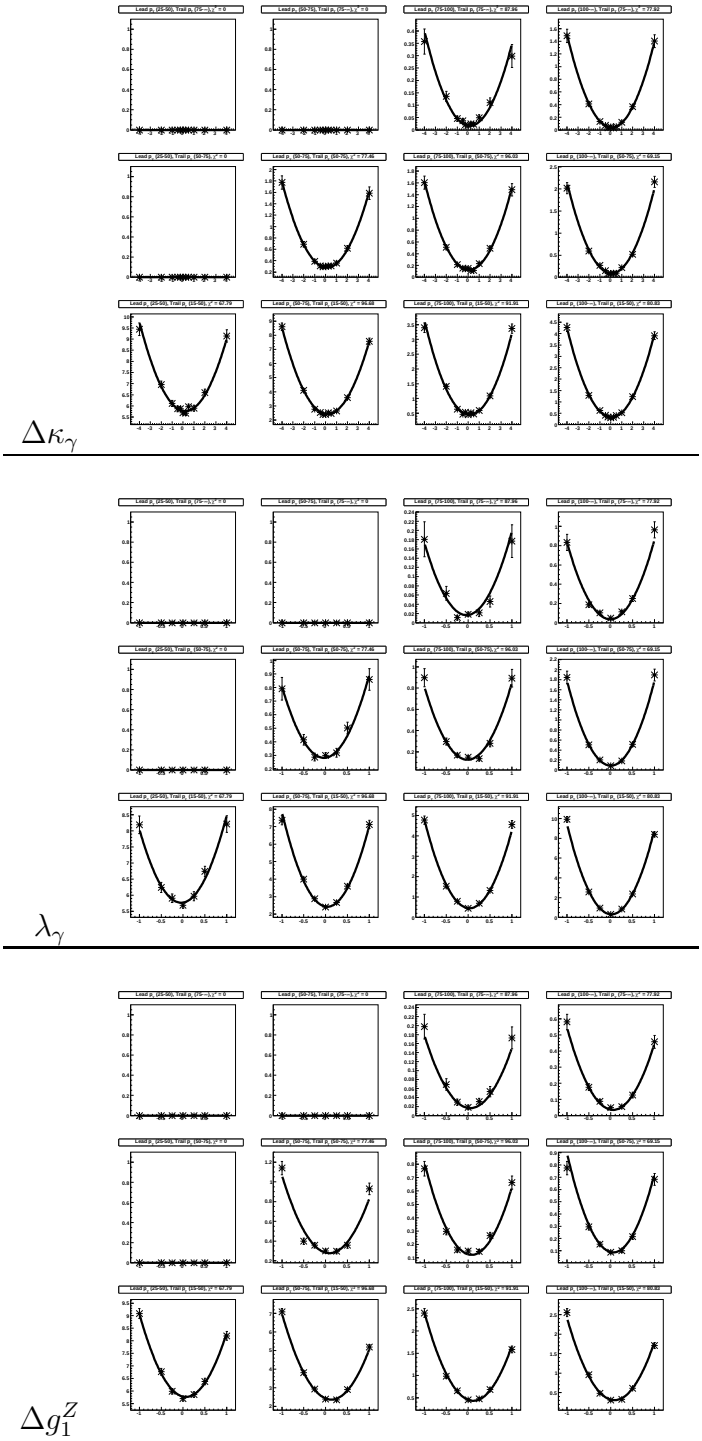

Figure 7.4 : Comparison in the $\mu\mu$ channel of the three-dimensional fit in ($\Delta\kappa_\gamma$, λ_γ, Δg_1^Z) space to the simulated number of WW events along the $\Delta\kappa_\gamma$ axis (top), λ_γ axis (center) and Δg_1^Z (bottom). Each fit in a set is labeled with respect to the two-dimensional p_T bin it represents.

λ_γ limits set in this analysis show significant improvement over all previously tested TGC models in the WW channel at DØ.

Coupling		95% C.L. Limits	Λ (TeV)
$WW\gamma = WWZ$	λ	$-0.31, 0.33$	1.5
	$\Delta\kappa$	$-0.36, 0.47$	
$WW\gamma = WWZ$	λ	$-0.29, 0.30$	2.0
	$\Delta\kappa$	$-0.32, 0.45$	
HISZ	λ	$-0.34, 0.35$	1.5
	$\Delta\kappa_\gamma$	$-0.57, 0.75$	
SM $WW\gamma$	λ_Z	$-0.39, 0.39$	2.0
	$\Delta\kappa_Z$	$-0.45, 0.55$	
SM WWZ	λ_γ	$-0.97, 1.04$	1.0
	$\Delta\kappa_\gamma$	$-1.05, 1.29$	

Table 7.1 : Previously published WW one-dimensional TGC limits, from a ~ 250 pb^{-1} study at DØ [55]. Limits are at the 95% C.L. with various assumptions relating the $WW\gamma$ and WWZ couplings at various values of Λ. Parameters which are not constrained by the coupling relationships are set to their SM values.

The combined limits from the ALEPH, L3 and OPAL experiments at the CERN e^+e^- Collider (LEP), expressed as 95% C.L. limits in the same variables used in this analysis, are $-0.117 < \Delta\kappa_\gamma < 0.061$, $-0.070 < \lambda_\gamma < 0.012$, and $-0.054 < \Delta g_1^Z < 0.028$ [56]. While these limit intervals are significantly smaller than the one-dimensional limit intervals set in this analysis, the measured values from LEP are not directly comparable to those from the Tevatron. While LEP explores a fixed $\sqrt{\hat{s}}$, the Tevatron explores a wide range of $\sqrt{\hat{s}}$ values, as shown in Figure 1.2, and must measure the couplings as form factors, as expressed in Equation 1.9. Additionally, the quoted values from LEP are a combination from multiple experiments, while this analysis probes only a single channel at a single Tevatron experiment. A combination

between WW, $W\gamma$ and WZ processes at DØ may provide much more stringent TGC limits.

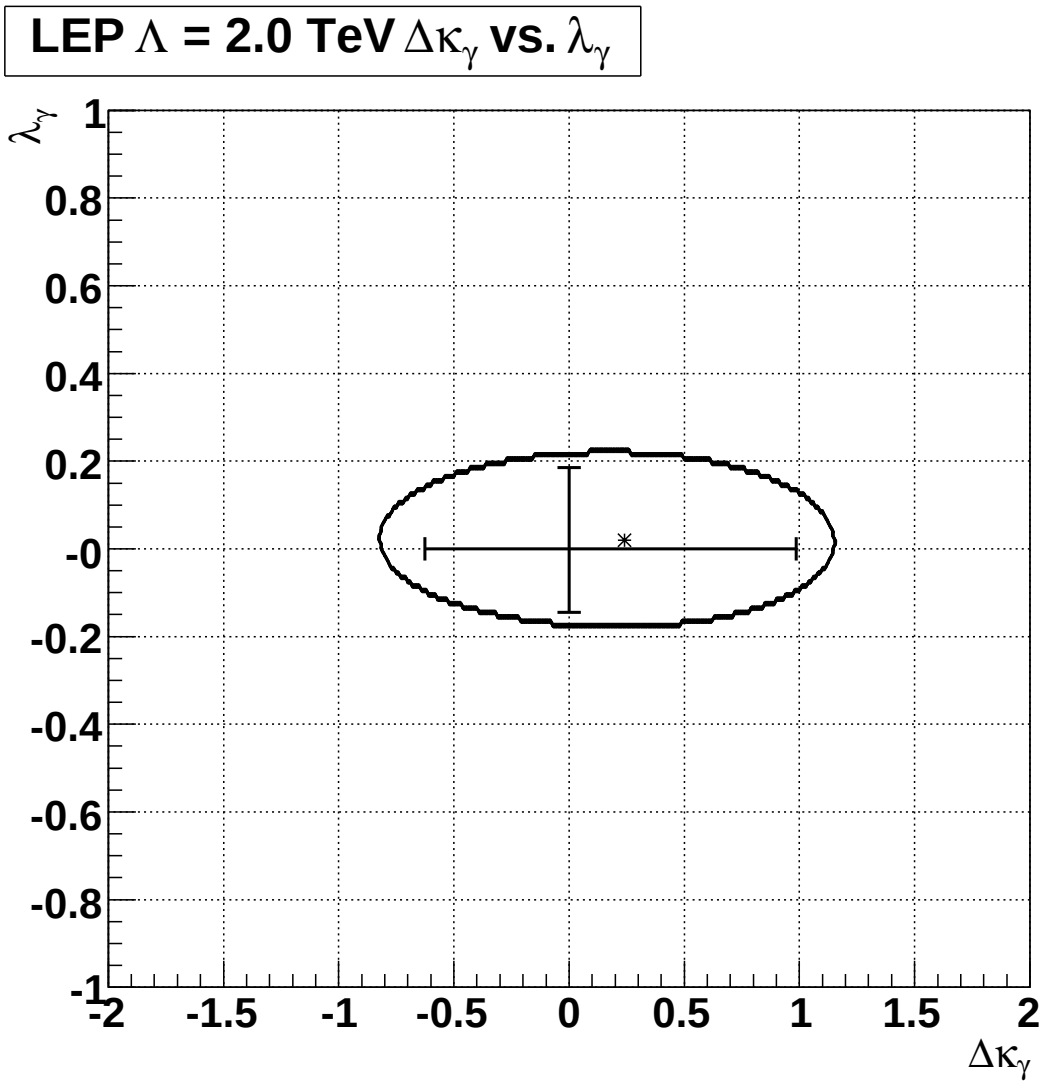

Figure 7.5 : The solid curve represents the two-dimensional 95% C.L. contour in the ($\Delta\kappa_\gamma$, λ_γ) plane, while the tick marks represent the one-dimensional 95% C.L. limits for each coupling. An asterisk ($*$) marks the point with the highest likelihood in the two-dimensional plane.

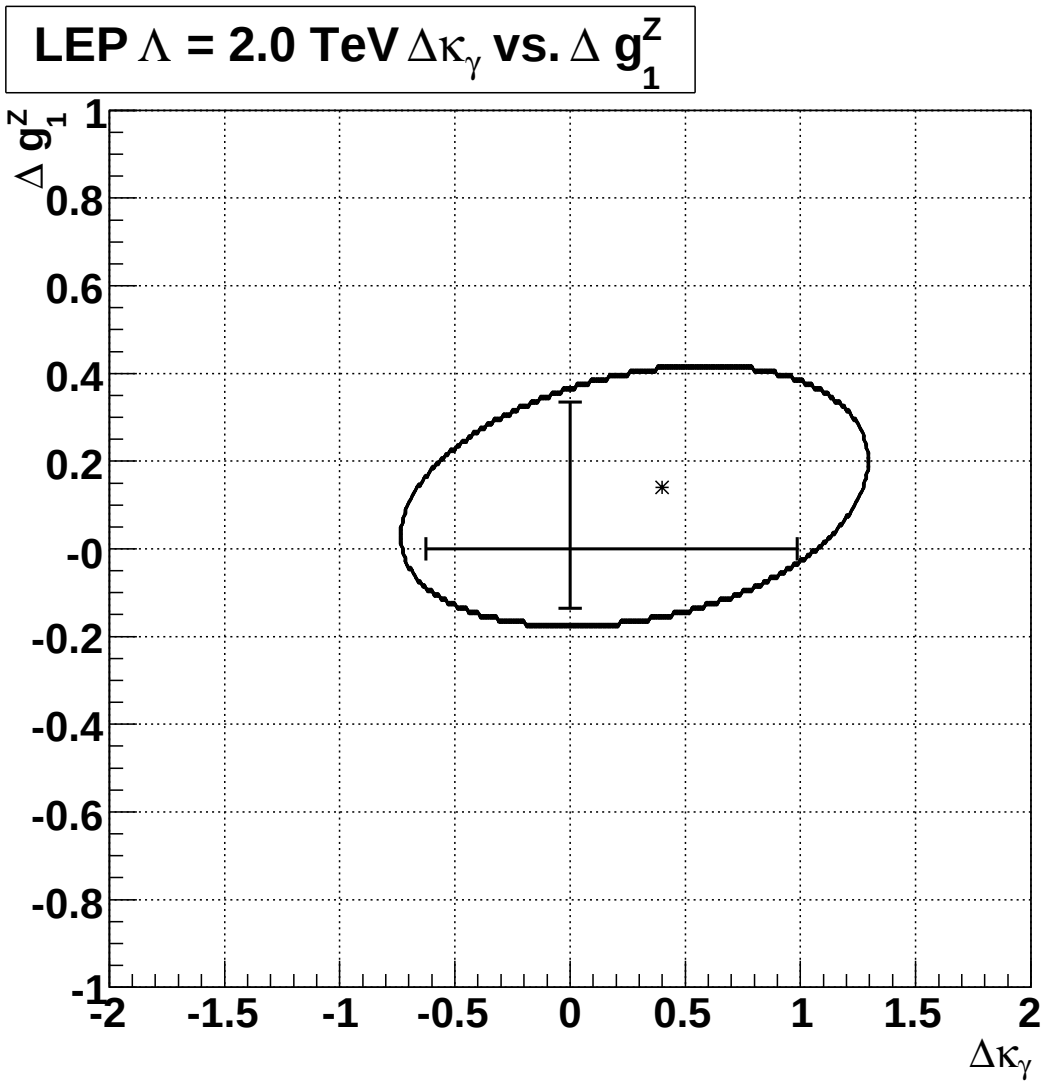

Figure 7.6 : The solid curve represents the two-dimensional 95% C.L. contour in the ($\Delta\kappa_\gamma$, Δg_1^Z) plane, while the tick marks represent the one-dimensional 95% C.L. limits for each coupling. An asterisk ($*$) marks the point with the highest likelihood in the two-dimensional plane.

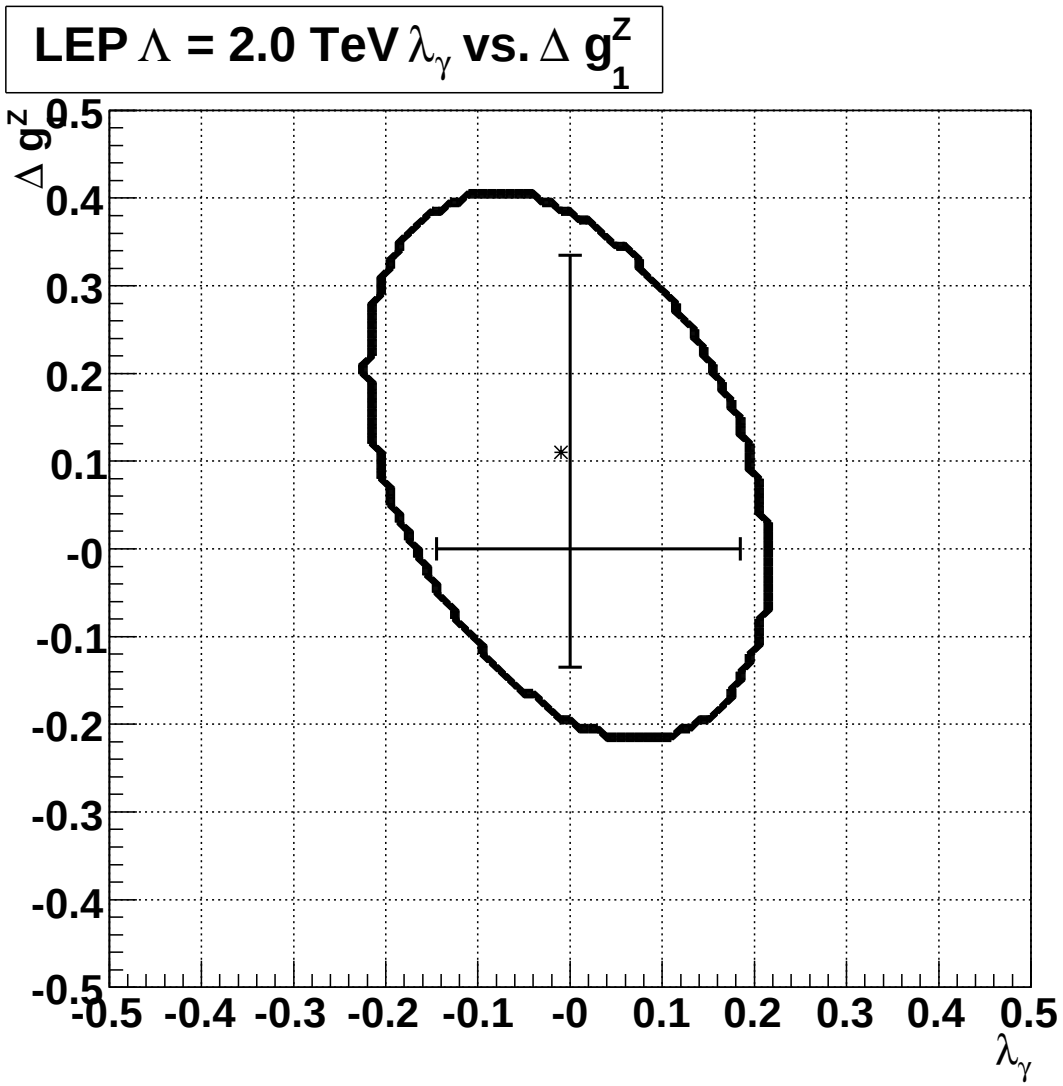

Figure 7.7 : The solid curve represents the two-dimensional 95% C.L. contour in the (λ_γ, Δg_1^Z) plane, while the tick marks represent the one-dimensional 95% C.L. limits for each coupling. An asterisk ($*$) marks the point with the highest likelihood in the two-dimensional plane.

Chapter 8

Conclusion

The WW cross section corresponding to the combined observations across all three final states, ee, $e\mu$ and $\mu\mu$, considering all sources of systematic uncertainty, is

$$\sigma(p\bar{p} \rightarrow WW) = 11.6 \pm 1.8 \text{ (stat)} \pm 0.7 \text{ (syst)} \pm 0.7 \text{ (lumi) pb.}$$

In comparison, the Standard Model theoretical cross section is 12.0 ± 0.6 (scale) $\pm$ 0.3 (PDF) pb [44]. The latest public result from the CDF collaboration is $\sigma(p\bar{p} \rightarrow WW) = 13.6 \pm 2.3(\text{stat}) \pm 1.6(\text{syst}) \pm 1.2(\text{lum})$ pb, using 825 pb^{-1} [52]. The most recent published result from the Fermilab Tevatron Collider is $\sigma(p\bar{p} \rightarrow WW) = 11.8^{+3.7}_{-3.3}(\text{stat})\,^{+1.0}_{-0.8}(\text{syst}) \pm 0.6(\text{lum})$ pb, using 224-252 pb^{-1} [53].

This is the most precise measurement of $\sigma(p\bar{p} \rightarrow WW)$ to date, and is highly statistics limited. Assuming this analysis is repeated on a larger data set using the same methods as presented in this thesis, an increase in integrated luminosity by a factor of ~ 7 is required before the statistical uncertainty is comparable to the systematic uncertainty of the measurement, at which point both are comparable to the luminosity uncertainty. This implies that continual improvement of this measurement may be possible until RunII of the Tevatron concludes.

The one-dimensional 95% C.L. limits on triple gauge-boson couplings (TGCs),

when ignoring C and P violating terms, enforcing electromagnetic gauge invariance, using the $SU(2)_L \otimes U(1)_Y$ constraints from Equations 7.2 and 7.3 and assuming a dipole form factor with $\Lambda = 2$ TeV, are:

$$-0.63 < \Delta\kappa_\gamma < 0.99$$

$$-0.15 < \lambda_\gamma < 0.19$$

$$-0.14 < \Delta g_1^Z < 0.34$$

The combined limits from the ALEPH, L3 and OPAL experiments at the CERN e^+e^- Collider (LEP), expressed as 95% C.L. limits in the same variables used in this analysis, are $-0.117 < \Delta\kappa_\gamma < 0.061$, $-0.070 < \lambda_\gamma < 0.012$, and $-0.054 < \Delta g_1^Z < 0.028$ [56]. While these limit intervals are significantly smaller than the one-dimensional limit intervals set in this analysis, the measured values from LEP are not directly comparable to those from the Tevatron. While LEP explores a fixed $\sqrt{\hat{s}}$, the Tevatron explores a wide range of $\sqrt{\hat{s}}$ values, as shown in Figure 1.2, and must measure the couplings as form factors, as expressed in Equation 1.9. Additionally, the quoted values from LEP are a combination from multiple experiments, while this analysis probes only a single channel at a single Tevatron experiment. A combination between WW, $W\gamma$ and WZ processes at DØ may provide much more stringent TGC limits.

While the 95% C.L. limits on TGCs are only expected to improve as the fourth-root of integrated luminosity, a significant increase in the candidate event sample size

will allow for a more detailed study of the kinematic distributions of those candidates. Anomalous values of the couplings will cause a change in the η and $\Delta\phi$ distributions of charged leptons from those expected in the Standard Model, and TGC sensitivity may be increased by considering such distributions or by studying the lepton p_T distributions on a finer scale than used in this analysis. Additionally, the angular distributions may be able to discriminate between contributions from the CP-conserving λ and the CP-violating $\tilde{\lambda}$ terms in the TGC Lagrangian.

Appendix A

Pythia Underlying Event Tune

The underlying event is modeled based on "Tune A" of PYTHIA as developed by R. Field [57, 58]. The default parameter configuration for this PYTHIA tune is reproduced below.

```
!  Fix Lambda_QCD by hand.  Tuned for the CTEQ6L1 PDFs.  (T.
Nunnemann)
MSTP(2)=1 !  LO evolution of alpha_s for ME
MSTP(3)=1 !  set lambda values by hand; !  The following is good for
CTEQ6L1 !
MSTU(112)=5 !  5 flavour scheme
PARU(112)=0.165 !  lambda_QCD used in PYALPS
PARP(1)=0.165 !  lambda_QCD for ME (hard interaction)
PARP(61)=0.165 !  lamba_QCD for space-like PS
PARP(72)=0.165 !  lambda_QCD for time-like PS (not from resonances)
!
!  HF quarks mass
PMAS(6,1)=170.
PMAS(5,1)=4.75
PMAS(4,1)=1.55
!
!  Set a few B meson/baryon masses to match new ptable.dat and
pdt.table values
PMAS(C5122,1)=5.624
PMAS(C541,1)=6.3
!
!  y* (true rapidity in the HS center-of-mass framework)
CKIN(9)=-5.0 !  Bounds for Max(y*3,y*4)
CKIN(10)=5.0 !  of the 2->2 hard process
CKIN(11)=-5.0 !  Bounds for Min(y*3,y*4)
CKIN(12)=5.0 !  of the 2->2 hard process
```

```
!
!  Underlying event tuning
!  The following PARP(67,83-86,90) parameters should
!  be adapted for PDFs different than CTEQ5L !!!
!  tuneA
MSTP(81)=1 !  TURN ON MULTIPLE INTERACTIONS
MSTP(82)=4 !  varying IP 2-gauss.  matter distr
PARP(67)=4.0 !  ISR Max Scale Factor
PARP(82)=2.0 !  smooth turn off below pT=PARP(82)
PARP(83)=0.5 !
PARP(84)=0.4 !
PARP(85)=0.9 !
PARP(86)=0.95 !
PARP(89)=1800.  !
PARP(90)=0.25 !
!
!  Tau decay
MDCY(15,1)=0 !  Sets tau stable - important for TAUOLA
!
!  The next line is _mandatory_ for RunII production
MSTJ(22)=2 !  A particle is decayed only if its
!  proper lifetime is smaller than PARJ(71)
!  default should be ok (strange particles stable, charm & bottom
decay)
!
MSTU(16)=2 !  Improved particle history record
!  Updated version (Alberto Sanchez, Lars Sonnenschein, 11may04)
!  New default for the Common Samples MC Pythia cardfiles
!  set "most known" B-hadrons stable, decayed by QQ or EvtGen
!
MDCY(C511,1)=0 !  B0
MDCY(C513,1)=0 !  B*0
MDCY(C521,1)=0 !  B+
MDCY(C523,1)=0 !  B*+
MDCY(C531,1)=0 !  B_s0
MDCY(C533,1)=0 !  B_s*0
MDCY(C541,1)=0 !  B_c+
MDCY(C553,1)=0 !  Upsilon
MDCY(C555,1)=0 !  chi_b2
MDCY(C5122,1)=0 !  Lambda_b0
MDCY(C5132,1)=0 !  Xi_b-
MDCY(C20553,1)=0 !  chi_b1
```

```
MDCY(C100553,1)=0 !  Upsilon(2S)
! Updated version (Alberto Sanchez, Lars Sonnenschein, 11may04)
!  New default for the Common Samples MC Pythia cardfiles
!  set "most known" C-hadrons stable, decayed by QQ or EvtGen
!
MDCY(C411,1)=0 !  D+
MDCY(C413,1)=0 !  D*+
MDCY(C415,1)=0 !  D*_2+
MDCY(C421,1)=0 !  D0
MDCY(C423,1)=0 !  D*0
MDCY(C425,1)=0 !  D_2*0
MDCY(C431,1)=0 !  D_s+
MDCY(C433,1)=0 !  D_s*+
MDCY(C435,1)=0 !  D_s2*+
MDCY(C441,1)=0 !  eta_c
MDCY(C443,1)=0 !  J/psi
MDCY(C445,1)=0 !  chi_c2
MDCY(C4112,1)=0 !  Sigma_c0
MDCY(C4114,1)=0 !  Sigma_c*0
MDCY(C4122,1)=0 !  Lambda_c+
MDCY(C4212,1)=0 !  Sigma_c+
MDCY(C4214,1)=0 !  Sigma_c*+
MDCY(C4222,1)=0 !  Sigma_c++
MDCY(C4224,1)=0 !  Sigma_c*++
MDCY(C4312,1)=0 !  Xi'_c0
MDCY(C4314,1)=0 !  Xi_c*0
MDCY(C4322,1)=0 !  Xi'_c+
MDCY(C4324,1)=0 !  Xi_c*+
MDCY(C4334,1)=0 !  Omega_c*0
MDCY(C10411,1)=0 !  D_0*+
MDCY(C10413,1)=0 !  D_1+
MDCY(C10421,1)=0 !  D_0*0
MDCY(C10423,1)=0 !  D_10
MDCY(C10431,1)=0 !  D_s0*+
MDCY(C10433,1)=0 !  D_s1+
MDCY(C10441,1)=0 !  chi_c0
MDCY(C20413,1)=0 !  D'_1+
MDCY(C20423,1)=0 !  D'_10
MDCY(C20433,1)=0 !  D'_s1+
MDCY(C20443,1)=0 !  chi_c1
MDCY(C100443,1)=0 !  psi(2s)
```

Appendix B

W+jets Background Cross-check

A cross-check of the backgrounds involving a charged lepton that is faked by a jet is calculated based on the matrix method as described in [59]. A loose and tight cut is defined for each lepton in Table B.1. For real leptons, the probability to pass a tight cut given that it passes the loose cut, ε, is calculated from standard DØ efficiency files as discussed in Appendix C.2. The probability that a jet faking a lepton passes a tight cut given that it satisfies the loose cut, f, is measured in low $\not\!\!E_T$ QCD dijet events, as described below. The contribution of fake lepton backgrounds is estimated by measuring the number of events that pass the final selection cuts using one loose and one tight lepton, N_{TL}, and comparing that to the number of events with two tight leptons, N_{TT}:

$$N_{TL} = N_{\ell\ell} + N_{\ell j} \tag{B.1}$$

$$N_{TT} = \varepsilon N_{\ell\ell} + f N_{\ell j} \tag{B.2}$$

where $N_{\ell\ell}$ is the number of events with two real leptons and $N_{\ell j}$ is the number of events with one real and one fake lepton. In this analysis, $N_{\ell j}$ represents an estimation of the sum of the W+jet, $W\gamma$ and QCD backgrounds. The quantity of interest is the

number of events from jets faking a tight lepton after the tight selection, $N_{\ell j}^{tight}$:

$$N_{\ell j}^{tight} = f * \frac{\varepsilon N_{TL} - N_{TT}}{\varepsilon - f} \tag{B.3}$$

Lepton	Loose Cut	Tight Cut
Electron	Likelihood > 0.2	Likelihood > 0.85
Muon	Calorimeter Halo < 4.0 and Track Halo < 4.0	Calorimeter Halo < 2.5 and Track Halo < 2.5

Table B.1 : For each lepton, all selection cuts other than those listed above are identical to the cuts described in Section 4.4. The calorimeter halo is the scalar sum of the E_T of all calorimeter cells in a hollow cone $0.1 < \Delta R < 0.4$ around the muon. The track halo is the scalar sum of track p_T, excluding the muon track, in a $\Delta R < 0.5$ cone around the muon.

The efficiency for an electron to pass a tight cut given that it passes a loose cut is determined from the `emid_eff` package efficiency files that measure efficiency with respect to η_{CAL}. The root mean variance of the efficiency calculated for each bin in η_{CAL} is the uncertainty on the rate. The CC and EC electron efficiencies are combined by weighting based on the proportions of CC and EC loose electrons found when calculating the jet fake electron rate, as described below. The efficiency for a muon to pass a tight cut given that it passes a loose cut is calculated in a similar way, based on the `muid_eff` package efficiency files as a function of the number of jets with $p_T > 15$ GeV in an event.

The fake rate, f, is measured using a tag and probe method in $\not\!\!E_T <$ 10 GeV dijet events. The tagged object is the highest p_T jet in the event that satisfies the standard jet identification criteria with $|\eta_{CAL}| < 3.0$. Tag jet candidates flagged as EM objects are removed. A loose or better electron or muon, as defined above, is

counted if it satisfies $\Delta\phi(\text{Tag jet}, \ell) > (\pi - 0.4)$. Events with more than one loose electron or muon are not counted, in order to suppress Z+jet events. The jet fake rate for electrons and muons is calculated as $f = N_T/N_L$, where N_L is the number of loose leptons counted and N_T is the subset of that number that also passed the tight cut. The invariant mass and $\Delta\phi$ between the tag jet and probe lepton are shown in Figure B.1 and Figure B.2, respectively. There does not appear to be a large amount of Z contamination in this data sample, as evidenced by the shape of the invariant mass distributions. The systematic uncertainty for the jet fake rate is the change in the fake rate when a $\not\!\!E_T <$ 20 GeV cut is used instead $\not\!\!E_T <$ 10 GeV. The fake rate as a function of the $\not\!\!E_T$ cut used for electrons and muons is shown in Figure B.3. This systematic uncertainty is added in quadrature with the statistical uncertainty of the fake rate measurement to represent the total uncertainty of the fake rate. The measured rates and the calculated efficiencies are listed in Table B.2.

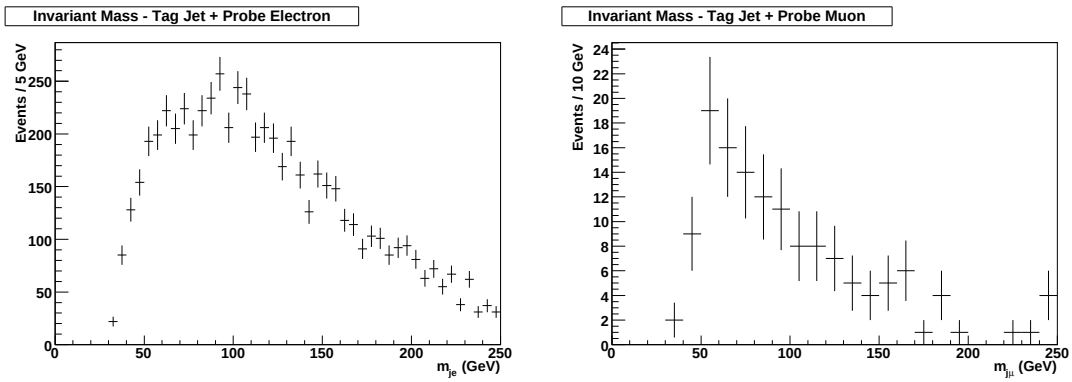

Figure B.1 : The invariant mass between the tag jet and the probe electron (left) or muon (right) for all events with leptons passing loose selection cuts.

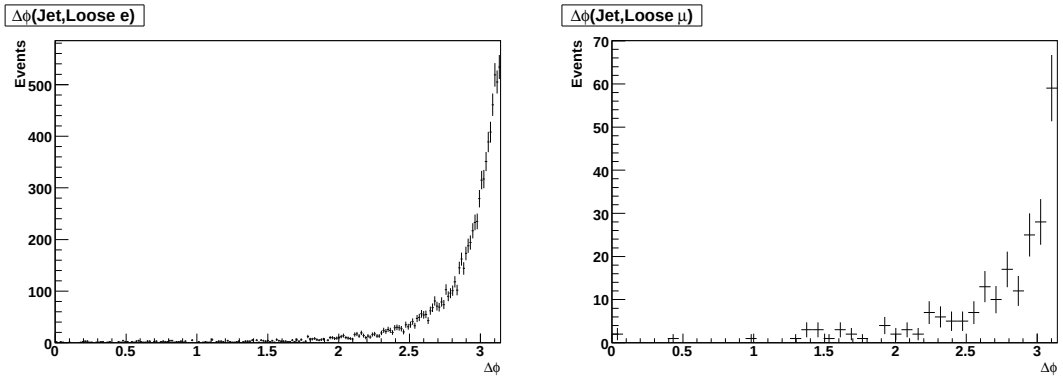

Figure B.2 : The azimuthal separation between the tag jet and the probe electron (left) or muon (right) for all events with leptons passing loose selection cuts.

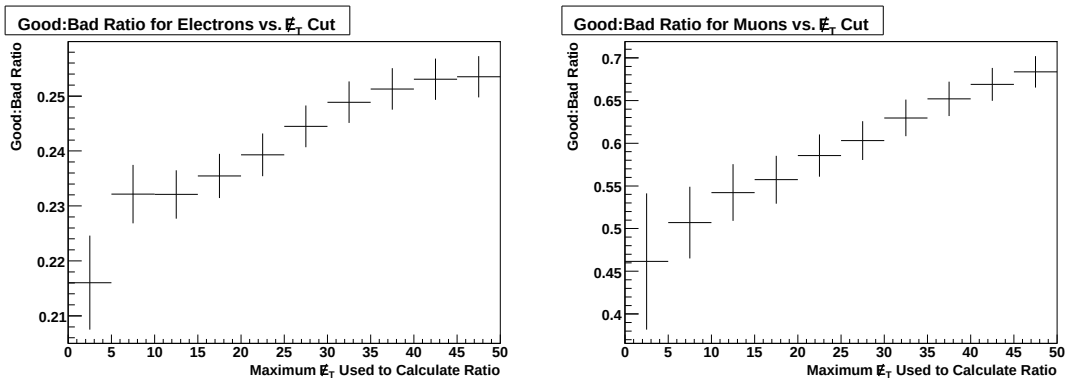

Figure B.3 : The jet fake rate as a function of the maximum $\not\!\!E_T$ allowed in events that enter the calculation for jets faking electrons (left) and muons (right). At high values of $\not\!\!E_T$, the fake rate is expected to rise due to W+jet contamination.

Lepton	ε	f
Electron	86.87 ± 3.50 %	23.22 ± 0.62 %
Muon	96.67 ± 4.93 %	50.70 ± 7.32 %

Table B.2 : The efficiency of a real lepton to pass a tight cut given that it passes the loose cut (ε) and the fake rate for a jet to pass the tight cut if it passes the loose cut (f).

The results of the matrix method estimation for ℓj events is summarized in Table B.3. The matrix method often estimates a $N_{\ell j}$ value consistent with zero in the case where a jet fakes a muon.

Background Events from Jets faking Electrons		
Channel & Selection Stage	Matrix Method	Monte Carlo
ee After Cut 1	14.6 ± 2.8	7.93 ± 2.29
ee After Cut 2	7.26 ± 1.71	4.65 ± 1.35
ee Final Selection	6.99 ± 1.68	4.52 ± 1.34
$e\mu$ After Cut 1	12.97 ± 3.91	11.56 ± 2.97
$e\mu$ After Cut 2	8.11 ± 2.52	9.11 ± 2.38
$e\mu$ Final Selection	4.68 ± 1.80	7.86 ± 2.20
Background Events from Jets faking Muons		
Channel & Selection Stage	Matrix Method	Monte Carlo
$e\mu$ After Cut 1	6.55 ± 11.82	2.48 ± 1.10
$e\mu$ After Cut 2	< 11.39	2.48 ± 1.10
$e\mu$ Final Selection	< 5.96	1.80 ± 0.99
$\mu\mu$ After Cut 1	< 11.72	4.98 ± 2.28
$\mu\mu$ After Cut 2	< 4.63	4.38 ± 2.20
$\mu\mu$ Final Selection	< 2.37	4.38 ± 2.20

Table B.3 : Comparison of the expected number of events from ℓj backgrounds from the matrix method and from the Monte Carlo used in this analysis. Numbers consistent with zero are quoted as 95% C.L. limits. In the ee channel, Cut 1 is $\not\!\!E_T >$ 40 GeV, Cut 2 is $q_T < 20$ GeV, and the final cut is ($\not\!\!E_T >$ 50 GeV if $|M_Z - M_{ee}| < 7$ GeV). In the $e\mu$ channel, Cut 1 is $\not\!\!E_T >$ 20 GeV, Cut 2 is $q_T < 24$ GeV, and the final cut is ($\not\!\!E_T >$ 50 GeV if $\Delta\phi_{e\mu} > 2.85$). In the $\mu\mu$ channel, Cut 1 is ($\not\!\!E_T >$ 35 GeV and $\cos(\Delta\phi_{\not\!\!E_T,\mu}) < 0.98$), Cut 2 is $q_T < 19$ GeV, and the final cut is $\Delta\phi_{\mu\mu} < 2.55$.

Appendix C

DØ-Specific Analysis Details

The DØ Collaboration has built a common framework for physics analysis that involves many shared tools. Collaborators are encouraged to use common tools and data sets as a basis for their analyses so that methods and results within the collaboration are internally consistent. This appendix details the specific information about common data files and tools that are used in the course of this analysis.

This analysis uses the "RunIIa" data sample of the DØ Collider Detector, including events starting from run number 151817 on April 19, 2002, and ending with run number 215670 on February 22, 2006. This data sample corresponds to approximately 1 fb^{-1} of integrated luminosity. (See Sec. C.1 for the detailed calculation of integrated luminosity.)

Common Analysis Format (CAF) data samples are taken from the Common Samples Group (CSG) skims, using the "2EMhighpt", "EMMU" and "2MUhighpt" skims for the ee, $e\mu$ and $\mu\mu$ channels, respectively. All RunIIa data, including the "PASS3_p17.09.03", "PASS3_p17.09.06" and "PASS3_p17.09.06b" datasets for each skim, is included in this analysis.

C.1 Triggering and Integrated Luminosity Calculation

The ee and $e\mu$ channels use the same set of Single EM triggers to select events. The list of triggers used in each version of the trigger list is shown in Tab. C.1. This analysis uses the "Single Muon OR" as defined in [51] to select events in the $\mu\mu$ channel, where a muon must fire a trigger from the list shown in Tab. C.2. In all channels, a lepton is considered to fire a trigger if it is spatially matched to all L1, L2 and L3 components of a specific trigger and that trigger fired during the event.

Trigger Version	Single Electron Triggers Used
v8-v11	EM_HI EM_HI_SH EM_HI_2EM5_SH
v12	E1_SH30 E1_SHT20 E2_SHT20 E3_SHT20
v13	E1_SH30 E1_SHT22 E2_SHT22 E3_SHT22
v14	E1_SH35 E3_SH35 E1_SHT25 E3_SHT25 E1_T13SHT15
	E1_T15SH20 E3_T13SHT15 E3_T15SH20

Table C.1 : Single electron triggers used in each version of the trigger list.

Triggers Used in Single Muon Trigger OR		
MU_W_L2M0_TRK3	MU_W_L2M0_TRK10	MU_W_L2M3_TRK10
MU_W_L2M5_TRK10	MUW_W_L2M3_TRK10	MUW_W_L2M5_TRK10
MUW_A_L2M3_TRK10	MUH1_TK10	MUH1_TK12_TLM12
MUH1_ILM15	MUH1_TK12	MUH1_LM15
MUH4_LM15	MUH4_TK10	MUH5_LM15
MUH6_TK12_TLM12	MUH6_LM15	MUH6_TK10
MUH7_TK12	MUH7_LM15	MUH7_TK10
MUH8_TK12_TLM12	MUH8_ILM15	

Table C.2 : Single muon triggers used across all versions of the trigger list.

For the ee and $e\mu$ channels, integrated luminosity is calculated by using the

`lm_tools` package associated with the `t07.05.00` release of DØ framework code. An initial list of bad run numbers and bad luminosity block numbers is taken from the `dq_defs` package, using the `v2007-10-01-fixed` tag. The ee channel removes bad runs and bad luminosity block numbers from all subdetectors except for the muon system, while the $e\mu$ channel removes items marked bad from every subdetector including the muon system.

Parentage files are generated based on the Common Samples Group "2EMhighpt" and "EMMU" skims, for the ee and $e\mu$ channels, respectively. Both of these channels use the same set of Single EM triggers, as listed in Tab. C.1. A "good runs list" is used that consists of all runs in which at least one of the appropriate Single EM triggers in use is unprescaled.

Luminosity is determined by using the bad runs list, bad luminosity block numbers list and good runs list as described, basing the luminosity for each epoch on a trigger that is not prescaled and always present in the good runs list for that epoch. Trigger epochs are used as defined in [60]. For trigger epochs v8-10 and v11, good runs lists were manipulated such that the two triggers spanning those epochs did not overlap when calculating integrated luminosity. The integrated luminosity results for each trigger epoch are summarized in Tab. C.3.

The `lm_tools` package also produces a list of additional bad luminosity block numbers that are concatenated with those from `dq_defs` before processing data in this analysis.

Trigger Epoch	Base Trigger (ee,$e\mu$)	ee	$e\mu$	$\mu\mu$
v8-10	EM_MX, EM_HI	72.36	60.85	24.19
v11	EM_MX, EM_HI	65.95	65.83	70.93
v12a-b	E1_SH30	136.04	132.4	220.03
v12c	E1_SH30	103.9	99.12	—
v13a	E1_SH30	57.05	55.08	31.68
v13b-e	E1_SH30	327.02	324.06	324.33
v14a	E1_SH35	166.89	162.46	140.5
v14b	E1_SH35	75.45	74.86	190.59
v14c	E1_SH35	58.96	57.58	—
v14d	E1_SH35	39.98	39.55	—
Total		1103.60	1071.78	1002.24

Table C.3 : Integrated luminosity, in pb^{-1}, by trigger epoch. The $\mu\mu$ channel numbers are reproduced from [51]. A "—" indicates that this trigger epoch's integrated luminosity is included in the number immediately above. The $\mu\mu$ luminosity is based on the JT_125TT trigger in every epoch.

The luminosity for the $\mu\mu$ channel is that associated with the standard DØ "Single Muon OR" set of triggers, as described in [51].

Each analysis channel removes individual events that are flagged for a known calorimeter problem. An additional efficiency is applied to each channel of the analysis based on the amount of integrated luminosity in each trigger epoch, as described in [61]. This leads to an efficiency loss of about 3% in each analysis channel, as shown in Tab. C.4.

Channel	CAL Flag Efficiency
ee	96.990 ± 0.010 %
$e\mu$	96.985 ± 0.010 %
$\mu\mu$	96.944 ± 0.010 %

Table C.4 : Efficiency of applying calorimeter event flag vetoes in each channel.

C.2 CAF Environment Code

A common set of tools is available for analyzing CAF files, called the CAF Environment (CAFE). This analysis uses various CAFE packages to apply corrections to MC events as they are processed, in order to correct primary vertex z positions, instantaneous luminosity distributions, and the efficiency of object selection cuts. Additional smearing is also applied to MC muons and jets after the full detector simulation, in order to fine tune the matching between data and MC distributions. The CAFE package versions used in this analysis are summarized in Table C.5.

Package Name	Version
caf_dq	v02-02-02
cafe	p18-br-132
caf_eff_utils	p18-br-07
cafe_sam	p18-br-07
caf_mc_util	p18-br-40
caf_pdfreweight	v00-00-03
caf_trigger	p18-br-15
caf_util	p18-br-47
dq_defs	v2007-10-01-fixed
dq_util	v02-03-00
eff_utils	p18-br-13
emid_cuts	p18-br-03
emid_eff	Tv7-preliminary-06
jetcorr	p18-br-09
jetid_eff	Tv01-01-03
lumi_profiles	Tv2008-03-04
met_util	p18-br-01
muid_eff	v04-01-02
tau_tmb	p18-br-09
tmb_tree	p18-br-91
trigeff_cafe	v00-03-00

Table C.5 : The specific version of each DØ code package as used in this analysis.

The `emid_eff` and `muid_eff` packages are used to adjust the efficiency of electron and muon object selection, respectively. The `caf_mc_util` package contains standardized code to reweight the Z p_T spectrum of $Z/\gamma*$ MC samples, as well as code to adjust MC instantaneous luminosity profiles and primary vertex z distributions to better match those in data.

The effect of reweighting the instantaneous luminosity profile and the primary vertex z distribution for MC samples is illustrated in Fig. C.1. These reweighting schemes do not necessarily preserve the total weight of all events in a MC sample, so special adjustments are made for each MC sample in order to maintain proper integrated luminosity scaling.

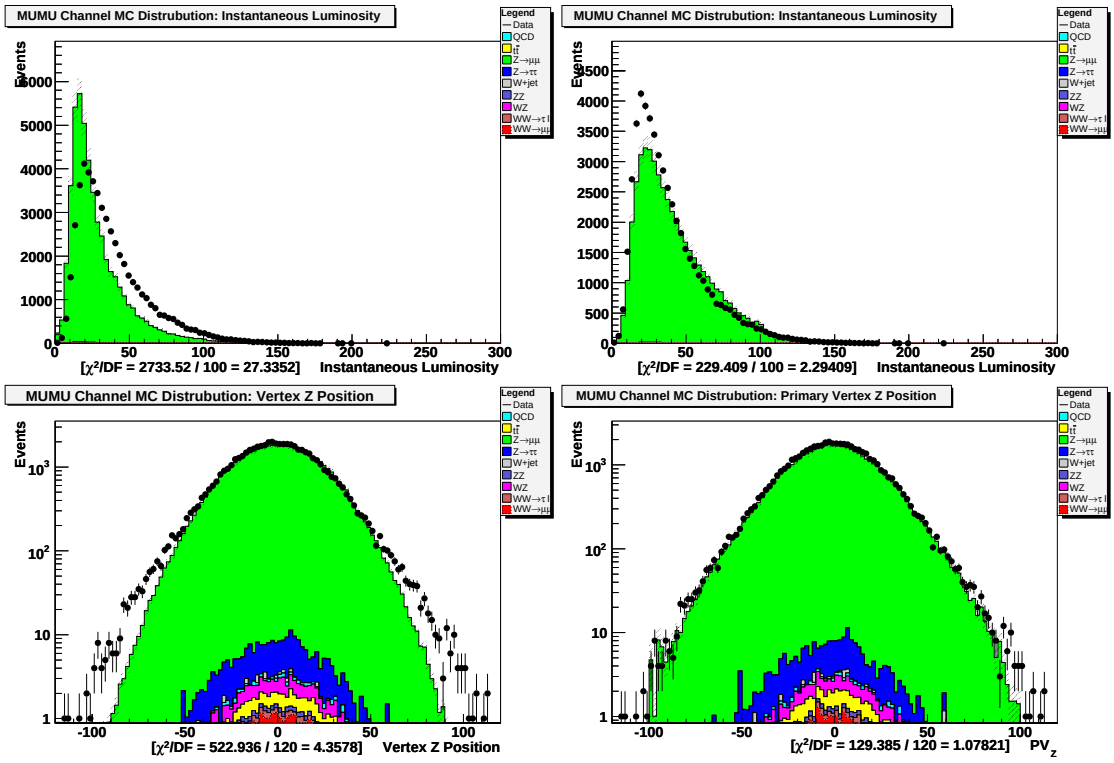

Figure C.1 : The top-left and top-right plots show the instantaneous luminosity profile comparison between data and MC before and after reweighting, respectively. The lower-left and lower-right plots similarly show the primary vertex z position before and after reweighting.

Appendix D

Individual Kinematic Distribution Plots

The invariant mass and q_T distributions for individual signal and background samples in each channel after preselection are provided in this Appendix.

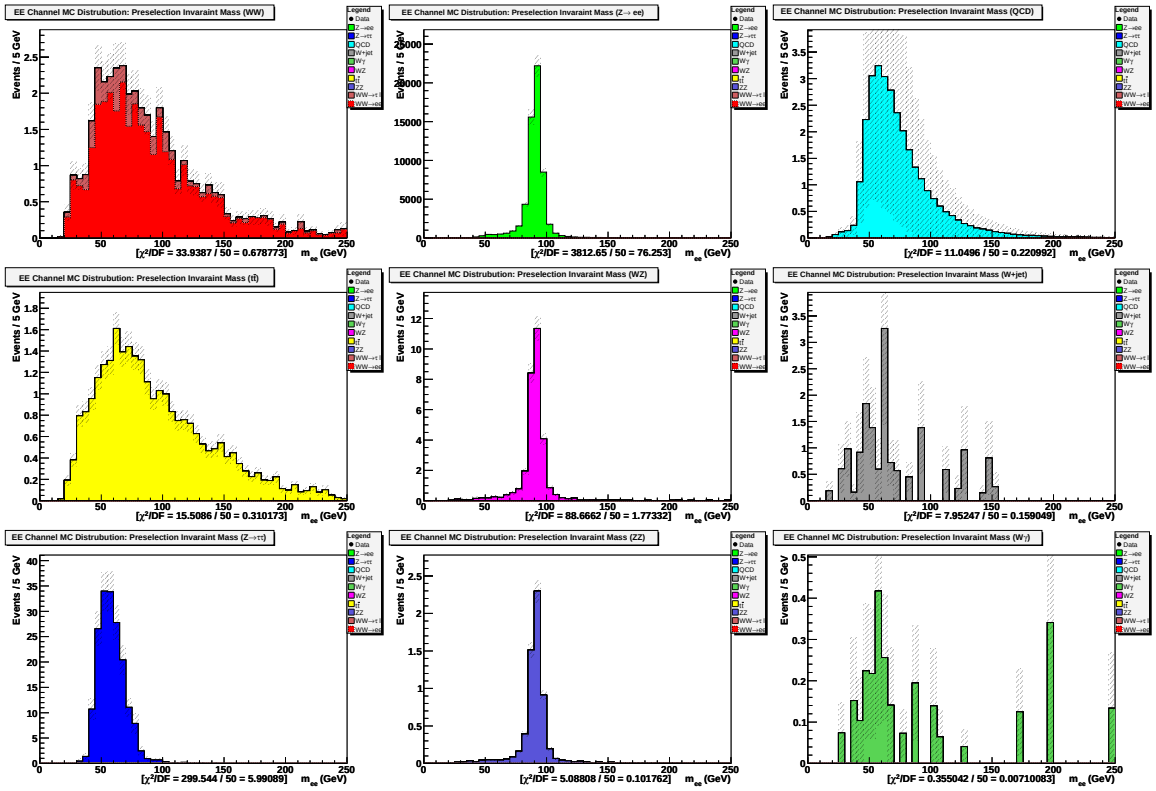

Figure D.1 : The invariant mass for the signal estimate and individual background estimates in the ee channel after preselection. Top row, left to right: WW, $Z \to ee$, QCD. Center row, left to right: $t\bar{t}$, WZ, W+jet. Bottom row, left to right: $Z \to \tau\tau$, ZZ, $W\gamma$.

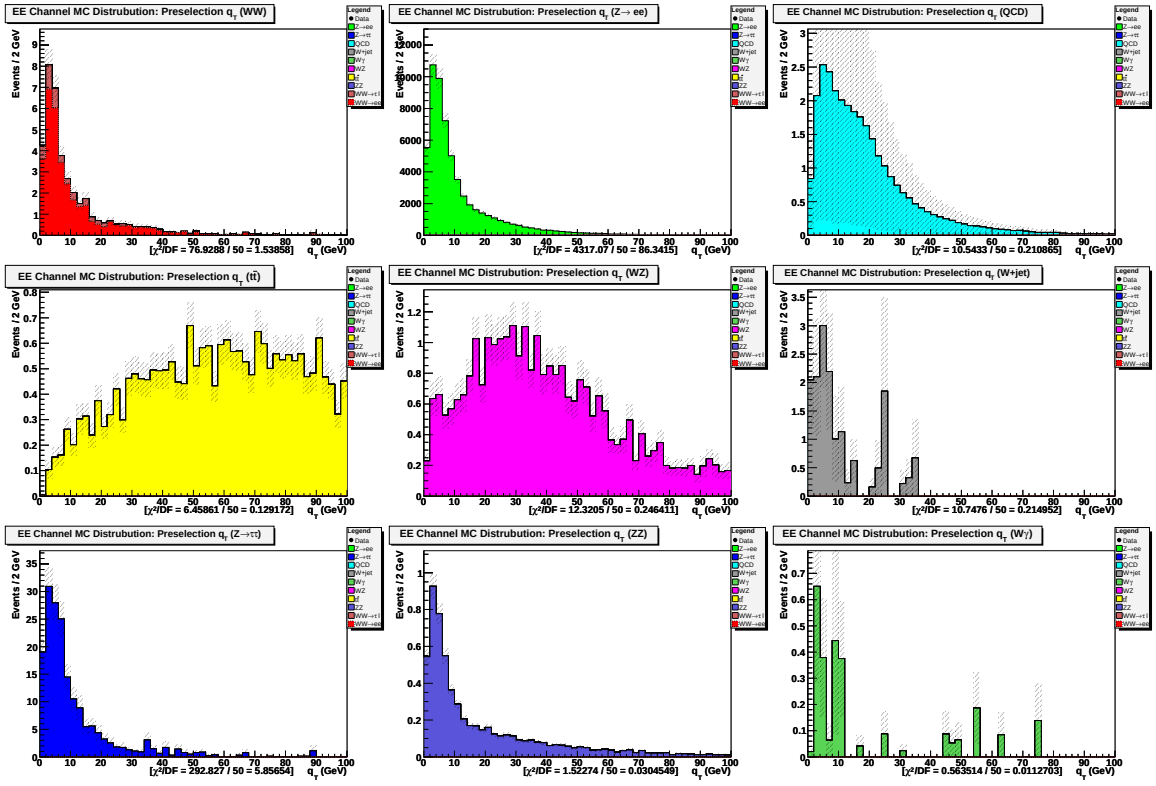

Figure D.2 : The q_T for the signal estimate and individual background estimates in the ee channel after preselection. Top row, left to right: WW, $Z \to ee$, QCD. Center row, left to right: $t\bar{t}$, WZ, W+jet. Bottom row, left to right: $Z \to \tau\tau$, ZZ, $W\gamma$.

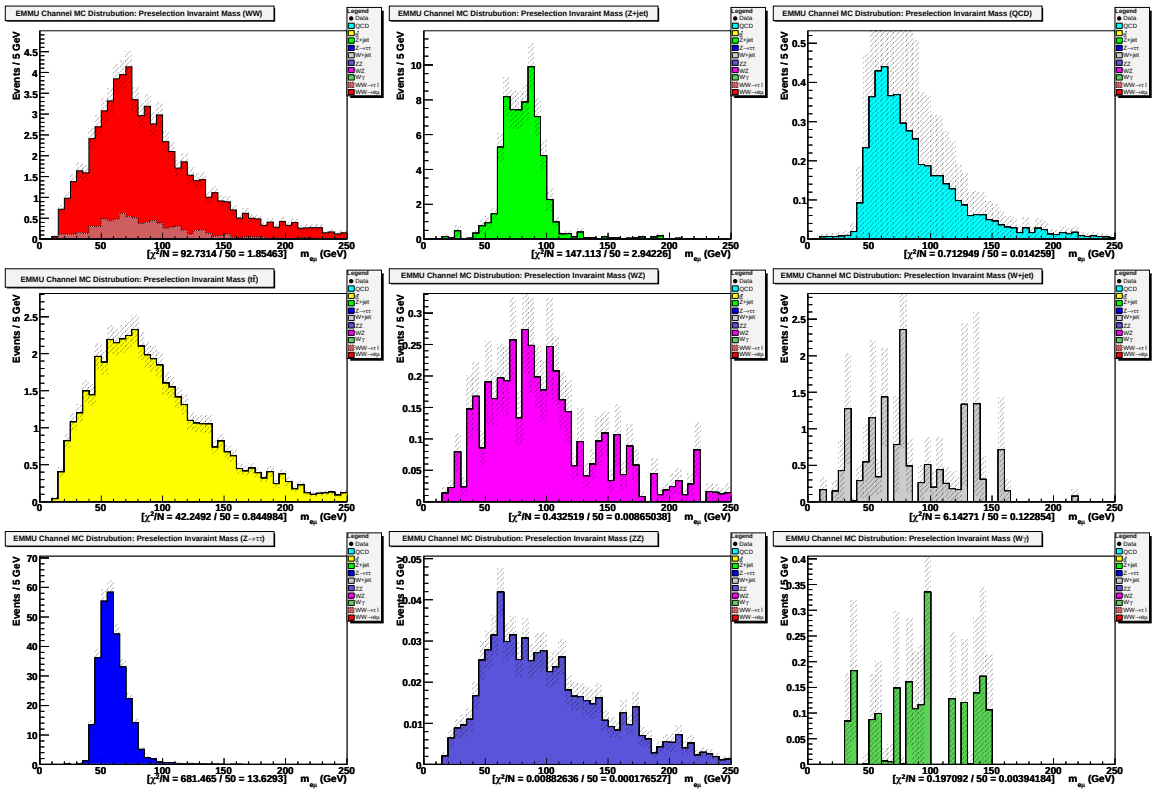

Figure D.3 : The invariant mass for the signal estimate and individual background estimates in the $e\mu$ channel after preselection. Top row, left to right: WW, Z+jet, QCD. Center row, left to right: $t\bar{t}$, WZ, W+jet. Bottom row, left to right: $Z \to \tau\tau$, ZZ, $W\gamma$.

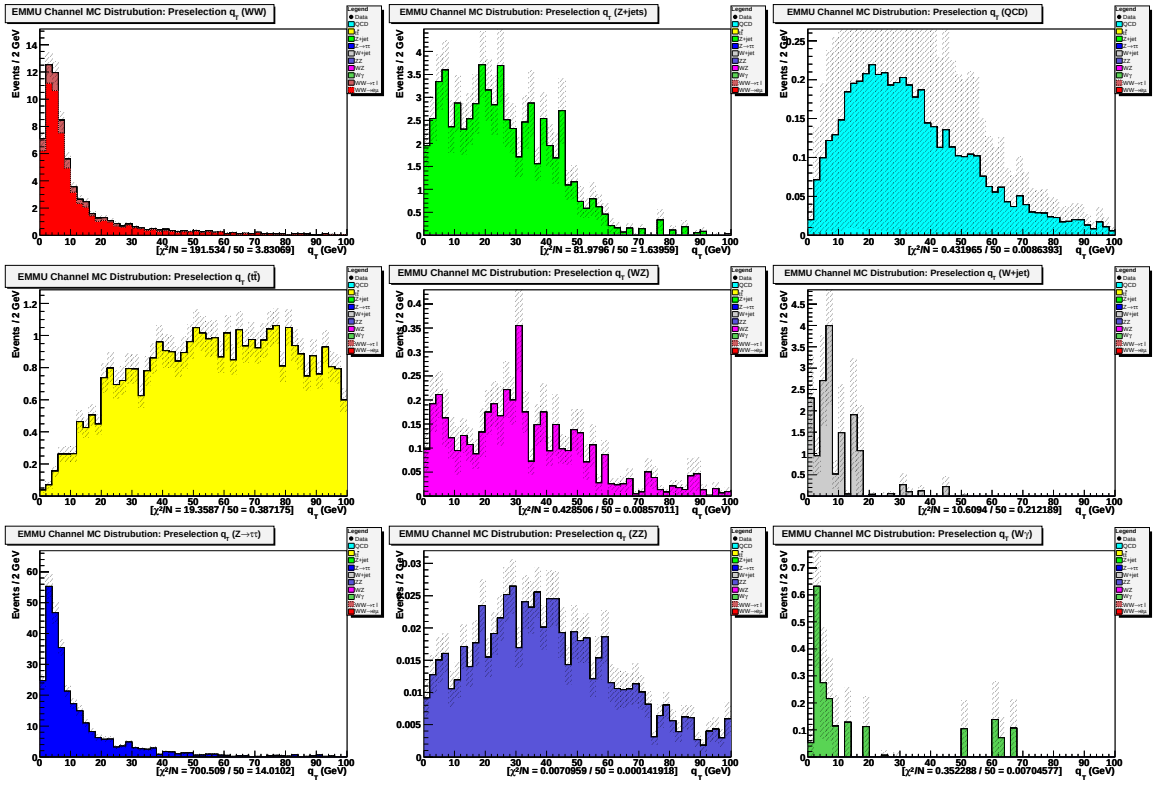

Figure D.4 : The q_T for the signal estimate and individual background estimates in the $e\mu$ channel after preselection. Top row, left to right: WW, Z+jet, QCD. Center row, left to right: $t\bar{t}$, WZ, W+jet. Bottom row, left to right: $Z \to \tau\tau$, ZZ, $W\gamma$.

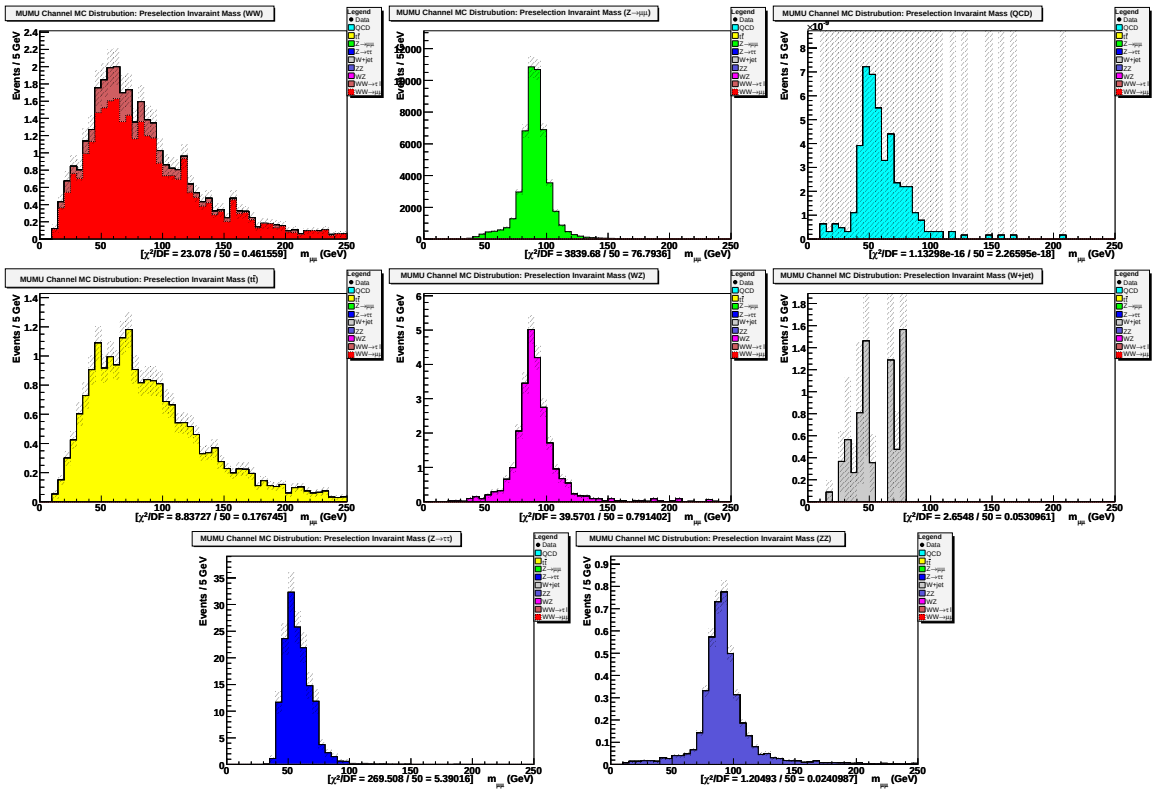

Figure D.5 : The invariant mass for the signal estimate and individual background estimates in the $\mu\mu$ channel after preselection. Top row, left to right: WW, $Z \to \mu\mu$, QCD. Center row, left to right: $t\bar{t}$, WZ, W+jet. Bottom row, left to right: $Z \to \tau\tau$, ZZ.

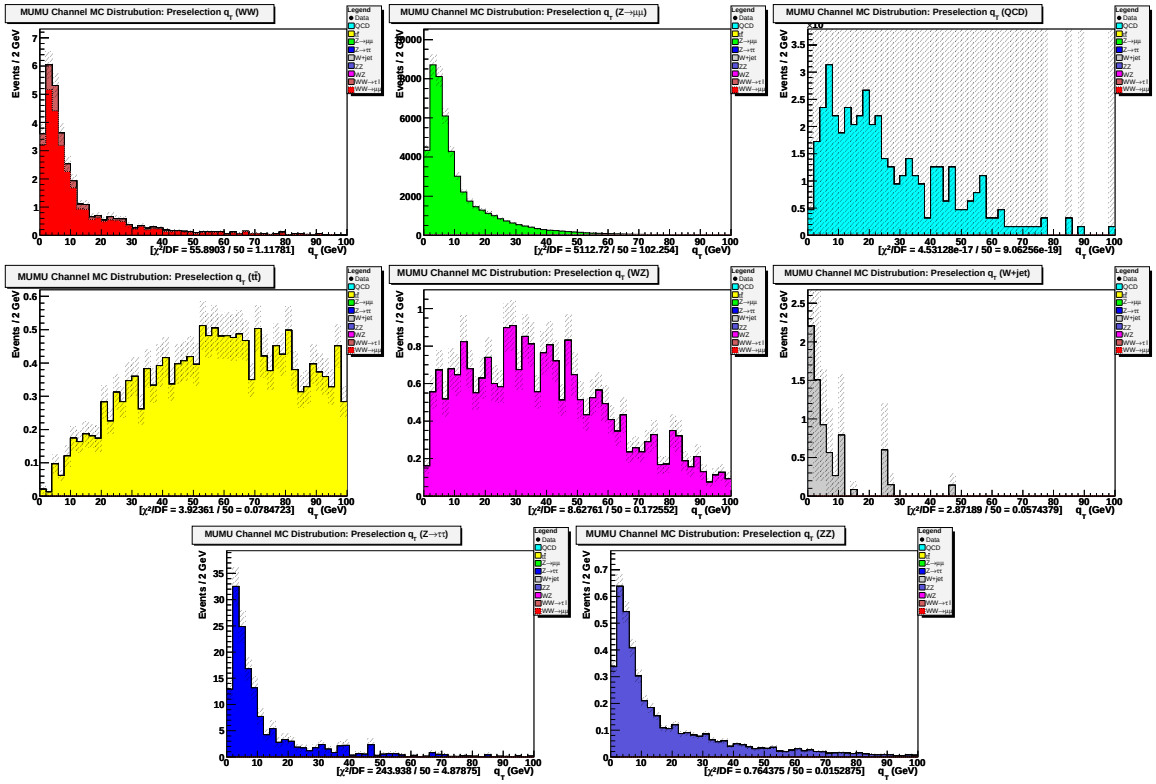

Figure D.6 : The q_T for the signal estimate and individual background estimates in the $\mu\mu$ channel after preselection. Top row, left to right: WW, $Z \to \mu\mu$, QCD. Center row, left to right: $t\bar{t}$, WZ, W+jet. Bottom row, left to right: $Z \to \tau\tau$, ZZ.

Bibliography

[1] F. Halzen and A. D. Martin. *Quarks & Leptons: An Introductory Course in Modern Particle Physics*. John Wiley & Sons, New York, 1984.

[2] N. Cabibbo. Unitary Symmetry and Leptonic Decays. *Phys. Rev. Lett.*, 10:531, 1963.

[3] M. Kobayashi and T. Maskawa. CP Violation in the Renormalizable Theory of Weak Interaction. *Prog. Theor. Phys.*, 49:652, 1973.

[4] A.D. Sakharov. Violation of CP Symmetry, C-Asymmetry and Baryon Asymmetry of the Universe. *Pisma Zh. Eksp. Teor. Fiz.*, 5:32, 1967. Translation in JETP Lett. 5: 24-27 (1967).

[5] S. Laporta and E. Remiddi. The analytical value of the electron $(g-2)$ at order α^3 in QED. *Phys. Lett.*, B379, 1996.

[6] B. Odom, D. Hanneke, B. D'Urson, and G. Gabrielse. New Measurement of the Electron Magnetic Moment. *Phys. Rev. Lett.*, 97:030801, 2006.

[7] K. Hagiwara, J. Woodside, and D. Zeppenfeld. Measuring the WWZ coupling at the Tevatron. *Phys. Rev.*, D41:2113–2119, 1990.

[8] G. Azuelos et al. Electroweak Physics. *CERN-TH/2000-102*, 2000. hep-ph/0003275v1.

[9] U. Baur and D. Zeppenfeld. Unitarity Constraints on the Electroweak Three Vector Boson Verticies. *Phys. Lett.*, B201:383, 1988.

[10] K. Hagiwara, S. Ishihara, R. Szalapski, and D. Zeppenfeld. Low energy effects of new interactions in the electroweak boson sector. *Phys. Rev.*, D48:2182, 1993.

[11] Fermilab Accelerator Division. Operations Rookie Books, 2006-2008. http://www-bdnew.fnal.gov/operations/rookie_books/rbooks.html.

[12] D. Groom et al. Review of particle physics. *The European Physical Journal*, C15, 2000.

[13] S. Abachi et al. The DØ Upgrade: The Detector and Its Physics. *FERMILAB-PUB-96-357-E*, 1996.

[14] The DØ Upgrade Central Fiber Tracker: Technical Design Report. http://d0server1.fnal.gov/users/stefan/www/CFT_TDR/CFT_TDR.ps.

[15] S. Klimenko, J. Konigsberg, and T.M. Liss. Averaging of the inelastic cross sections measured by the CDF and the E811 experiments, 2003. FERMILAB-FN-0741.

[16] B. Casey, M. Corcoran, Y. Enari, M. Prewitt, and G Snow. Determination of the DØ RunIIb Luminosity Constants. Internal Note 5559, DØ Collaboration, 2007.

[17] V.M. Abazov et al. The Upgraded DØ Detector. *Nucl. Instr. and Methods*, A565:463, 2006.

[18] G. Blazey. DØ Run II Trigger Page. http://niuhep.physics.niu.edu/∼blazey/upgrade.html.

[19] M. Cooke. Operation and Efficiency of the DØ Central Track Trigger. Master's thesis, Rice University, 2004.

[20] A. Khanov. HTF: histogramming method for finding tracks. The algorithm description. Internal Note 3778, DØ Collaboration, 2000.

[21] G. Borissov. Ordering a Chaos or... Technical Details of AA Tracking. http://www-d0.fnal.gov/global_tracking/talks/20030228/talk-adm-030228.ps.

[22] K. Bloom and A. Dominguez. DØ Tracking Performance at High Luminosity. Internal Note 4980, DØ Collaboration, 2006.

[23] F. Fleuret. The DØ Electron/Photon Analysis Package EMAnalyze. Internal Note 3888, DØ Collaboration, 2001.

[24] J. Zhu. Determination of Electron Energy Scale and Energy Resolution using P14 $Z \to ee$ data. Internal Note 4323, DØ Collaboration, 2004.

[25] G. Steinbrück. *Measurement of the Angular Distribution of Electrons from W Boson Decays at DØ*. PhD thesis, University of Oklahoma, 1999.

[26] J. Kozminski, R. Kehoe, H. Weerts, S.J. Park, A. Quadt, J. Gardner, and S. Jabeen. Electron Likelihood in p14. Internal Note 4449, DØ Collaboration, 2004.

[27] L. Wang, J. Hays, J. Mitrevski, and C. Schwanenberger. Electron Likelihood Efficiency in p17. Internal Note 5114, DØ Collaboration, 2006.

[28] E. Busato and B. Andrieu. Jet Algorithms in D0 RunII Software: Description and User's Guide. Internal Note 4457, DØ Collaboration, 2004.

[29] G. Blazey et al. Run II Jet Physics: Proceedings of the Run II QCD and Weak Boson Physics Workshop. *hep-ex/0005012v2*, 2000.

[30] A. Harel. Jet ID optimization. Internal Note 4919, DØ Collaboration, 2005.

[31] M. Voutilainen. Jet p_T resolution for Run IIa final JES (v7.2) with dijet J4S jet corrections. Internal Note 5499, DØ Collaboration, 2007.

[32] O. Peters. Muon Segment Reconstruction - Linked List Algorithm, 2001. http://www-d0.fnal.gov/nikhef/muon_reco/segmentreco/... MuonSegmentReconstruction.pdf.

[33] F. Déliot. The Fit Algorithm in muo_trackreco, 2000. http://www-d0.fnal.gov/∼deliot/fitalg.ps.

[34] L. Chevalier et al. Track Parameter Error Matrix Propagation in Matter and Magnetic Field, Error Matrices Combination, 2001. http://www-clued0.fnal.gov/∼tuchming/myprop.ps.

[35] M. Arthaud, F. Deliot, B. Tuchming, V. Sharyy, and D. Vilanova. Muon Momemtum Oversmearing for p17 Data. Internal Note 5444, DØ Collaboration, 2007.

[36] H.-U. Bengtsson and T. Sjöstrand. The Lund Monte Carlo for hadronic processes – PYTHIA version 4.8. *Comp. Phys. Comm.*, 46:43, 1987.

[37] T. Sjöstrand et al. High-energy-physics event generation with PYTHIA 6.1. *Comput. Phys. Commun.*, 135:238, 2001.

[38] S. Agostinelli et al. Geant4 – A Simulation Toolkit. *Nucl. Instrum. Methods*, A506:250, 2003.

[39] J. Allison et al. Geant4 Developments and Applications. *IEEE Trans. Nucl. Sci.*, 53:270, 2006.

[40] Y. Fisyak and J. Womersley. D0gstar DØ GEANT Simulation of the Total Apparatus Response. Internal Note 3191, DØ Collaboration, 1997.

[41] H. Fox. Search for the Higgs boson in $H \to WW* \to \mu\mu$ decays in 930pb^{-1} at D0 in RunII. Internal Note 5194, DØ Collaboration, 2006.

[42] M. Titov, R. Bernhard, and B. Penning. Search for $H \to WW^* \to ll'$ $(l, l' = e, \mu)$ Production Using Neural Networks with 1.1 fb^{-1} of Run IIa Data. Internal Note 5496, DØ Collaboration, 2007.

[43] H. Fox and M. Titov. Search for the Higgs Boson in $H \to WW^* \to ll'$ ($l, l' = e, \mu$) decays with up to 1.7 fb^{-1} at DØ in Run II. Internal Note 5537, DØ Collaboration, 2007.

[44] J.M. Campbell and R.K. Ellis. Update on vector boson pair production at hadron colliders. *Phys. Rev.*, D60:113006, 1999.

[45] J.D. Hobbs, T. Nunnemann, and R. Van Kooten. Study of $p\bar{p} \to Z\gamma* \to ee$ and $p\bar{p} \to Z\gamma* \to \mu\mu$ event yields as a luminosity cross check. Internal Note 5268, DØ Collaboration, 2006.

[46] M. Cacciari, S. Frixione, G. Ridolfi, M.L. Mangano, and P. Nason. The $t\bar{t}$ cross-section at 1.8 and 1.96 tev: a study of the systematics due to parton densities and scale dependence. *JHEP*, 404:68, 2004.

[47] U. Baur and E.L. Berger. Probing the $WW\gamma$ vertex at the Fermilab Tevatron Collider. *Phys. Rev.*, D41:1476, 1990.

[48] C. Balazs and C.P. Yuan. Soft gluon effects on lepton pairs at hadron colliders. *Phys. Rev.*, D56:5558, 1997.

[49] B. Tiller and T. Nunnemann. Measurement of the differential Z-boson production cross-section as function of transverse momentum. Internal Note 4660, DØ Collaboration, 2004.

[50] J. Hays, J. Mitrevski, and C.Schwanenberger. The Program Package em_cert: Version p18-br-20. Internal Note 5070, DØ Collaboration, 2006.

[51] P. Calfayan. ORing single muon triggers in p17 data. Internal Note 5329, DØ Collaboration, 2007.

[52] M. Neubauer. Diboson Physics at the Tevatron. *hep-ex/0605066v2*, 2006. CDF and DØ Collaborations.

[53] V.M. Abazov et al. Measurement of the WW production cross section in $p\bar{p}$ collisions at $\sqrt{s} = 1.96$ TeV. *Phys. Rev. Lett.*, 94:151801, 2005. Erratum submitted to Phys. Rev. Lett. corrects luminosity to yield $\sigma(p\bar{p} \to WW) = 11.8^{+3.7}_{-3.3}(\text{stat})\,^{+1.0}_{-0.8}(\text{syst}) \pm 0.6(\text{lum})$ pb.

[54] Greg Graham et al. Status of the Fast Simulation, PMCS, December 2002. Internal Note 4059, DØ Collaboration, 2002.

[55] V. Abazov et al. Limits on anomalous trilinear gauge couplings from $WW \to e^+e^-$, $WW \to e\mu$, and $WW \to \mu^+mu^-$ events from $p\bar{p}$ collisions at $\sqrt{\hat{s}} = 1.96$ TeV. *Phys. Rev.*, D74:057101, 2006. [Erratum-ibid. D74 059904 (2006)].

[56] The LEP Collaborations ALEPH, DELPHI, L3, OPAL, and the LEP TGC Working Group. A combination of results on charged triple gauge boson couplings measured by the lep experiments. *LEPEWWG/TGC/2005-01*, 2005. Prepared from published results of the LEP experiments.

[57] R.D. Field. Studying the Underlying Event at CDF. *CDF/PUB/JET/PUBLIC/8548*, 2006.

[58] R. Field. Min-Bias and the Underlying Event in Run 2 at CDF. *APP*, B36/2:137, 2005.

[59] E. Barberis, T. Golling, I. Iashvili, A. Juste, A. Quadt, and P. Schieferdecker. The Matrix Method and its Error Calculation. Internal Note 4564, DØ Collaboration, 2004.

[60] H. Schellman. Data and MC sets for the Second pass Run II Z cross section measurement. Internal Note 5374, DØ Collaboration, 2007.

[61] J. Hays, H. Schellman, and J. Steele. Calorimeter Event Quality Flag Rates for W/Z Production Cross-section Measurement (second pass). Internal Note 5412, DØ Collaboration, 2007.